

NIST Technical Note 1886

An Experimental and Computational Study of Precast Concrete Moment Frames under a Column Removal Scenario

Joseph A. Main
Yihai Bao
H.S. Lew
Fahim Sadek
Vincent P. Chiarito
Stephen D. Robert
Jorge O. Torres



NIST Technical Note 1886

An Experimental and Computational Study of Precast Concrete Moment Frames under a Column Removal Scenario

Joseph A. Main
Yihai Bao
H.S. Lew
Fahim Sadek
*Engineering Laboratory
National Institute of Standards and Technology*

Vincent P. Chiarito
Stephen D. Robert
Jorge O. Torres
*Engineer Research and Development Center
U.S. Army Corps of Engineers
Vicksburg, MS*

<http://dx.doi.org/10.6028/NIST.TN.1886>

September 2015



U.S. Department of Commerce
Penny Pritzker, Secretary

National Institute of Standards and Technology
Willie E. May, Under Secretary of Commerce for Standards and Technology and Director

The policy of the National Institute of Standards and Technology is to use metric units in all its published materials. Because this report is intended for the U.S. building construction industry, which uses inch-pound units, it is more practical and less confusing to use inch-pound units, in some cases, rather than metric units. However, in most cases, units are presented in both metric and the inch-pound system.

Certain commercial entities, equipment, products, or materials are identified in this document in order to describe a procedure or concept adequately. Such identification is not intended to imply recommendation or endorsement by the National Institute of Standards and Technology, nor is it intended to imply that the entities, products, materials, or equipment are necessarily the best available for the purpose.

National Institute of Standards and Technology Technical Note 1886
Natl. Inst. Stand. Technol. Tech. Note 1886, 102 pages (September 2015)
<http://dx.doi.org/10.6028/NIST.TN.1886>
CODEN: NTNOEF

ABSTRACT

This report presents an experimental and computational study of two precast concrete moment-frame assemblies under a column removal scenario. The main objectives of the study were to (1) characterize the behavior and failure modes of the assemblies through full-scale testing and (2) develop computational models that could adequately capture the experimental observations and provide additional insights into the influence of key factors on the responses of the assemblies. The two moment-frame assemblies represented portions of the perimeter moment frames of two 10-story precast concrete frame buildings. One assembly was part of an ordinary moment frame (OMF) from a building designed for Atlanta, Georgia (Seismic Design Category B), and the other assembly was part of a special moment frame (SMF) from a building designed for Seattle, Washington (Seismic Design Category D). The assemblies, each comprising three columns and two beams, were subjected to monotonically increasing vertical displacement of the unsupported center column. The tests were continued beyond the ultimate capacities of the assemblies to characterize the failure modes and collapse mechanisms that were developed. Experimental measurements included the vertical load, vertical and horizontal displacements at specific locations, rotations at beam ends, and strains in reinforcing bars and other steel components. In addition, video cameras recorded the progression of damage, including surface cracking, spalling, and component failure in the regions surrounding each moment connection. The failure of both the OMF and the SMF specimens was characterized by (1) fracture of the bottom anchorage bars at the welded connection to the center column and (2) diagonal cracking and shear deformation of the end columns under outward forces generated by arching action in the beams. Other failure modes that were observed included shear stud failure for the OMF specimen and bond failure of anchorage bars for the SMF specimen.

Computational analyses of the moment-frame assembly tests were carried out using detailed finite element models, in which solid elements were used to represent the concrete, steel plates, and steel angles, while beam elements were used to represent the longitudinal and transverse reinforcing bars in the beams and columns. The models were able to capture the primary response characteristics of the test specimens, and the analyses provided additional insights into the overall behavior and failure modes. The analyses revealed that out-of-plane bending moments, resulting from eccentricities in the forces transferred through the welded beam-to-column connections, contributed to the fracture of the anchorage bars in the moment-frame assemblies. Reductions in ductility resulting from welding also contributed to the fracture of the anchorage bars, as evidenced by component-level testing of a welded anchorage bar, which enabled calibration of the fracture criterion in the finite element modeling. The analyses confirmed that the vertical loads were resisted initially through flexural action and subsequently through arching action, after closure of the initial gaps between the beams and columns. An energy-based analysis of sudden column loss revealed that the ultimate capacities of the moment frames slightly exceeded the applicable gravity loads, by 2 % - 11 %. However, the analyses revealed that the responses of the assemblies were quite sensitive to uncertain factors such as anchorage bar ductility and the initial gap width between the beams and columns, and variations in these factors could result in specimens that would not sustain the applicable gravity loads under sudden column loss.

Keywords: buildings; computational model; design standards; disproportionate collapse; finite element analysis; moment resisting connections; progressive collapse; precast concrete structures; structural robustness; testing.

This page intentionally left blank.

PREFACE

The experimental and computational study reported herein is part of a comprehensive research program being carried out by the National Institute of Standards and Technology (NIST) on prevention of disproportionate collapse of building structures. To meet the critical need for experimental data, NIST developed a plan to test a series of full-scale structural assemblies of common building types.

This report presents the results from an experimental and computational study of two precast concrete moment-frame assemblies. The specimens represent portions of the perimeter moment frames of two precast concrete buildings designed for Seismic Design Categories B and D and incorporating ordinary moment frames and special moment frames, respectively. Detailed design of the buildings was carried out by S. K. Ghosh and Associates. The design was guided by a panel of experts who reviewed the design and provided valuable comments. The following experts served on the panel: David R. Bonneville (Degenkolb Engineers, San Francisco, CA), Donald O. Dusenberry (Simpson, Gumpertz & Heger, Waltham, MA), Ramon Gilsanz (Gilsanz, Murray, Steficek, LLP, New York, NY), Thomas A. Sabol (Englekirk & Sabol, Los Angeles, CA), and Andrew W. Taylor (KPF Consulting Engineers, Seattle, WA).

This research was carried out by NIST in partnership with the U.S. Army Engineer Research and Development Center (ERDC) in Vicksburg, Mississippi. ERDC erected the test specimens, deployed the instruments, performed the tests, and collected the test data. NIST developed the test plan and designed the specimens, developed finite-element models of the test specimens and performed pre-test analyses to guide the development of the test plan, analyzed the experimental data to characterize the responses of the specimens and compared the data with computational results, performed post-test analyses to investigate the sensitivity of the response to various factors, and wrote the report. Zhiyu Zong contributed to the finite element model development and experimental data analysis while a Guest Researcher at NIST. Isaiah Sampson contributed to the analysis and plotting of experimental data during a Summer Undergraduate Research Fellowship at NIST. Financial support for the full-scale tests was provided by NIST and the Precast/Prestressed Concrete Institute (PCI). The test specimens were fabricated and contributed by the Metromont Corporation.

The authors gratefully acknowledge the thorough review of this report by Jonathan M. Weigand of NIST and David J. Stevens of Protection Engineering Consultants.

This page intentionally left blank.

TABLE OF CONTENTS

Abstract.....	iii
Preface	v
Table of Contents.....	vii
List of Figures.....	ix
List of Tables	xiii
List of Acronyms and Abbreviations.....	xiv
Chapter 1 Introduction.....	1
1.1 Background.....	1
1.2 Scope of Study.....	2
1.3 Report Outline.....	2
Chapter 2 Prototype Buildings.....	3
2.1 Design of Prototype Buildings.....	3
2.2 Design of Moment Frames.....	4
Chapter 3 Experimental Program.....	7
3.1 Test Specimens	7
3.2 Experimental Configuration.....	10
3.3 Instrumentation	12
3.3.1 OMF Specimen.....	13
3.3.2 SMF Specimen	15
Chapter 4 Experimental Results	19
4.1 OMF Specimen	19
4.1.1 Observed Behavior and Failure Modes	19
4.1.2 Displacement and Rotation Measurements	24
4.1.3 Strain Measurements	27
4.2 SMF Specimen.....	35
4.2.1 Observed Behavior and Failure Modes	35
4.2.2 Displacement and Rotation Measurements	40
4.2.3 Strain Measurements	43
4.3 Summary and Discussion.....	49

Chapter 5 Computational Modeling and Analysis	53
5.1 Pre-Test Modeling and Model Sensitivities.....	53
5.2 Finite Element Models.....	56
5.3 Material Modeling	58
5.3.1 Concrete.....	58
5.3.2 Steel Plates and Angles	59
5.3.3 Reinforcing Bars.....	60
5.3.4 Torsion Bars	61
5.3.5 Shear Studs.....	61
5.4 Welded Anchorage Bar Modeling	62
5.4.1 Interaction of Bending Moment and Axial Force.....	63
5.4.2 Reduction of Ductility in Heat-Affected Zone	67
5.5 Analysis of Test Specimens	70
5.5.1 OMF Specimen.....	70
5.5.2 SMF Specimen	74
5.6 Influence of Span Length.....	78
5.7 Summary and Discussion.....	79
Chapter 6 Evaluation of Structural Robustness	81
6.1 Gravity Loads	81
6.2 Energy-Based Analysis.....	81
6.3 Results.....	82
6.4 Discussion and Limitations.....	84
Chapter 7 Summary and Conclusions.....	85
References	87

LIST OF FIGURES

Figure 2–1. (a) Plan layout and (b) elevation view of prototype buildings.....	3
Figure 2–2. Perspective illustration of a perimeter moment frame showing link-plate connections and placement of spandrel beams within pockets in the columns.	5
Figure 2–3. Ordinary moment frame (OMF) connection details.	5
Figure 2–4. Special moment frame (SMF) connection details.....	6
Figure 3–1. Details of OMF specimen.....	8
Figure 3–2. Details of SMF specimen.....	9
Figure 3–3. Precast concrete beams and columns prior to assembly.	9
Figure 3–4. Front and top views of experimental configuration.	11
Figure 3–5. Oblique view of experimental configuration including reaction frame.	11
Figure 3–6. Assembled specimens prior to testing: (a) OMF specimen; (b) SMF specimen.	12
Figure 3–7. Instrumentation: (a) load cell; (b) string potentiometer; (c) LVDT; (d) inclinometer.	13
Figure 3–8. Displacement and rotation transducers (OMF specimen).....	14
Figure 3–9. Strain gauges on anchorage bars (OMF specimen).	14
Figure 3–10. Strain gauges on flexural reinforcing bars (OMF specimen).....	14
Figure 3–11. Strain gauges on link plates and brace beam (OMF specimen).....	15
Figure 3–12. Displacement and rotation transducers (SMF specimen).	16
Figure 3–13. Strain gauges on flexural reinforcing bars (SMF specimen).	16
Figure 3–14. Strain gauges on shear studs (SMF specimen).	16
Figure 3–15. Strain gauges on link plates and brace beams (SMF specimen).	17
Figure 4–1. Applied vertical load vs. vertical displacement of center column for OMF specimen (labeled points correspond to images in Figure 4–2).	20
Figure 4–2. Progression of damage for OMF specimen (images correspond to labeled points in Figure 4–1).	21
Figure 4–3. Detachment of upper column plate from left end column (OMF specimen).....	23
Figure 4–4. Fractured anchorage bars from lower left connection to center column (OMF specimen). ...	23
Figure 4–5. Final damage to right end column viewed from several angles (OMF specimen).	23
Figure 4–6. Final damage to left end column viewed from several angles (OMF specimen).	23
Figure 4–7. Detachment of upper column plate from right end column (OMF specimen).....	24
Figure 4–8. Out-of-plane bending of link plates at right end column: (a) upper link plate; (b) lower link plate (OMF specimen).	24
Figure 4–9. Applied vertical load vs. vertical displacements at (a) center column and (b) midspan of beams (OMF specimen).	25

Figure 4–10. Vertical displacement profile of beams corresponding to indicated vertical loads (OMF specimen; displacements magnified).	25
Figure 4–11. Beam end rotations (OMF specimen).	26
Figure 4–12. Horizontal displacement of end columns at beam mid-height (OMF specimen).	27
Figure 4–13. Strain in upper anchorage bars at end columns (OMF specimen).	27
Figure 4–14. Strain in lower anchorage bars at center column (OMF specimen).	28
Figure 4–15. Deformation and strain profile in anchorage bar and link plate of OMF specimen: (a) tension in anchorage bar; (b) compression in anchorage bar.	28
Figure 4–16. Axial force in anchorage bars (OMF specimen).	30
Figure 4–17. Bending moment in anchorage bars (OMF specimen).	30
Figure 4–18. Interaction diagrams for axial force and bending moment in anchorage bars (OMF specimen).	30
Figure 4–19. Axial strain in link plates at end columns (OMF specimen).	31
Figure 4–20. Axial strain in link plates at center column (OMF specimen).	31
Figure 4–21. Strain in flexural reinforcing bars at midspan of beams (OMF specimen).	33
Figure 4–22. Average strain in flexural reinforcing bars at midspan of beams (OMF specimen).	33
Figure 4–23. Axial strain at midspan of front brace beam (OMF specimen).	34
Figure 4–24. Axial force in front brace beam (OMF specimen).	34
Figure 4–25. Applied vertical load vs. vertical displacement of center column for SMF specimen (labeled points correspond to images in Figure 4–26).	35
Figure 4–26. Progression of damage for SMF specimen (images correspond to labeled points in Figure 4–25).	37
Figure 4–27. Fractured anchorage bars from lower left connection to center column (SMF specimen)...	39
Figure 4–28. Progression of splitting failure and concrete spalling at upper anchorage bars at right end column (SMF specimen).	39
Figure 4–29. Final damage to right end column viewed from several angles (SMF specimen).	39
Figure 4–30. Final damage to left end column viewed from several angles (SMF specimen).	40
Figure 4–31. Applied vertical load vs. vertical displacements at (a) center column, (b) 3/4 span of beams, (c) midspan of beams, and (b) 1/4 span of beams (SMF specimen).	41
Figure 4–32. Vertical displacement profile of beams corresponding to indicated vertical loads (SMF specimen; displacements magnified).	41
Figure 4–33. Beam end rotations (SMF specimen).	42
Figure 4–34. Horizontal displacement of end columns (SMF specimen).	42
Figure 4–35. Axial strain in link plates at end columns (SMF specimen).	44
Figure 4–36. Axial strain in link plates at center column (SMF specimen).	44
Figure 4–37. Deformation and strain profiles in anchorage bar and link plate of SMF specimen: (a) tension in anchorage bar; (b) compression in anchorage bar.	45

Figure 4–38. Strain in shear studs on upper column plate on left end column (SMF specimen).....	45
Figure 4–39. Strain in flexural reinforcing bars at midspan of beams (SMF specimen).	47
Figure 4–40. Average strain in flexural reinforcing bars at midspan of beams (SMF specimen).	47
Figure 4–41. Strain in brace beams at midspan (SMF specimen).....	48
Figure 4–42. Axial force in brace beams (SMF specimen).....	48
Figure 4–43. Three stages in the response of the precast concrete specimens.....	50
Figure 4–44. Top view of link plate connection showing (a) eccentricity in force transfer and (b) resulting out-of-plane bending.	50
Figure 5–1. Influence of key factors on computed response of OMF specimen.....	55
Figure 5–2. Influence of key factors on computed response of SMF specimen.	55
Figure 5–3. Finite element models: (a) OMF specimen; (b) SMF specimen.....	57
Figure 5–4. Solid-element mesh in connection region (SMF specimen).	57
Figure 5–5. Modeling details at moment connection (top view).	58
Figure 5–6. Stress-strain response of concrete material model: (a) compression; (b) tension.....	59
Figure 5–7. Stress-strain curves used to model steel components.	60
Figure 5–8. Normalized shear force vs. slip relationship used for shear studs.	61
Figure 5–9. Finite element models of a welded anchorage bar under eccentric loading: (a) detailed model; (b) reduced model.	63
Figure 5–10. Calibrated detailed model analysis of reinforcing bar tensile test.	65
Figure 5–11. Detailed model analysis of welded anchorage bar under eccentric loading.	65
Figure 5–12. Bending moment in welded anchorage bar vs. distance along bar.	66
Figure 5–13. Interaction of axial force and bending moment for welded anchorage bars under eccentric loading: (a) #10 bar, (b) #11 bar.	67
Figure 5–14. Component test setup for welded anchorage bar.	68
Figure 5–15. Results of welded anchorage bar component test: (a) stress-strain curve; (b) fractured anchorage bar.	68
Figure 5–16. Calibrated detailed model of welded anchorage bar component test.	69
Figure 5–17. Interaction of axial force and bending moment for welded #11 anchorage bar with reduced ductility under eccentric loading.....	70
Figure 5–18. Comparison of experimental and computed results for (a) vertical load and (b) horizontal reaction from front brace beam at end column tops (OMF specimen).	71
Figure 5–19. Section views of OMF model near the peak vertical load.	72
Figure 5–20. Deflected shape of OMF specimen prior to anchorage bar fracture.	72
Figure 5–21. Concrete damage for OMF specimen prior to anchorage bar fracture.	72
Figure 5–22. Concrete damage near top of center column for OMF specimen after anchorage bar fracture: (a) photograph; (b) contours of computed damage index.	73

Figure 5–23. Anchorage bar fracture in OMF model: (a) perspective view; (b) section through bottom anchorage bars on bottom link plates.....	73
Figure 5–24. Bending moment and axial force interaction for anchorage bar of OMF model.	74
Figure 5–25. Comparison of experimental and computed results for (a) vertical load and (b) horizontal reaction from brace beams at end column tops (SMF specimen).	75
Figure 5–26. Anchorage bar fracture in SMF model: (a) perspective view; (b) section through bottom anchorage bars on bottom link plates.....	76
Figure 5–27. Bending moment and axial force interaction for anchorage bars of SMF specimen.	76
Figure 5–28. Deflected shape of SMF specimen prior to anchorage bar fracture.....	77
Figure 5–29. Concrete damage for SMF specimen prior to anchorage bar fracture.	77
Figure 5–30. Section views of SMF model at the peak vertical load.....	77
Figure 5–31. Concrete damage on right end column of SMF specimen: (a) photograph; (b) contours of computed damage index.....	77
Figure 5–32. Influence of span length on computed vertical load-displacement response: (a) OMF specimen and (b) SMF specimen.	79
Figure 6–1. Energy-based analysis of sudden column loss.....	82
Figure 6–2. Load-displacement relationships for static loading and sudden column loss compared with applicable gravity loading: (a) OMF specimen; (b) SMF specimen.	83

LIST OF TABLES

Table 3–1. Average material properties of reinforcing bars.....	10
Table 5–1. Finite element models used to illustrate the influence of key factors on the computed responses.	54
Table 6–1. Normalized ultimate capacities and dynamic increase factors for OMF and SMF specimens with prototype span lengths.	83

LIST OF ACRONYMS AND ABBREVIATIONS

Acronyms

ACI	American Concrete Institute
AISC	American Institute of Steel Construction
ASCE	American Society of Civil Engineers
ERDC	U.S. Army Engineer Research and Development Center
NIST	National Institute of Standards and Technology
OMF	Ordinary Moment Frame
PCI	Precast/Prestressed Concrete Institute
SDC	Seismic Design Category
SMF	Special Moment Frame

Unit Abbreviations

ft	foot
in	inch
kip	1000 lbf
kN	kilonewton
ksi	kip per square inch
lbf	pound-force
m	meter
mm	millimeter
MPa	megapascal
psf	pound-force per square foot
psi	pound-force per square inch

Chapter 1

INTRODUCTION

1.1 BACKGROUND

In May of 1968, a gas explosion blew out a load bearing wall on the 18th floor of the Ronan Point tower block in London, causing a progression of failures that resulted in the collapse of an entire corner of the 22-story precast concrete building (Griffiths et al. 1968; Delatte 2009). This event provided an impetus for the development of design approaches to prevent such cases of disproportionate collapse. Elliott and Jolly (2013, Chapter 9) present a summary of design approaches for disproportionate collapse mitigation, with application to multi-story precast concrete structures. One such approach is the tie force method, an indirect design approach that requires minimum levels of strength and continuity in the connections between the various components of a structure. However, this approach does not consider the ductility of the ties, and thus does not ensure that the loads can actually be redistributed as large deformations develop following a local failure. The alternative load path method is a direct design approach that requires structural analysis to demonstrate explicitly the adequacy of the structural system to redistribute loads following a local failure. This approach requires characterization of the nonlinear behavior and ductility of structural components and connections, which can involve mechanisms such as arching action and catenary action.

Experimental data from structural assemblies and systems under local failure scenarios, such as column removal, are indispensable in characterizing the complex nonlinear behaviors whereby alternative load paths can be developed. Experimental data are also critical for validation of models used to represent such behaviors in analysis of structural systems. To address the need for such experimental data and associated modeling capabilities, the National Institute of Standards and Technology (NIST) is carrying out a comprehensive analytical and experimental research program to study the vulnerability of multi-story building structures to disproportionate collapse. As part of this research, ten-story prototype buildings have been designed with various structural systems, including steel frame, cast-in-place concrete frame, and precast concrete frame buildings. Moment-frame assemblies representing portions of these structural systems have been tested at full scale under simulated column removal. Sadek et al. (2010) described testing and analysis of steel moment-frame assemblies, while Lew et al. (2011) described testing and analysis of cast-in-place concrete moment-frame assemblies. This report focuses on precast concrete moment-frame assemblies.

Experimental data on the disproportionate collapse resistance of precast concrete structures have been quite limited. As summarized by Elliott and Jolly (2015), several experimental studies have investigated the effectiveness of tie forces in precast concrete floor slabs at redistributing loads through catenary action (e.g., Regan 1974, Schultz et al. 1977, Engström 1990). Recently, Nimse et al. (2014, 2015) tested one-third scale precast concrete frame assemblies under a column removal scenario, comparing the performance of monolithic connections, cast-in-place (“wet”) connections, and field-bolted (“dry”) connections. Kang and Tan (2015) performed testing of half-scale precast concrete frame assemblies with cast-in-place connections under simulated column removal, comparing the performance of specimens with different reinforcement details in the joints. These recent reduced-scale assembly tests (Nimse et al.

2014, 2015; Kang and Tan 2015) considered rectangular beams with clear span to depth ratios of approximately nine, which is comparable to the clear span to depth ratio of beams in the cast-in-place concrete assemblies tested previously by Lew et al. (2011). However, much deeper spandrel beams are common for exterior frames in precast concrete construction. The focus of this study is on spandrel beams designed as part of an exterior moment frame, with moment connections formed by field-welding of steel link plates between embedded plates in the columns and embedded angles in the beams. Experimental data on the performance of such systems under column removal scenarios were previously unavailable.

1.2 SCOPE OF STUDY

The study reported herein included both full-scale testing and finite-element analysis of two precast concrete moment-frame assemblies, which represented portions of the third-floor framing of prototype ten-story buildings. Each test specimen comprised three columns and two beams. While both specimens had moment-resisting beam-to-column connections, one specimen was designed as part of an ordinary moment frame, and the other was designed as part of special moment frame. The specimens were subjected to monotonically increasing vertical displacement of the unsupported center column to observe their behavior under a simulated column removal scenario, which included the development of flexural action and arching action. Each test was continued beyond the ultimate capacity of the assembly, to characterize the failure modes and collapse mechanisms that developed. Detailed finite element models of the test specimens were developed, and the models were able to capture the primary response characteristics of the assemblies, providing insight into their behavior and failure modes.

1.3 REPORT OUTLINE

The report describes the experimental and computational approaches used in this study and presents and compares the experimental and computational results for the two moment-frame assemblies. Chapter 2 describes the design of the two ten-story prototype precast concrete buildings, with special emphasis on the moment connections considered in this study. The section dimensions, reinforcing details, and connection details of the test specimens were taken directly from the prototype buildings. Chapter 3 describes the experimental program, including the experimental configuration, the loading procedure, and the instrumentation used for both specimens. Chapter 4 summarizes the test results, including the observed behavior and failure modes of each specimen, and presents the measured responses, including displacements, rotations, strains, and loads. Chapter 5 describes the finite element models used in the analysis of the test specimens and presents the results of these analyses, including comparisons with the experimental data. Chapter 6 presents an evaluation of the structural robustness of the moment-frame assemblies, comparing the loads sustained by the assemblies with the applicable gravity loading and analyzing the effect of sudden column loss using an energy-based procedure. Chapter 7 summarizes the results of this study and lists the main conclusions.

Chapter 2

PROTOTYPE BUILDINGS

2.1 DESIGN OF PROTOTYPE BUILDINGS

The National Institute of Standards and Technology (NIST), working with a panel of practicing structural engineers, developed the overall configuration and dimensions of two prototype 10-story precast concrete buildings for office occupancy. To examine the effectiveness of seismic design and detailing in resisting disproportionate collapse, alternative designs were developed for Seismic Design Category B (SDC B) and SDC D. A square plan layout was chosen for both prototype buildings, as shown in Figure 2–1(a), with plan dimensions of 150 ft × 150 ft (45.7 m × 45.7 m). As shown in Figure 2–1(b), the height of the first story is 15 ft (4.6 m), and the height of each upper story is 13 ft (4.0 m). The detailed design of the buildings was carried out by a consulting engineering firm (Kim et al. 2009a,b).

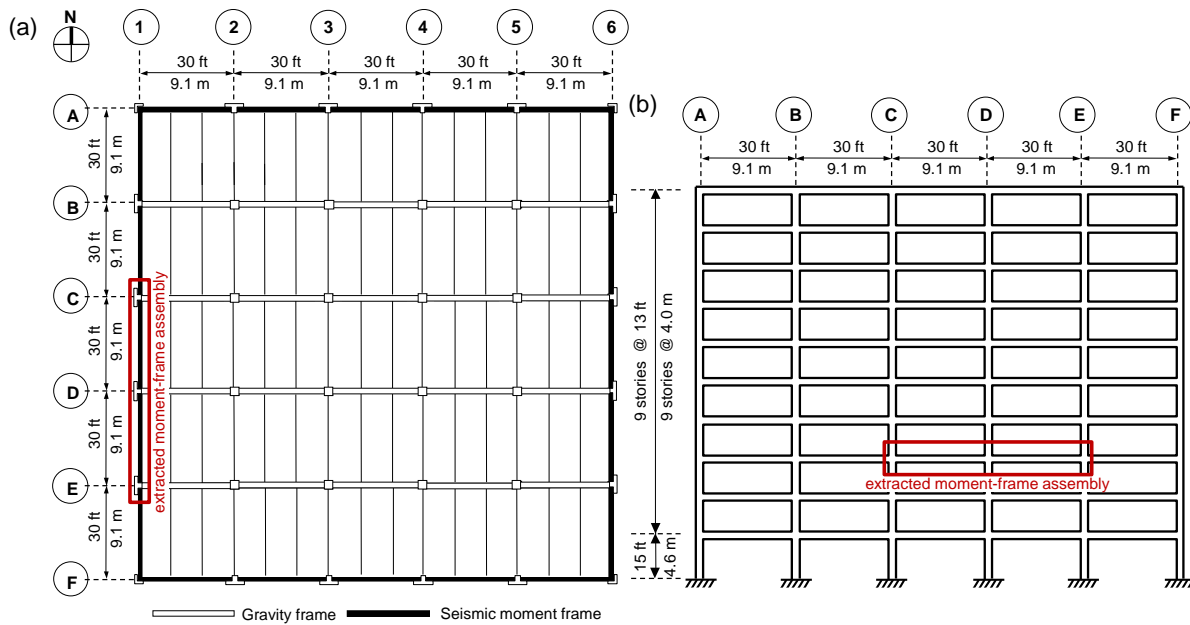


Figure 2–1. (a) Plan layout and (b) elevation view of prototype buildings.

Both buildings have perimeter moment frames designed to resist lateral loads, while the interior framing is designed for gravity loads only. The building designed for SDC B incorporates ordinary moment frames (OMFs), while the building designed for SDC D incorporates special moment frames (SMFs). The perimeter moment frames consist of spandrel beams connected to columns by steel link plates welded to embedded plates and angles (see Section 2.2). The interior gravity framing consists of simply supported inverted-T beams spanning between columns in the east-west direction. The floor system consists of cambered double-T members spanning in the north-south direction, with a concrete topping that varies in thickness from 3.5 in (89 mm) over the inverted-T beams to 2.5 in (64 mm) at midspan of the double-T members. The moment-frame assemblies considered in this study were extracted from perimeter moment frames in the north-south direction at the third-story level, as indicated in Figure 2–1.

The prototype buildings were designed according to ASCE 7-05 (ASCE 2005) for occupancy category II. A superimposed dead load of 10 psf (0.48 kN/m²) was considered in addition to the self-weight of the structure. Typical floors were designed for a live load of 100 psf (4.79 kN/m²), which was reduced in accordance with section 4.8 of ASCE 7-05 (ASCE 2005). The roof was designed for a live load of 25 psf (1.20 kN/m²). Seismic design of the OMF building was based on a location in Atlanta, Georgia, on Site Class C. Seismic design of the SMF building was based on a location in Seattle, Washington, on Site Class D. The design of the structural members was based on the requirements of the ACI 318-05 code (ACI 2005). The design of the beam ledges was based on the PCI Design Handbook (PCI 2004). Both the precast structural members and the concrete topping were designed using normal-weight concrete, with a specific weight of 150 lbf/ft³ (23.6 kN/m³). A compressive strength of 6000 psi (41.4 MPa) was specified for the precast structural members, and a compressive strength of 4000 psi (27.6 MPa) was specified for the concrete topping. A minimum yield strength of $f_y = 60$ ksi (414 MPa) was specified for the reinforcing bars.

Design of the structure was based on three-dimensional analyses of the buildings using a commercially available computer program for linear elastic analysis. All structural members except for the double-T floor members were included in the structural model, while lateral resistance was provided by the exterior columns and spandrel beams only. The floor system was modeled as a rigid diaphragm, and gravity loads on the floor system were applied directly to the supporting beams. To represent the construction sequence, in which welding of moment connections does not occur until after the self-weight loads are in place, the structure was analyzed in two steps. In the first analysis, dead loads were applied to a model without rigid frame connections between the beams and columns, with lateral restraints included to represent the erection bracing during construction. In the second analysis, the remaining load cases were applied to a model that included the rigid frame connections, without the lateral restraints. Final member and connection forces for design were obtained by combining the results from the two analyses, with appropriate load factors according to the applicable load combinations.

2.2 DESIGN OF MOMENT FRAMES

The exterior framing of the prototype buildings consists of columns and spandrel beams and is designed to provide the lateral load resisting system for the buildings. The spandrel beams are placed inside pockets in the exterior columns (Figure 2–2), and moment connections are established by welding steel link plates to steel angles embedded in the beams and to steel plates embedded in the columns. Moment connection details are shown in Figure 2–3 and Figure 2–4 for OMF connections and SMF connections, respectively. The steel column plates are embedded in the column concrete using AWS D1.1 Type B headed studs (AWS 2010). Anchorage reinforcing bars in the spandrel beams are welded to the steel angles embedded at the top and bottom of the beams. For both the OMF and SMF connections, class B splices are provided between the anchorage bars and the beam flexural reinforcement, to maintain continuity of the beam reinforcement through the connection, as required for precast concrete SMFs by Section 21.6.2 of ACI 318-05 (ACI 2005). The beam moment is transferred to the column by the coupling forces generated in the top and the bottom link plates. Torsional restraint for the spandrel beams is provided by torsion rods installed through sleeves in the beams and columns.

The precast concrete SMFs were designed in accordance with Sections 21.2 through 21.6 of ACI 318-05 (ACI 2005). As noted in the PCI Design Handbook (PCI 2004, Section 3.6.4), these provisions aim to produce structures with strong column, weak beam behavior. Section 21.3 of ACI 318-05 specifically

requires that flexural members of SMFs shall have a clear span not less than four times the effective depth. To comply with this requirement, the SMF spandrel beams have a reduced depth relative to the OMF spandrel beams. The clear span to depth ratio is 2.7 for the OMF spandrel beams and 4.2 for the SMF spandrel beams. Further details on the moment-frame assemblies considered in this study, including the member dimensions and reinforcement details, are provided in section 3.1.

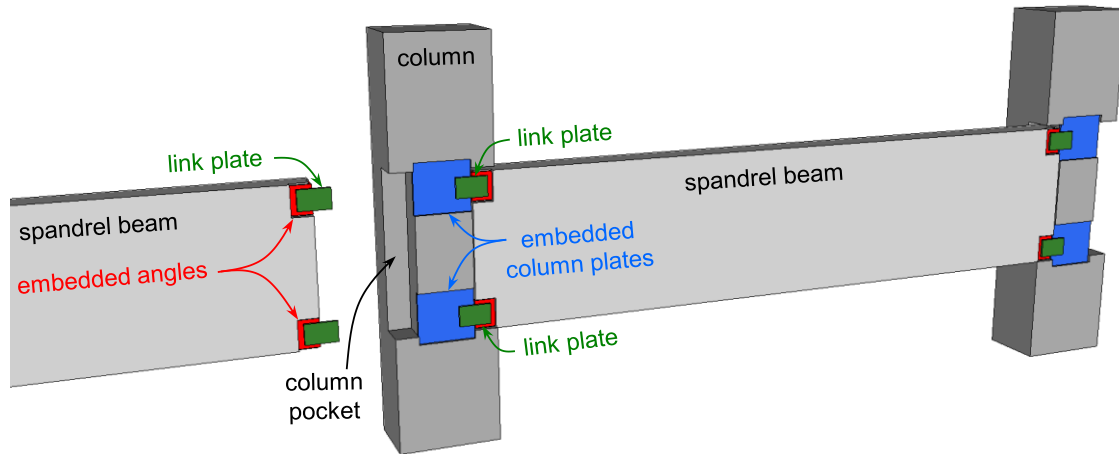


Figure 2–2. Perspective illustration of a perimeter moment frame showing link-plate connections and placement of spandrel beams within pockets in the columns.

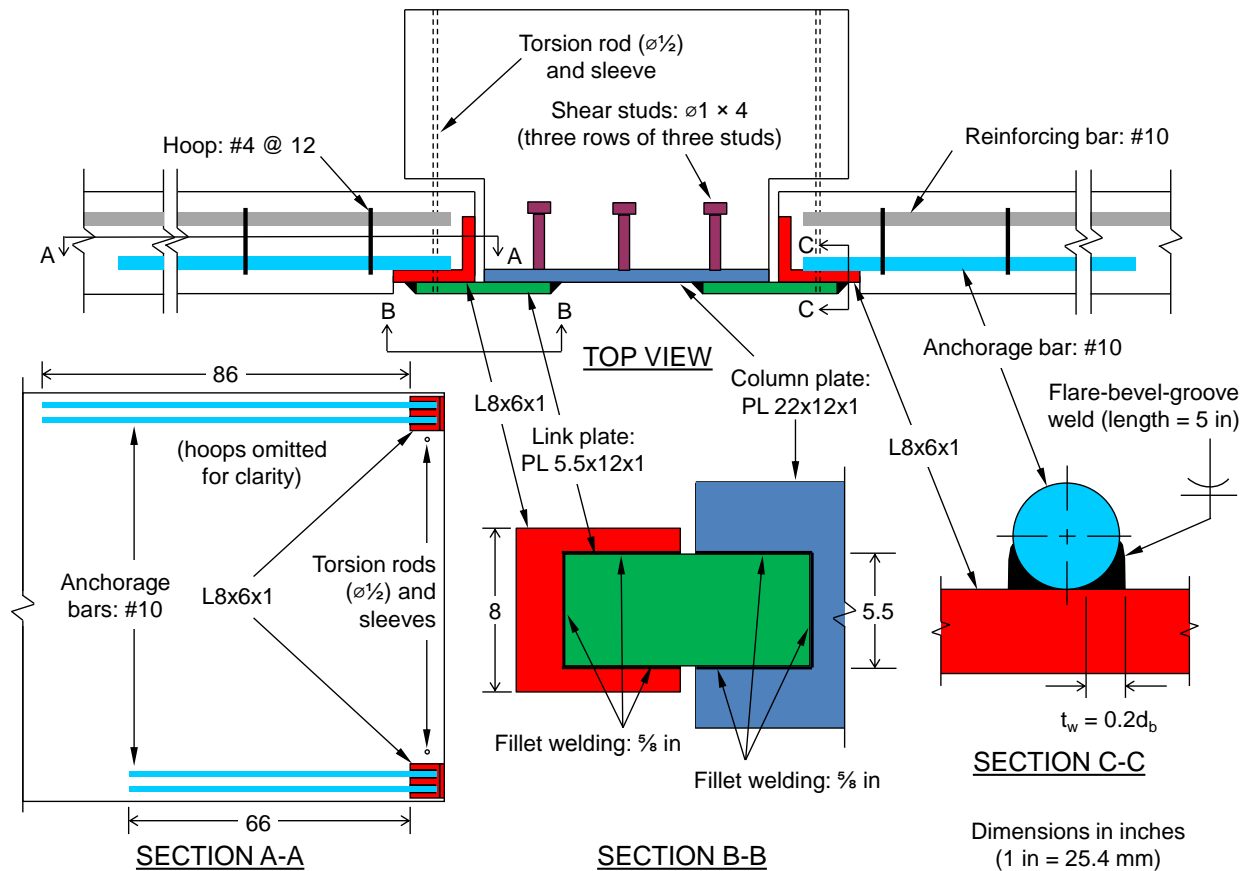


Figure 2–3. Ordinary moment frame (OMF) connection details.

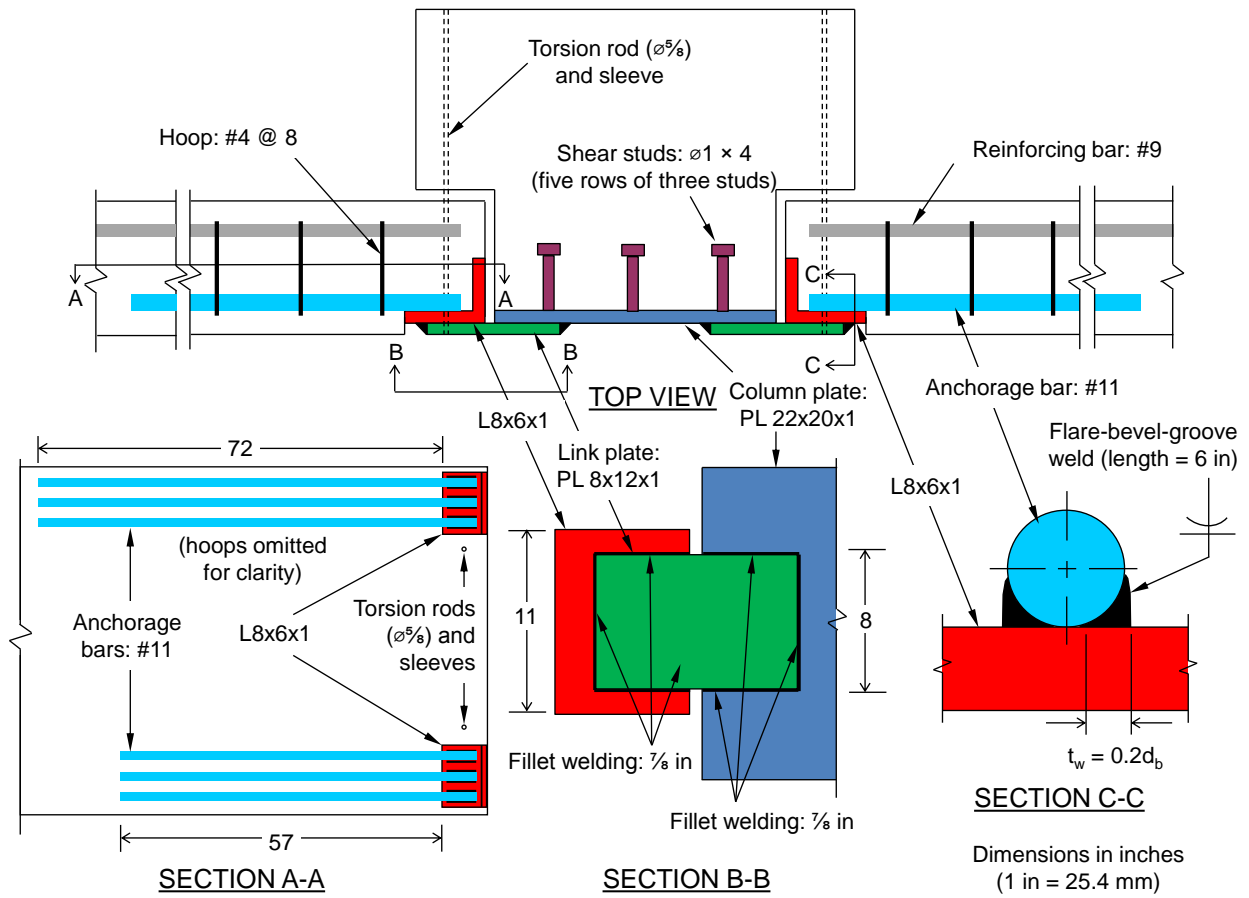


Figure 2-4. Special moment frame (SMF) connection details.

Chapter 3

EXPERIMENTAL PROGRAM

This chapter describes the overall experimental program, which includes the design of the test specimens, the experimental configuration, the loading procedure, and the instrumentation. The primary objectives of these tests were (1) to characterize the response of the precast concrete moment frames under a column removal scenario, particularly the capacity of the moment connections to transfer loads through flexural action and other mechanisms; and (2) to provide experimental data for validation of finite-element models to be used in evaluating the robustness of precast concrete structural systems. The test specimens were two-span moment-frame assemblies extracted from the third-floor framing system in the north-south direction (C1~E1) of the ten-story buildings described in Chapter 2 (see Figure 2–1). The specimen from the SDC B building was part of an ordinary moment frame (OMF), while the specimen from the SDC D building was part of a special moment frame (SMF). Throughout the remainder of this report, these two specimens are referred to as the OMF specimen and the SMF specimen, respectively. Section 3.1 describes the test specimens, including measured material properties. Section 3.2 describes the experimental configuration for both specimens, including boundary conditions and loading procedure. Section 3.3 presents the instrumentation for each of the two tests.

3.1 TEST SPECIMENS

Figure 3–1 and Figure 3–2 show member sizes and reinforcement details for the OMF specimen and the SMF specimen, respectively. The testing was conducted at the U.S. Army Engineer Research and Development Center (ERDC) in Vicksburg, Mississippi, and the span length of the test specimens was reduced from 30 ft (9.1 m) to 25 ft (7.6 m) to fit within the testing facility. Reducing the span length in this manner would be expected to cause the capacity of the specimens to increase. The effect of the shortened span length was evaluated using computational modeling and is discussed subsequently in Section 5.6.

The columns had a rectangular cross section (section A-A in Figure 3–1 and Figure 3–2), which was reduced to a T-shape in the connection regions to form pockets for the spandrel beams (section B-B in Figure 3–1 and Figure 3–2). Column longitudinal reinforcing bars were welded to 1 in (25 mm) thick steel plates at the bases of the end columns. The beams and columns were prefabricated off-site, and assembly of the test specimens, including welding of the link plates, took place at the ERDC testing facility. Figure 3–3 shows the precast concrete beams and columns prior to assembly.

The OMF specimen incorporated the OMF connection details shown in Figure 2–3, and the SMF specimen incorporated the SMF connection details shown in Figure 2–4. In this report, the *front* of each specimen denotes the surface on which the link plates were welded when making the moment connections, and the designations *left beam* and *right beam* correspond to the orientation of the beams when viewing the specimen from the front. As indicated in Figure 3–1 and Figure 3–2, the left beam was on the east side of the testing facility, and the right beam was on the west side.

The beams of the SMF specimen were inadvertently installed in an inverted orientation so that the longer anchorage bars were at the bottom of the beams rather than at the top as designed (see Figure 2–4). A slight misalignment of the torsion rod sleeves in the beams and columns also prevented installation of the torsion rods for the SMF specimen. As discussed in Section 5.1, the implications of these errors were investigated using computational modeling and were found to have only a slight influence on the response of the SMF specimen. The experimental results obtained for the SMF specimen are therefore believed to quite closely represent the behavior of the specimen as designed.

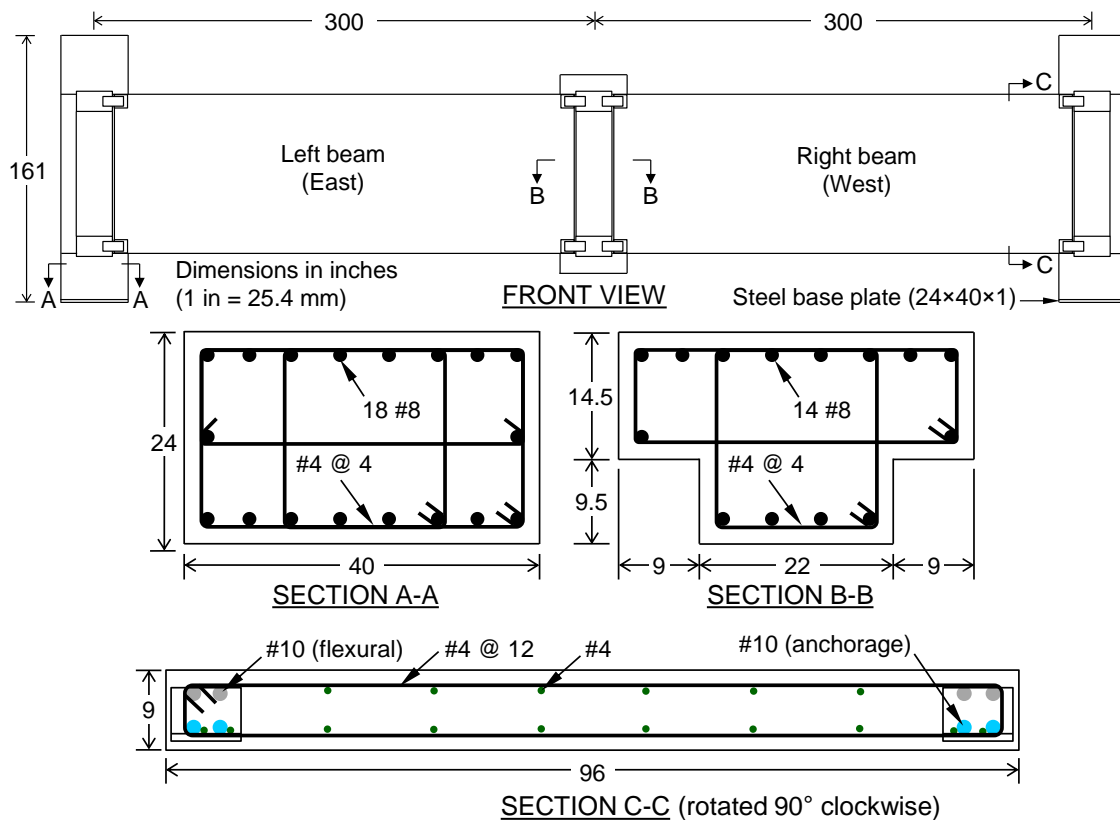


Figure 3–1. Details of OMF specimen.

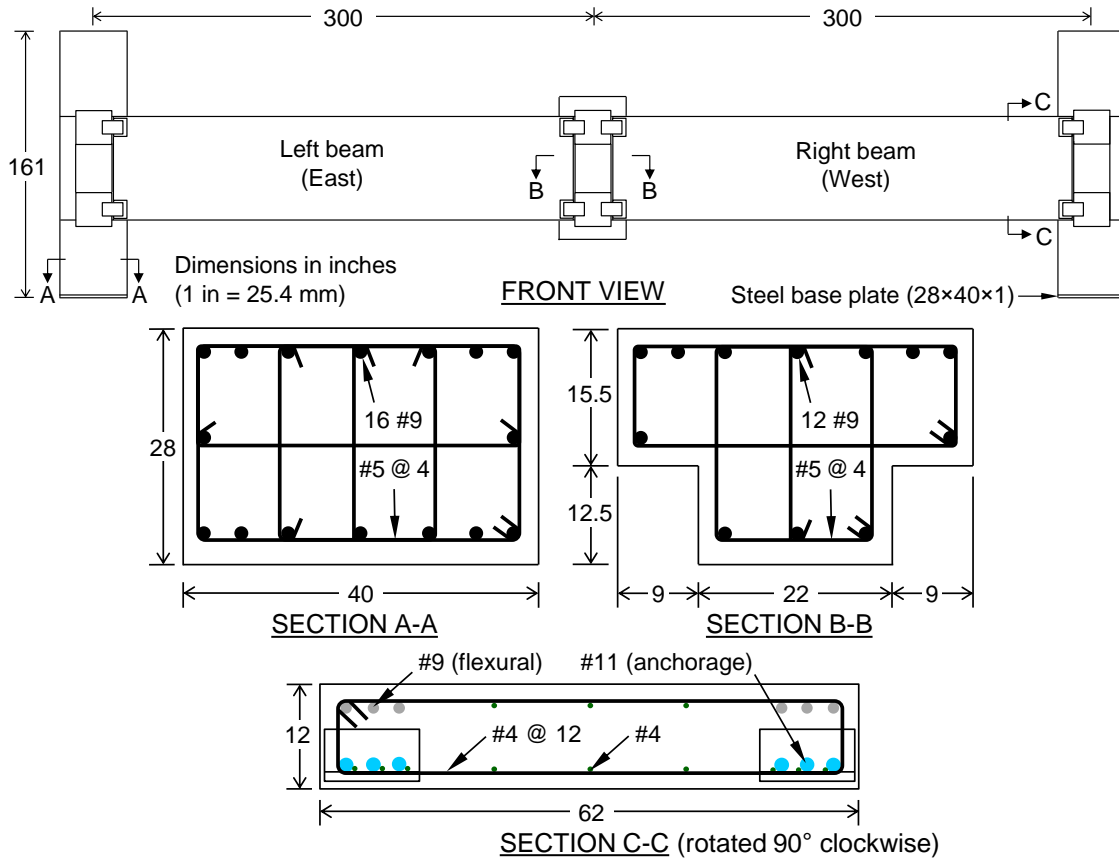


Figure 3–2. Details of SMF specimen.



Figure 3–3. Precast concrete beams and columns prior to assembly.

All precast beams and columns were designed with concrete having a specified compressive strength of 6000 psi (41.4 MPa) and with ASTM A706 Grade 60 reinforcing bars having a minimum specified yield strength of 60 ksi (413.7 MPa). The average measured 28-day compressive strength of concrete was 5785 psi (40 MPa) and the average 28-day splitting tensile strength of concrete was 469 psi (3.2 MPa). Table 3.1 shows average values of the measured mechanical properties of the reinforcing bars used to fabricate the specimens. All plates and angles were made of ASTM A36 steel with a minimum yield strength of 36 ksi (250 MPa). The torsion rods were ASTM A193 Grade B7 bolts with a minimum tensile strength of 125 ksi (862 MPa).

Table 3–1. Average material properties of reinforcing bars.

Bar Size	Yield Strength, f_y ksi (MPa)	Tensile Strength, f_u ksi (MPa)	Fracture Strain
No. 4 [†]	74 (510)	106 (731)	26 % ¹
No. 8 [†]	73 (503)	108 (745)	24 % ²
No. 9 [†]	71 (490)	109 (752)	21 % ²
No. 10 [†]	69 (476)	103 (710)	24 % ²
No. 11 [†]	70 (483)	105 (724)	22 % ²
No. 10 [‡]	64 (441)	90 (621)	15 % ³
No. 11 [‡]	68 (469)	95 (655)	15 % ³

[†] Data from coupon test

[‡] Data from rebar test

¹ Gage length: 1 in (25 mm)

² Gage length: 2 in (51 mm)

³ Gage length: 8 in (203 mm)

3.2 EXPERIMENTAL CONFIGURATION

The experimental configuration, which was essentially the same for both specimens, is illustrated in Figure 3–4 and Figure 3–5. The base plates of the end columns were welded to 2 in (51 mm) thick steel plates atop concrete footings. Each footing was clamped down to the strong floor using post-tensioning bars. The tops of the end columns were restrained by a steel frame to simulate the bracing effect provided by the upper stories in a multi-story building. This frame consisted of two W16x67 beams spanning between the end columns, with W14x82 cross beams at the inside and outside face of each end column. The W16x67 beams rested on support beams bolted to a reaction frame, as shown in Figure 3–5. Round steel bars between steel plates were used to provide contact between the cross beams and the column faces, thus restraining horizontal movements of the end column tops.

Vertical load was applied to the unsupported center column using a hydraulic actuator with a capacity of 400 kip (1779 kN) and a stroke of 20 in (508 mm). The actuator was mounted to a reaction frame as shown in Figure 3–5. The load was applied under displacement control at a rate of 1 in/min (25 mm/min) through a steel loading plate, and horizontal movements of the steel loading plate were restrained by four columns positioned at the corners of the plate as shown in Figure 3–4. These columns were welded to base plates, which were bolted to the strong floor of the laboratory. A special roller bearing support arrangement at the four corners of the plate allowed free vertical displacement of the plate along the four columns. A collar on the underside of the loading plate fit over the top of the center column and restrained its horizontal movement, thereby keeping the applied load in the vertical direction and limiting eccentrically applied loading. A pair of steel plates on the front and back sides of the center column restrained out-of-plane motion at the lower end of the center column (see Figure 3–4). Round steel rods were used to provide contact between these steel plates and the column faces. A pair of columns straddling each beam at midspan provided lateral bracing for the beams. Figure 3–6 shows photographs of both specimens assembled in the experimental configuration prior to testing.

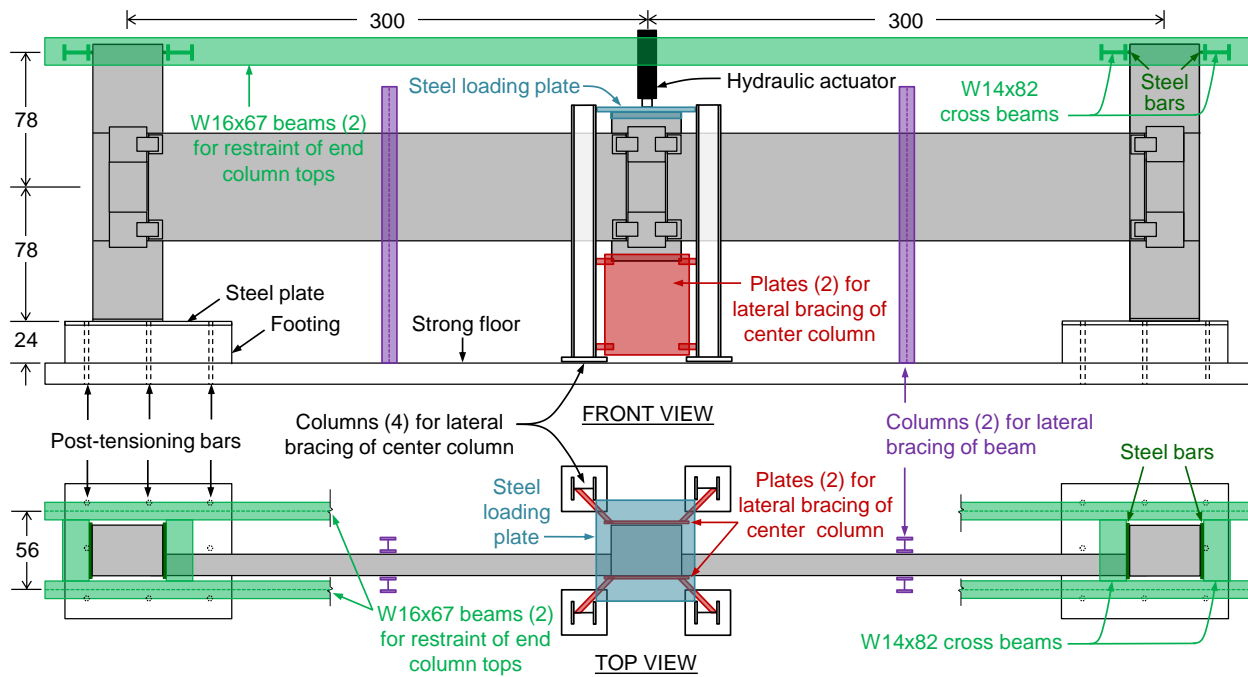


Figure 3-4. Front and top views of experimental configuration.

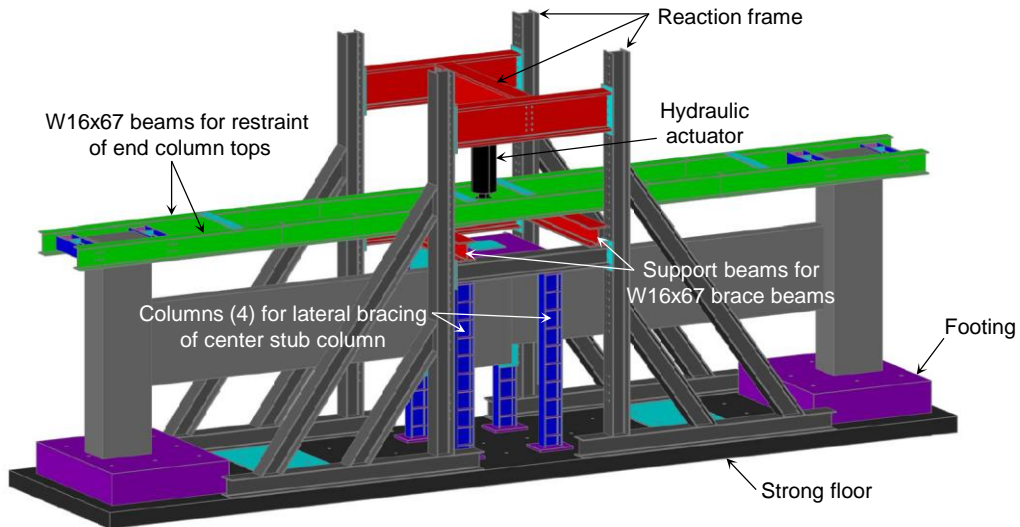


Figure 3-5. Oblique view of experimental configuration including reaction frame.

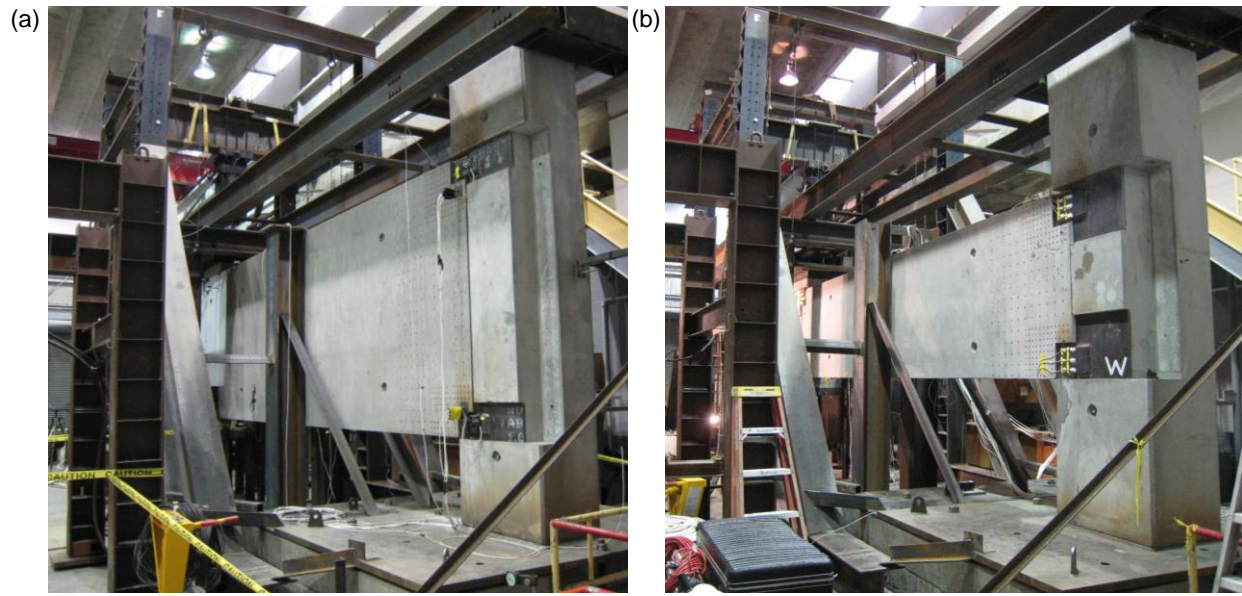


Figure 3-6. Assembled specimens prior to testing: (a) OMF specimen; (b) SMF specimen.

3.3 INSTRUMENTATION

Figure 3-7 shows photographs of selected instrumentation as installed on the test specimens. The vertical load applied by the hydraulic actuator was measured using a load cell with a capacity of 400 kip (1779 kN), shown in Figure 3-7(a). Displacement measurements included vertical displacements of the center column and the beams and horizontal displacements of the end columns. Two types of transducers were used to measure displacements: spring-loaded, string-type displacement potentiometers, as shown in Figure 3-7(b), with a range of 72 in (1830 mm) and an accuracy of 0.001 in (0.025 mm), and LVDTs (linear variable differential transformers, also known as linear variable displacement transducers), as shown in Figure 3-7(c), with a range of 6 in (152 mm) and an accuracy of 0.005 in (0.127 mm). LVDTs were used only to measure horizontal displacements of the end columns for the OMF specimen, while all other displacements were measured using string potentiometers. To measure the rotation of the beam ends, digital inclinometers were attached to the top surface of the beams, as shown in Figure 3-7(d).

In addition to the types of instruments shown in Figure 3-7, both specimens were extensively instrumented with electrical resistance strain gauges attached to the surfaces of selected steel components. Uniaxial strain gauges were attached to the reinforcing bars and anchorage bars in the beams, to the link plates connecting the beams and columns, and to the W16x67 beams used to brace the tops of the end columns. For the SMF specimen uniaxial strain gauges were also attached to shear studs welded to a column plate and embedded in the column concrete. For the OMF specimen, surface strains on some of the link plates were measured with 45° strain rosettes, which are assemblies of three strain gauges differing in orientation by 45° to enable determination of horizontal, vertical, and shear strains. Strain gauges on reinforcing bars and shear studs were installed at the precasting plant prior to concrete placement, while surface-mounted strain gauges on the link plates and brace beams were installed at the testing facility. The SMF specimen was tested first, and differences between the instrumentation layouts for the OMF specimen and the SMF specimen reflect changes made as a result of experience gained from testing of the SMF specimen. A total of 67 channels of data were recorded for the OMF specimen, and 77 channels of data were recorded for the SMF specimen.

The location and designation of specific instrumentation for each specimen are provided in the following subsections. In the designation of instrumentation, the prefix “D” is used to denote displacement gauges (both string potentiometers and LVDTs), the prefix “R” is used to denote rotation gauges (inclinometers), and the prefix “S” is used to denote strain gauges. The estimated uncertainty in the measured load, displacement, rotation, and strain data is $\pm 1\%$. In addition to these measurements, three digital video cameras were used to record each test. A camera was aligned with each of the three columns to capture deformations, surface cracking, spalling, and component failure in the region surrounding each moment connection.

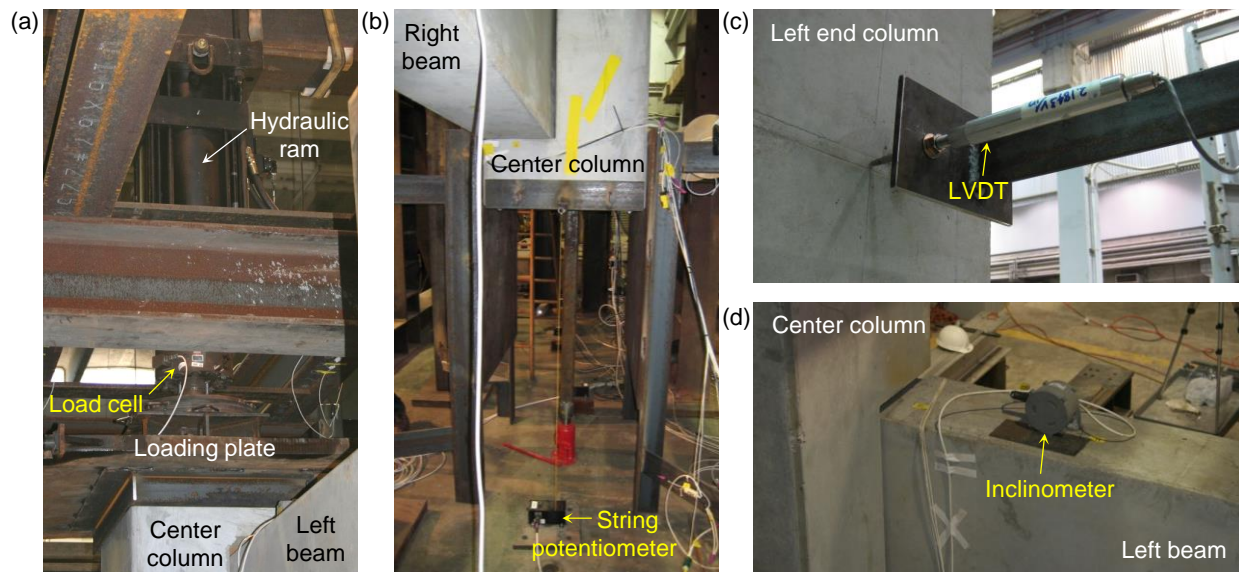


Figure 3–7. Instrumentation: (a) load cell; (b) string potentiometer; (c) LVDT; (d) inclinometer.

3.3.1 OMF Specimen

Figure 3–8 shows the transducers used to measure displacement and rotation for the OMF specimen. String potentiometers measured the vertical displacement of the center column (D85 and D86) and the vertical displacement near midspan of each beam (D83 and D88), while two LVDTs (D81 and D90) measured the horizontal displacement of the end columns at beam mid-height. Four inclinometers (R91–R94) measured the rotation at each end of the two beams.

Figure 3–9 shows the strain gauges installed on the anchorage bars of the OMF specimen. Strain gauges were installed at locations where tensile forces were expected in the anchorage bars, and the gauges were installed in pairs on opposite sides of the bars, to enable measurement of flexure as well as axial strains in the bars. Parentheses indicate strain gauges installed on the back side of the bars (i.e., the side further from the link plates), as is shown more clearly in the section views. Figure 3–10 shows the strain gauges installed on flexural reinforcing bars of the OMF specimen at midspan of each beam. These gauges were also installed in pairs on opposite sides of the bars as shown in the section views. Figure 3–11 shows the strain gauges installed on the link plates of the OMF specimen and at midspan of the front brace beam that spans between the tops of the end columns. Strain rosettes on the link plates are shown as groups of three strain gauges differing in orientation by 45° (e.g., gauges S112–S114 on the upper right link plate of the left beam).

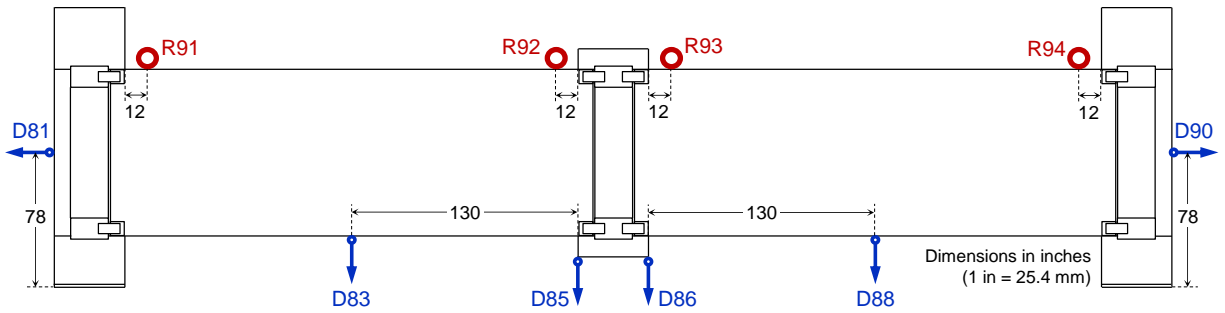


Figure 3-8. Displacement and rotation transducers (OMF specimen).

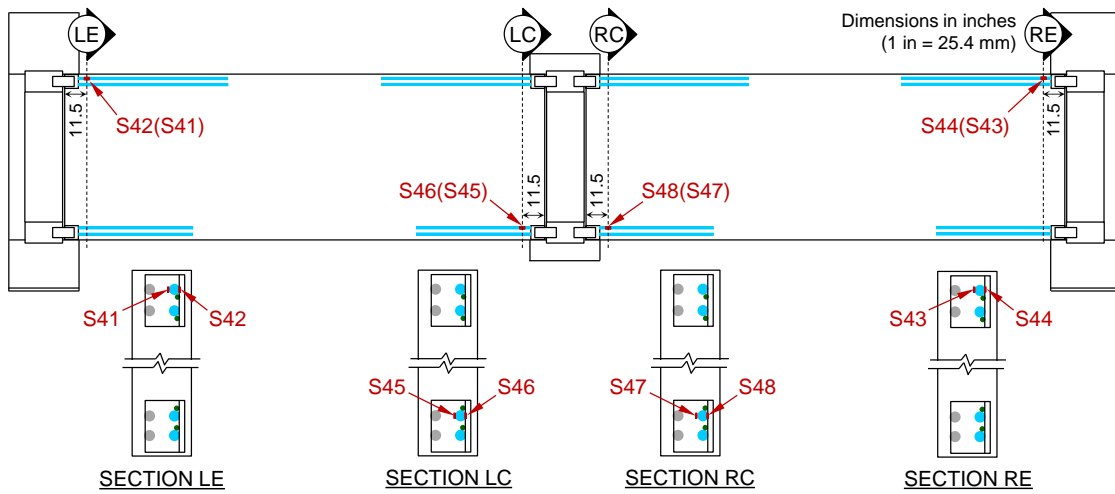


Figure 3-9. Strain gauges on anchorage bars (OMF specimen).

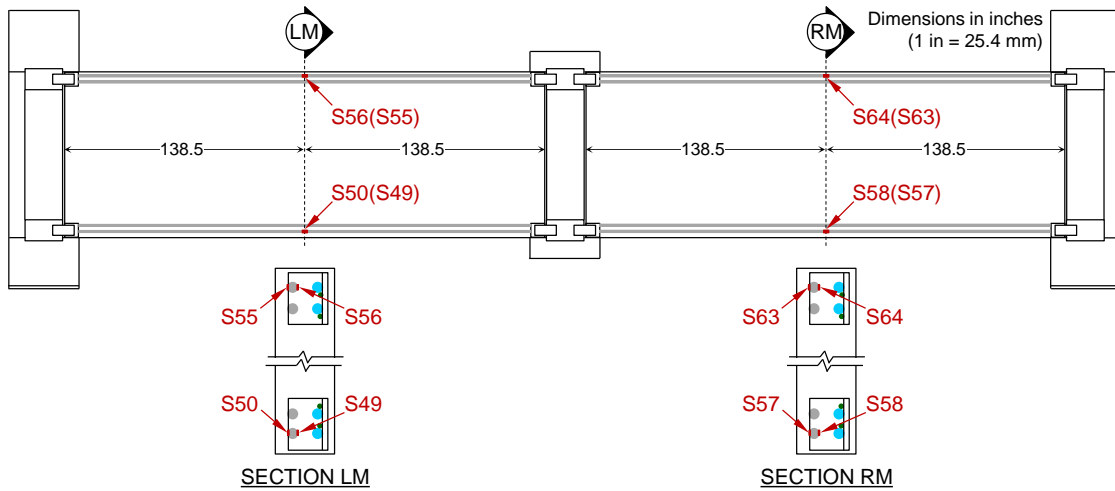


Figure 3-10. Strain gauges on flexural reinforcing bars (OMF specimen).

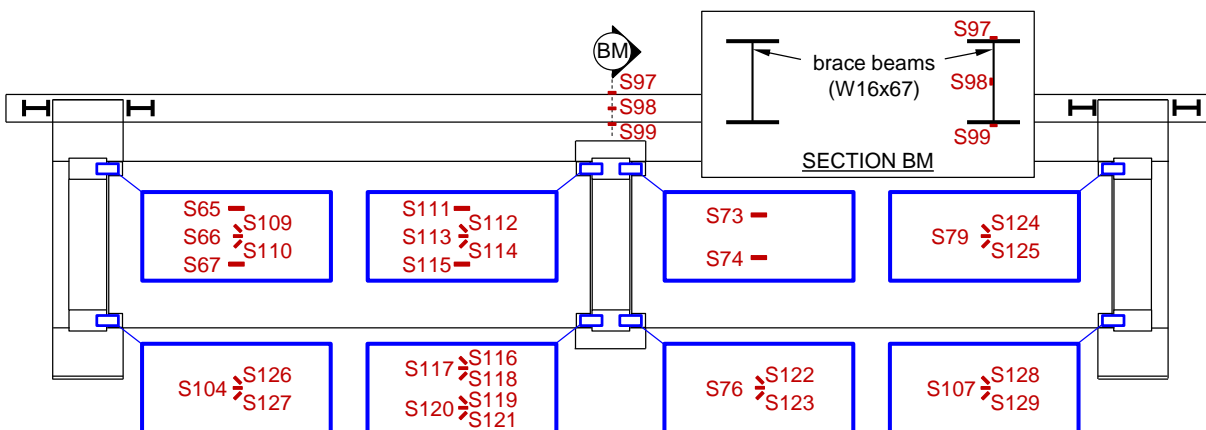


Figure 3–11. Strain gauges on link plates and brace beam (OMF specimen).

3.3.2 SMF Specimen

Figure 3–12 shows the transducers used to measure displacement and rotation for the SMF specimen. String potentiometers were used for all displacement measurements. Vertical displacements were measured at the center column (D85 and D86) and along the two beams near $\frac{1}{4}$ span (D82 and D89), midspan (D83 and D88), and $\frac{3}{4}$ span (D84 and D87). Horizontal displacements of the end columns were measured at beam mid-height (D81 and D90) and at the footings (D109 and D110). Four inclinometers (R91–R94) measured the rotation at each end of the two beams.

Strain gauges were installed on the anchorage bars of the SMF specimen in a similar configuration as shown for the OMF specimen in Figure 3–9. However, because the beams of the SMF specimen were inadvertently installed in an inverted orientation (see Section 3.1), the strain gauges were not at the intended locations, and no meaningful data was obtained from these gauges. Figure 3–13 shows strain gauges installed on the flexural reinforcing bars of the SMF specimen near midspan of each beam. These gauges were installed in pairs on opposite sides of the bars as shown in the section views. Additional strain gauges on flexural reinforcing bars at section RM (midspan of right beam) either malfunctioned or provided inconsistent data and are not presented in this report. Figure 3–14 shows strain gauges installed on shear studs welded to the upper column plate at the left end column. Four shear studs were instrumented, each with a pair of strain gauges on opposite sides to capture flexure in the studs. Figure 3–15 shows the uniaxial strain gauges installed on the link plates of the SMF specimen and at midspan of the two brace beams that span between the tops of the end columns. Strain gauges were installed on both brace beams for the SMF specimen, while only the front brace beam was instrumented for the OMF specimen because of limitations on the number of data acquisitions channels available.

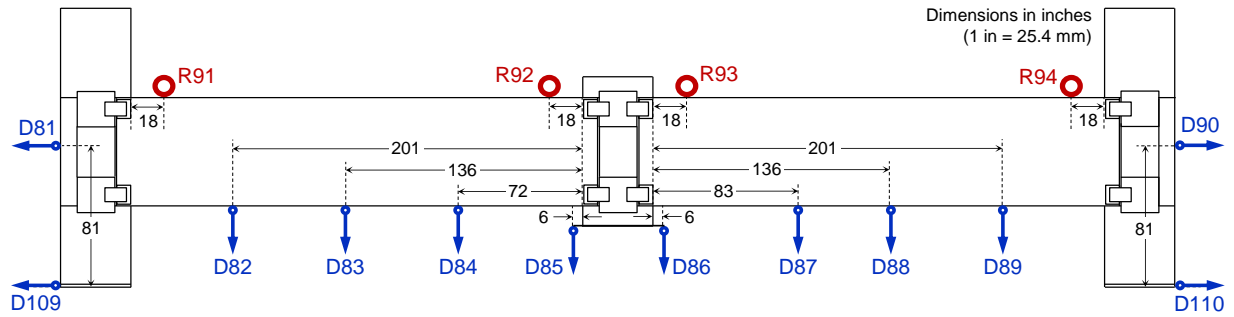


Figure 3-12. Displacement and rotation transducers (SMF specimen).

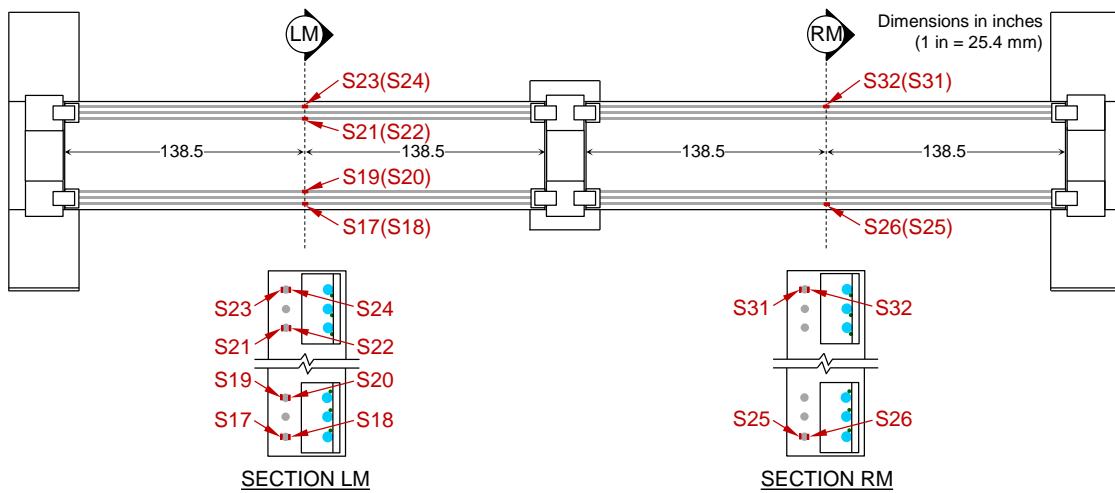


Figure 3-13. Strain gauges on flexural reinforcing bars (SMF specimen).

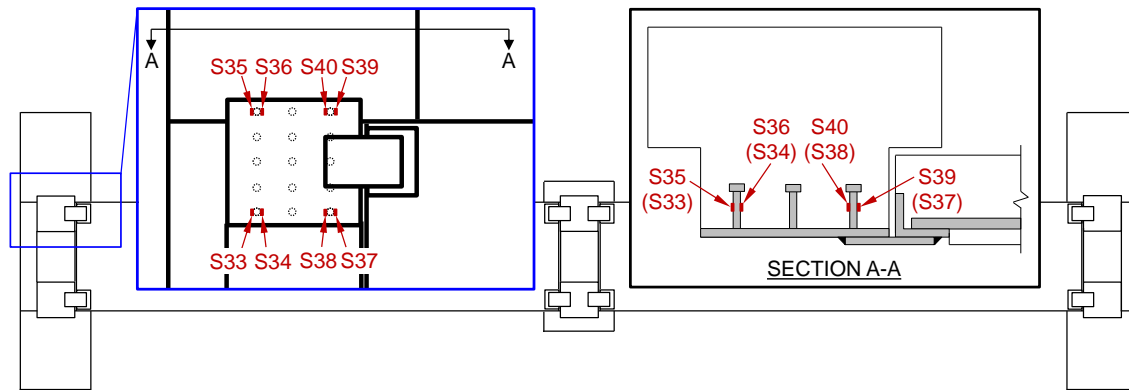


Figure 3-14. Strain gauges on shear studs (SMF specimen).

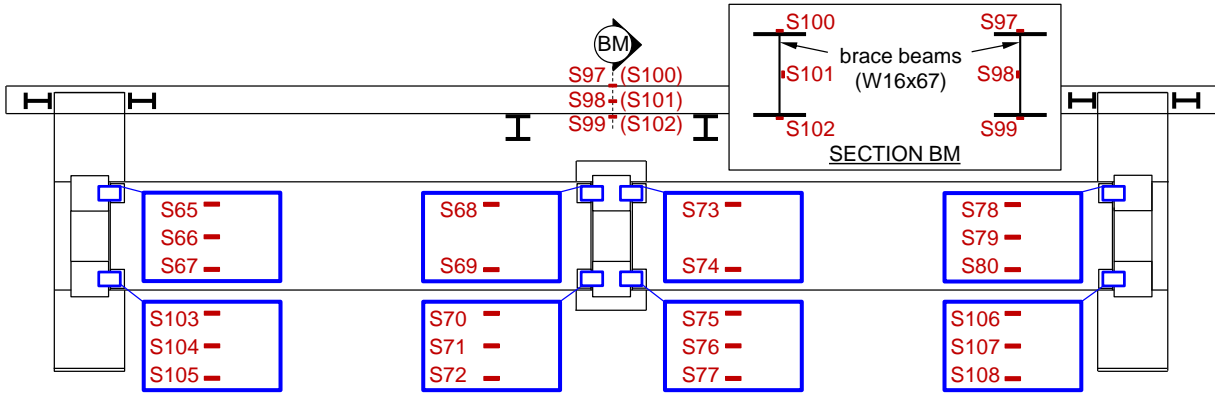


Figure 3–15. Strain gauges on link plates and brace beams (SMF specimen).

This page intentionally left blank.

Chapter 4

EXPERIMENTAL RESULTS

This chapter presents experimental results for both the OMF and SMF specimens, tested under a column removal scenario as described in Chapter 3. These results include the observed behavior and failure modes of each specimen, along with measurements recorded during the experiments. Such measurements include the applied vertical load, vertical displacements of the center column and beams, horizontal displacements of the end columns, rotations at the beam ends, and strains in reinforcing bars, anchorage bars, link plates, and other steel components. Both the observed behavior and the measured data provide insights into the performance of the specimens under the column removal scenario. Sections 4.1 and 4.2 present experimental results obtained from the OMF and SMF specimens, respectively. Finally, Section 4.3 presents a summary and discussion of the key experimental findings.

4.1 OMF SPECIMEN

4.1.1 Observed Behavior and Failure Modes

Figure 4–1 shows a plot of the applied vertical load versus the vertical displacement of the center column for the OMF specimen. The vertical displacement of the center column, denoted by Δ , was obtained as an average of the displacements measured on each side of the center column (D85 and D86 in Figure 3–8). Displacement measurements are further discussed subsequently in Section 4.1.2. The labeled points in Figure 4–1 correspond to images in Figure 4–2 that show the progression of damage with increasing Δ . The images in Figure 4–2 were obtained from the three video cameras that recorded the test, one camera aligned with each of the three columns. Each row of three images in Figure 4–2 corresponds to the same value of Δ , which was estimated by tracking and scaling of vertical displacements in the central image. The uncertainty in the displacement estimates in Figure 4–2 is approximately 0.2 in (5.1 mm).

The vertical load vs. displacement response of the specimen was essentially linear up to point *a* in Figure 4–1, when concrete cracking occurred in the beams around the upper link plates, as shown Figure 4–2(a), and the stiffness of the specimen decreased. Further reductions in stiffness occurred as concrete cracks formed in the end columns at the lower column plates, as shown in Figure 4–2(b) and (c). The load reached an initial peak of 133 kip (592 kN) at a displacement of $\Delta = 2.87$ in (73 mm) and then began to decrease. A drop in the load at point *d* was associated with detachment of the upper column plate from the left end column. The column plate was attached to the column by shear studs (see Figure 2–3), and detachment of the column plate was associated with concrete cracking on the left end column, as indicated in Figure 4–2(d). This is shown more clearly in Figure 4–3, which shows the opening of cracks and spalling of concrete around the detached column plate under continued loading.

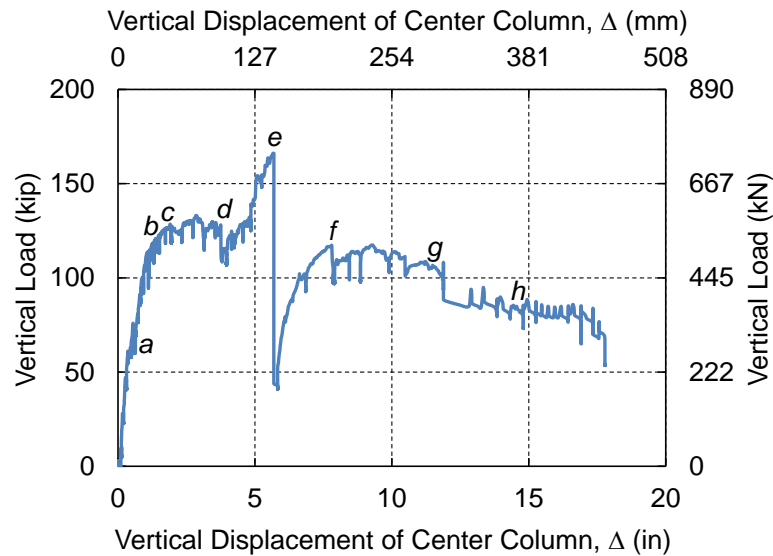


Figure 4–1. Applied vertical load vs. vertical displacement of center column for OMF specimen (labeled points correspond to images in Figure 4–2).

After the drop in load at point *d* in Figure 4–1, the load began to increase steeply again up to point *e*, reaching an ultimate peak of 166 kip (738 kN) at a displacement of $\Delta = 5.66$ in (144 mm). Between points *d* and *e*, the specimen developed additional capacity through arching action, with the top corner of each beam bearing against the center column and the bottom corner of each beam bearing against the end columns. Such bearing was evidenced by narrowing of the gaps between the beams and columns, with associated cracking and spalling of concrete in regions where bearing forces were developed, as indicated for the center column and the right end column in Figure 4–2(d). Bearing of the left beam against the left end column occurred somewhat later than at the other locations and is indicated in Figure 4–2(e).

After reaching the ultimate load at point *e*, the load dropped sharply to only 25 % of its peak value. This drop in load was associated with fracture of the #10 anchorage bars welded to the bottom connecting angle on the left side of the center column (see connection detail in Figure 2–3). Fracture of the anchorage bars was evidenced by widening of the gap between the left beam and the center column, as indicated in Figure 4–2(e). The anchorage bars fractured at the end of the flare-bevel-groove weld on the connecting angle, as is evident in Figure 4–4, which shows the connecting angle and welded anchorage bars recovered from the specimen after the test.

After fracture of the anchorage bars, the load increased steeply as the specimen developed additional resistance through arching action, reaching 70 % of the ultimate load at point *f*. A drop in load at point *f* was associated with fracture of the lower torsion bar at the right end column, accompanied by diagonal cracking and shear deformation of the right end column below beam level. Shear deformation of the right end column continued throughout the remainder of the test, and Figure 4–5 shows the final state of damage viewed from several angles. Another drop in load at point *g* was associated with fracture of the lower torsion bar at the left end column, accompanied by shear deformation of the left end column below beam level, which continued throughout the remainder of the test. Shear deformation of the left end column occurred with extensive concrete spalling, and Figure 4–6 shows the final state of damage viewed from several angles.

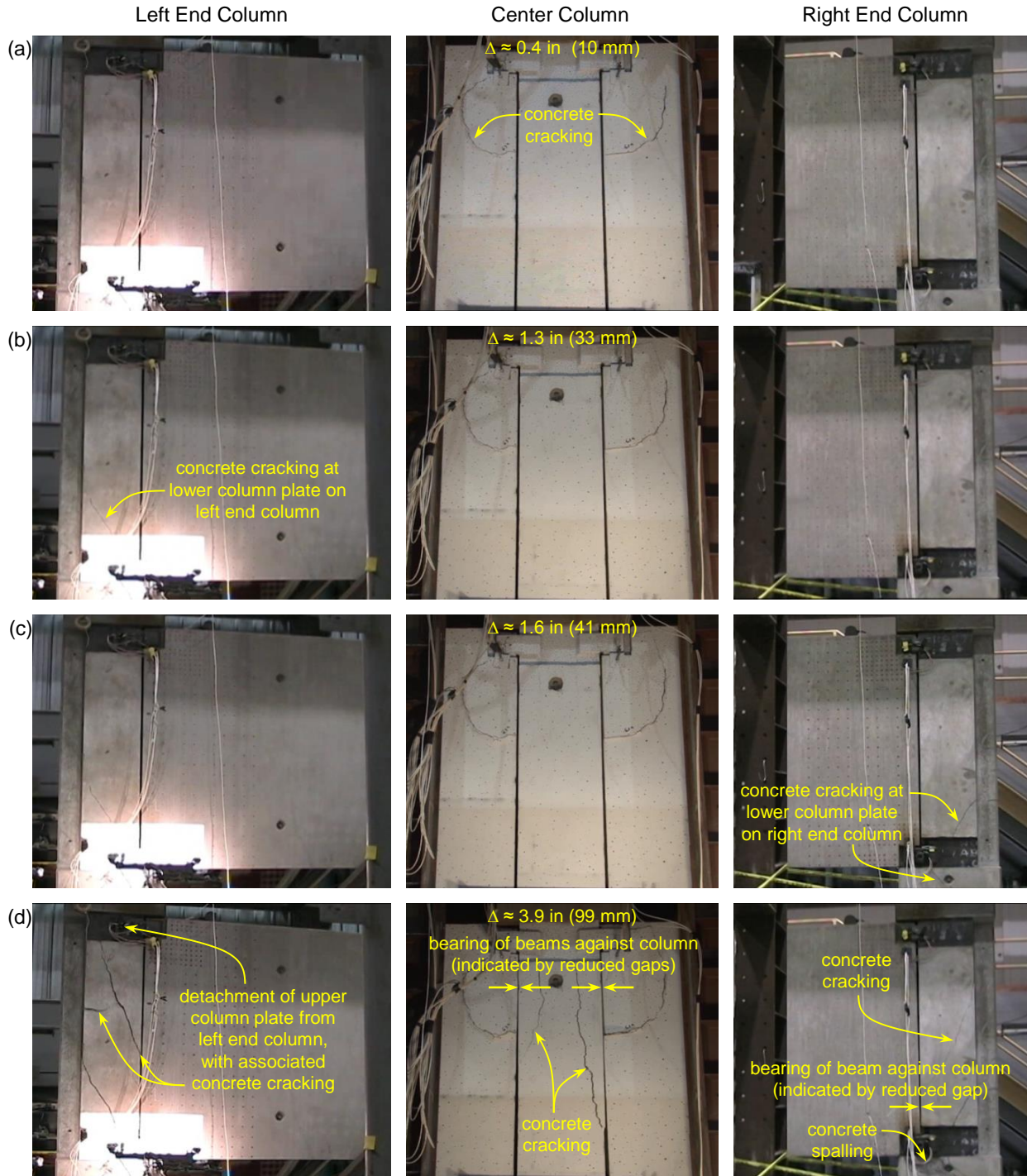


Figure 4-2. Progression of damage for OMF specimen (images correspond to labeled points in Figure 4-1).

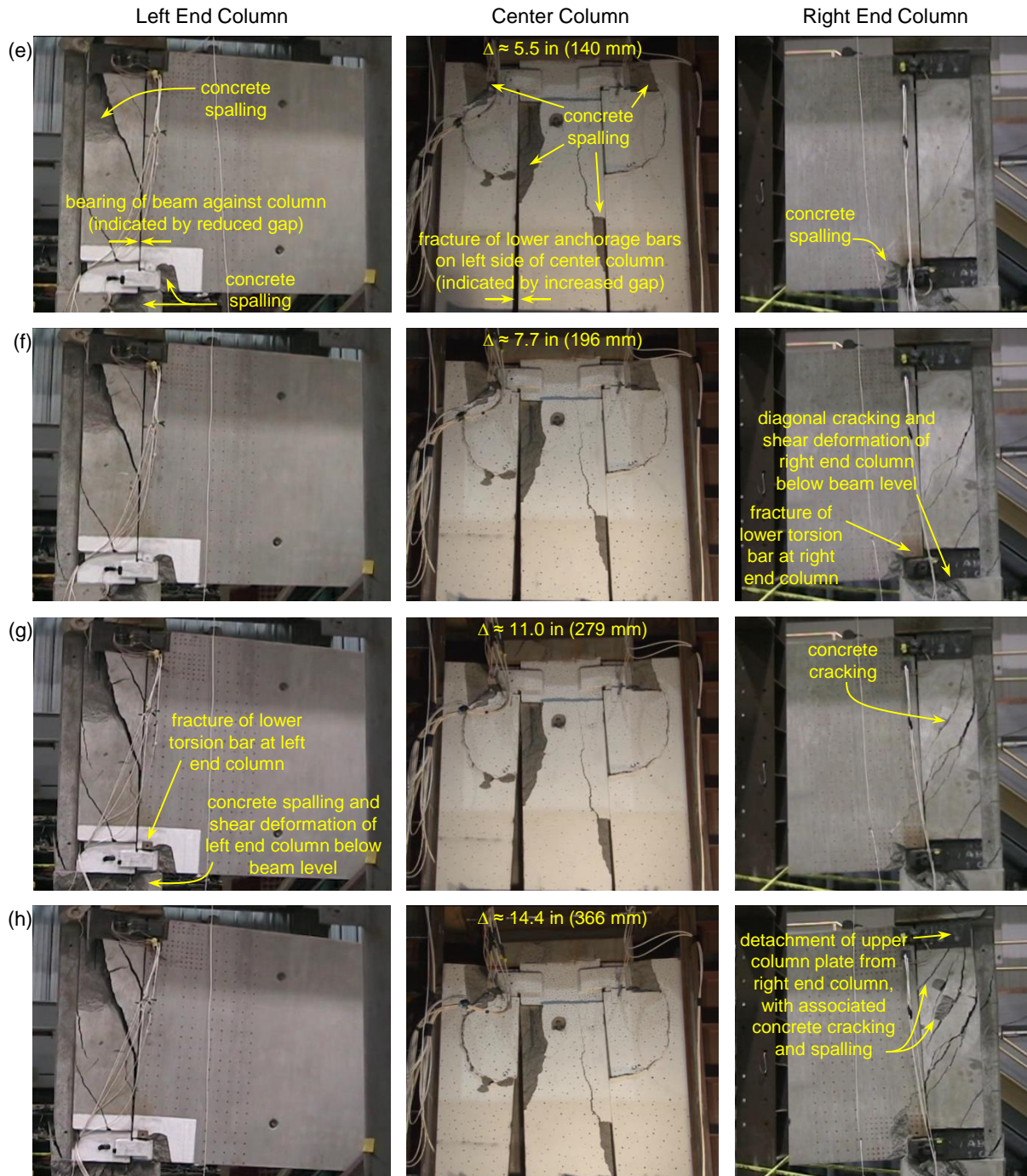


Figure 4–2 (continued). Progression of damage for OMF specimen (images correspond to labeled points in Figure 4–1).



Figure 4-3. Detachment of upper column plate from left end column (OMF specimen).



Figure 4-4. Fractured anchorage bars from lower left connection to center column (OMF specimen).



Figure 4-5. Final damage to right end column viewed from several angles (OMF specimen).



Figure 4-6. Final damage to left end column viewed from several angles (OMF specimen).

At point *h* in Figure 4–1, the upper column plate detached from the right end column, similar to the failure observed previously on the left end column at point *d*. As indicated in Figure 4–2(h), this failure was accompanied by cracking and spalling of concrete on the right end column, which is shown more clearly in Figure 4–7. Large deformations of the link plates were observed, as shown in Figure 4–8, which were indicative of extensive yielding. Concave out-of-plane bending occurred at the upper link plate [Figure 4–8(a)], where tensile forces caused the beam to pull away from the column, and convex out-of-plane bending occurred at the lower link plate [Figure 4–8(b)], where compressive forces caused the beam to bear against the column. Finally, as the load continued to decrease and large chunks of concrete spalled from the specimen, the test was terminated at a center column displacement of $\Delta = 17.8$ in (452 mm).



Figure 4–7. Detachment of upper column plate from right end column (OMF specimen).

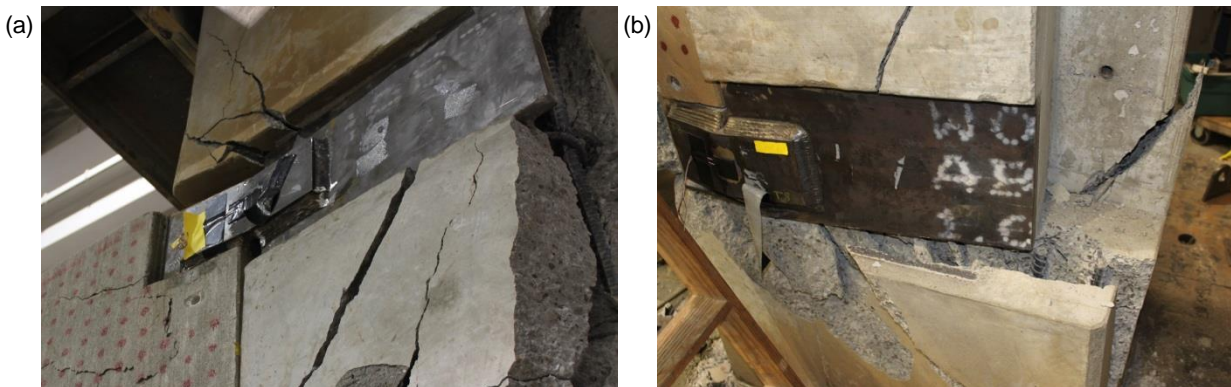


Figure 4–8. Out-of-plane bending of link plates at right end column: (a) upper link plate; (b) lower link plate (OMF specimen).

4.1.2 Displacement and Rotation Measurements

Figure 4–9 shows the vertical load plotted against the vertical displacements at (a) the center column and (b) midspan of the beams. Figure 4–10 shows the corresponding displacement profile of the beams at selected values of the center column displacement Δ , where Δ is an average of the two displacement measurements on each side of the center column (D85 and D86). Figure 4–10 was obtained by plotting displacements from Figure 4–9 at the transducer locations shown in Figure 3–8. Figure 4–9 and Figure 4–10 show good agreement between the measurements of symmetrically placed displacement transducers up

to the ultimate load at $\Delta = 5.66$ in (144 mm), indicating that symmetry was largely maintained to this point. Some asymmetry of the displacement profile is evident after the ultimate load, with larger displacements on the left side of the center column than on the right side. This asymmetry is a result of the anchorage bar fractures on the lower left side of the center column, which permitted in-plane rotations of the center column, as is evident in Figure 4–2(e) – (h).

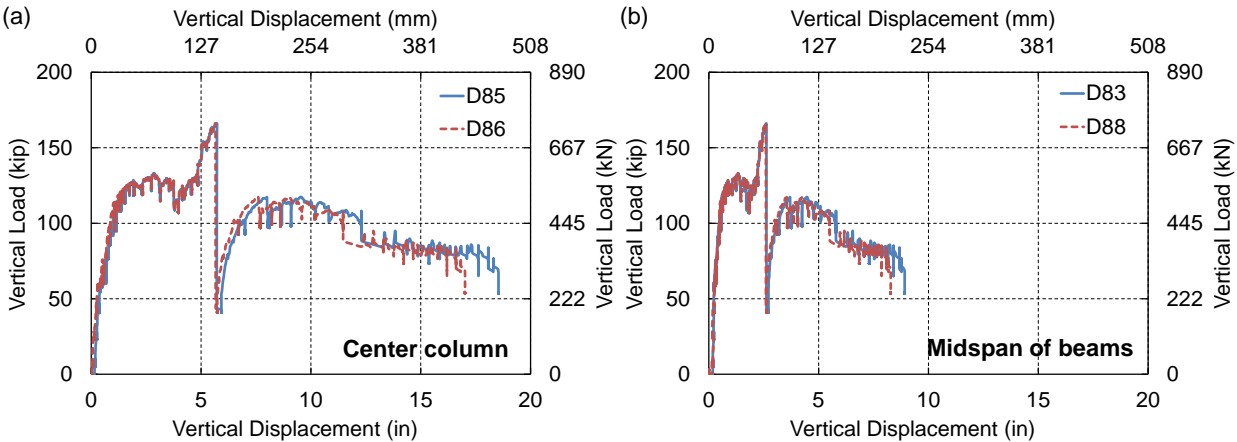


Figure 4–9. Applied vertical load vs. vertical displacements at (a) center column and (b) midspan of beams (OMF specimen).

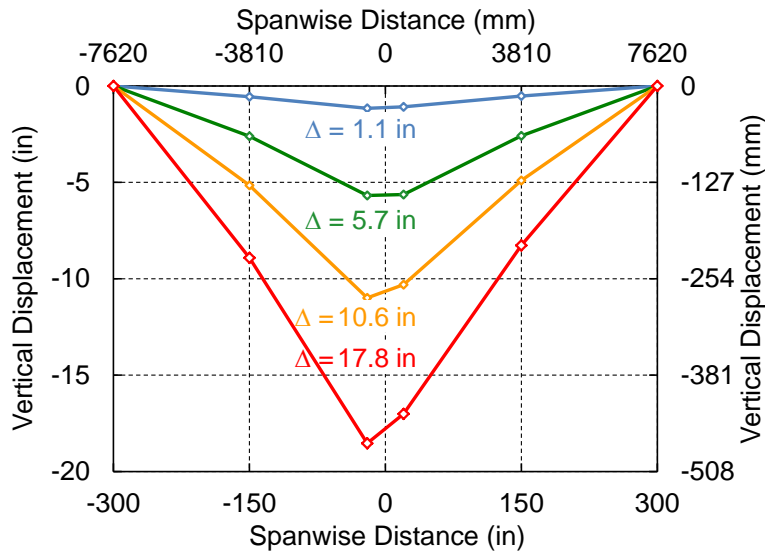


Figure 4–10. Vertical displacement profile of beams corresponding to indicated vertical loads (OMF specimen; displacements magnified).

Figure 4–11 shows the measured rotation at both ends of the right beam (R93 and R94, see Figure 3–8) plotted against the vertical displacement of the center column. Rotation measurements from the left beam (R91 and R92) are not presented because these inclinometers appeared to have malfunctioned. Figure 4–11 shows the measured rotations plotted with the beam chord rotation, calculated as $\theta = \tan^{-1}(\Delta/L)$, where $L = 300$ in (7620 mm) is the centerline-to-centerline beam span. This plot shows that the measured rotations were essentially linearly proportional to the vertical displacement of the center column, Δ . The measured rotations at the two ends of the beam span differed from the calculated beam chord rotation by

less than 0.20° (0.0035 rad) for most of the test, with the rotation at the center column being slightly greater and the rotation at the end column being slightly less. This implies that the beam essentially rotated as a rigid body, with most of the deformations localized at the beam-to-column connections.

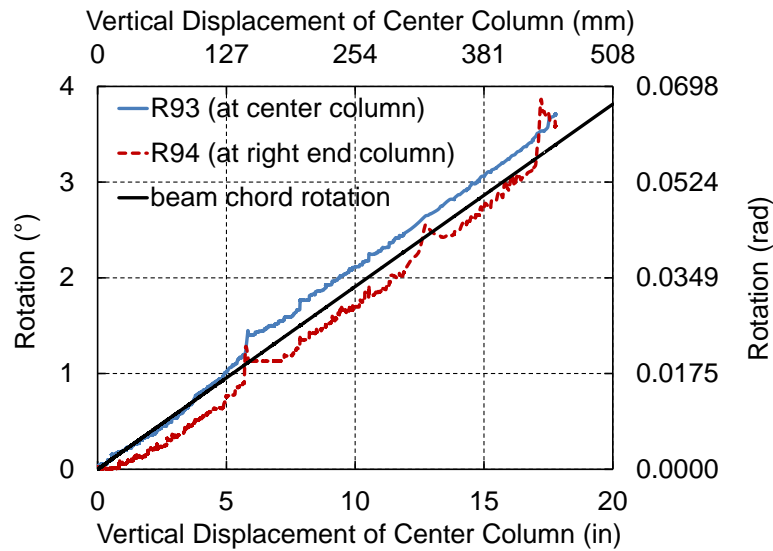


Figure 4–11. Beam end rotations (OMF specimen).

Figure 4–12 shows the horizontal displacement of the end columns at beam mid-height, with positive values signifying outward displacement, plotted against the vertical displacement of the center column. The average of the two measurements, which cancels out rigid-body motions, is also plotted for comparison. Initially, both end columns displaced slightly inward, reaching an average inward displacement of 0.044 in (1.1 mm) prior to the onset of arching action. After the onset of arching action at a center column displacement of $\Delta \approx 4.0$ in (100 mm) (point *d* Figure 4–1), both end columns displaced to the left by about 0.17 in (4.4 mm), indicating a slight rigid-body rotation of the end columns, which were linked at their tops by brace beams (see Figure 3–4). During this rigid-body rotation, the average inward displacement decreased slightly as a result of arching action. After fracture of anchorage bars at a center column displacement of $\Delta = 5.66$ in (144 mm) (point *e* in Figure 4–1), the motion of the right column changed directions, and both end columns moved outward. The measured displacement from both gauges froze at an outward displacement of about 0.15 in (3.8 mm) and did not provide meaningful data after this point. Horizontal displacements after this point were estimated from the video images in Figure 4–2, with an estimated uncertainty of ± 0.1 in (± 2.5 mm) determined by comparing displacements obtained from the video images with the those measured by the displacement gauges. The displacements estimated from the video images are shown as solid circles in Figure 4–12 and indicate that both end columns continued to displace outward as a result of arching action. An average outward displacement of 0.75 in (19 mm) was estimated at a center column displacement of $\Delta = 14.4$ in (366 mm), which corresponds to point *h* in Figure 4–1.

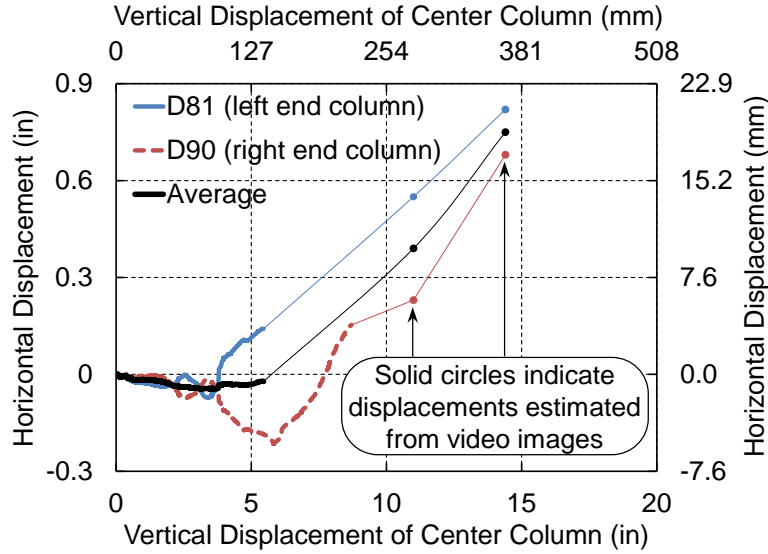


Figure 4–12. Horizontal displacement of end columns at beam mid-height (OMF specimen).

4.1.3 Strain Measurements

Strain measurements in the anchorage bars of the OMF specimen are presented in Figure 4–13 and Figure 4–14, where Figure 4–13 shows measured strains in the upper anchorage bars at the end columns and Figure 4–14 shows measured strains in the lower anchorage bars at the center column. Locations of the strain gauges, which were installed in pairs on opposite sides of each bar, were shown in Figure 3–9, along with the section designations (LE, RE, LC, and RC) referenced in Figure 4–13 and Figure 4–14. All gauges on the anchorage bars recorded tensile strains (positive values), which was expected, since gauges were installed on the upper bars at the end columns, where negative bending moments developed in the beams, and on the lower bars at the center column, where positive bending moments developed.

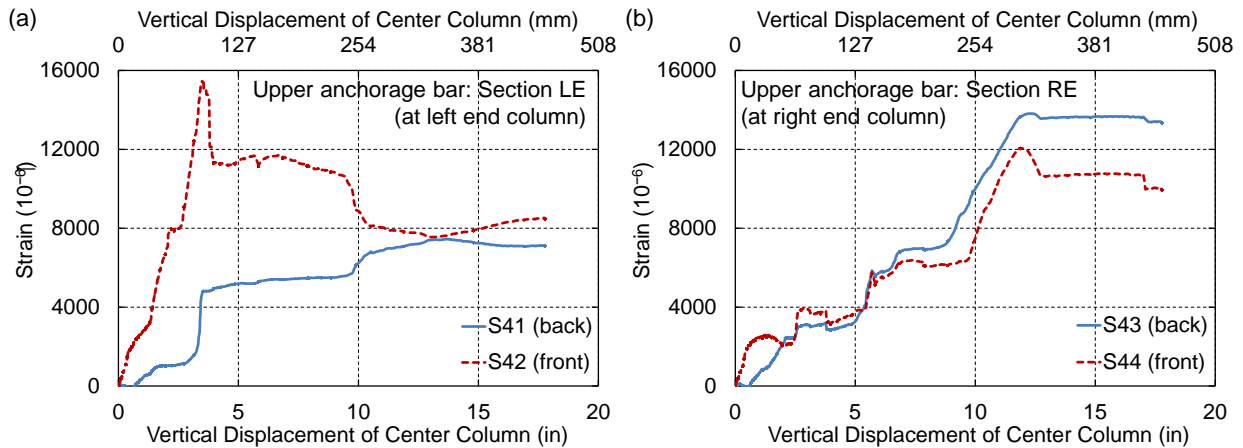


Figure 4–13. Strain in upper anchorage bars at end columns (OMF specimen).

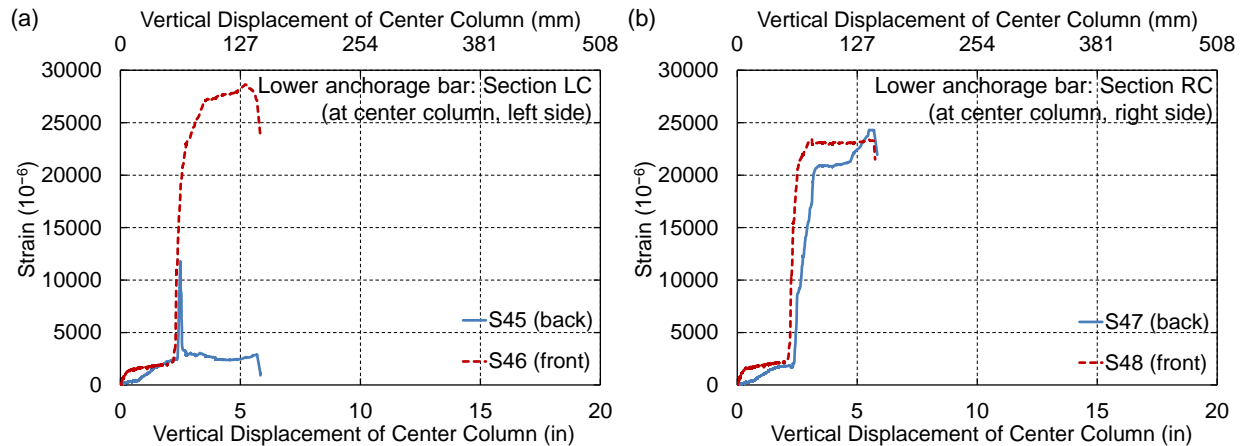


Figure 4-14. Strain in lower anchorage bars at center column (OMF specimen).

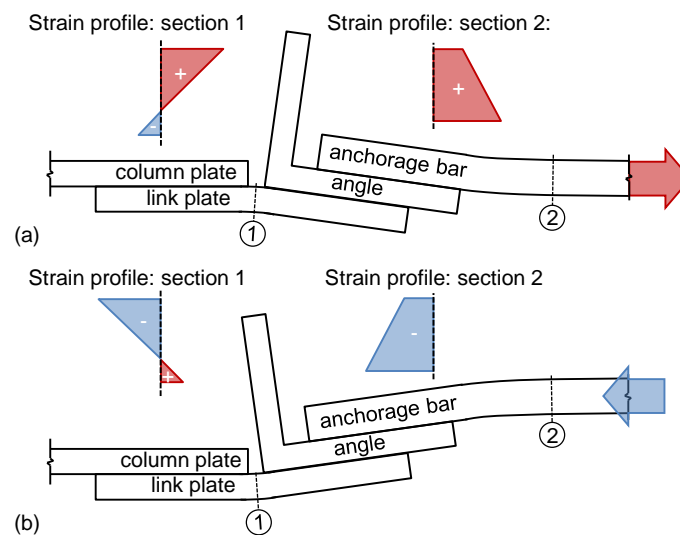


Figure 4-15. Deformation and strain profile in anchorage bar and link plate of OMF specimen: (a) tension in anchorage bar; (b) compression in anchorage bar.

Larger tensile strains were observed on the front side of each anchorage bar, at least initially, indicating out-of-plane bending of the bars with curvature away from the front of the specimen, as illustrated in Figure 4-15(a). This out-of-plane bending resulted from the eccentricity between the tensile force in the anchorage bar and the equilibrating tensile force developed in the link plate. At locations where the anchorage bars were subjected to compression, bending occurred in the opposite direction, as illustrated in Figure 4-15(b). The deformation and strain profiles in Figure 4-15 are further discussed subsequently in relation to strain measurements on the link plates.

Figure 4-16 and Figure 4-17 present the axial force and the out-of-plane bending moment in the anchorage bars, respectively, calculated from the measured strains in Figure 4-13 and Figure 4-14. Figure 4-18 presents corresponding interaction diagrams of axial force plotted against bending moment. These axial force and bending moment values were calculated by assuming a linear strain profile across the bar (illustrated in Figure 4-15), using the measured stress-strain curve for a #10 bar (from tensile testing reported in Table 3-1) to calculate the corresponding stress profile, and numerically integrating

the stress profile over the cross section of the bar. Open circles on the curves of calculated bending moment and axial force indicate the point at which yielding first occurred on either side of the bar. The curves terminate when significant reductions in strain were observed, because the basic stress-strain relationship cannot be applied after unloading occurs, since unloading and reloading occur elastically, rather than along the original stress-strain curve.

Figure 4–16 through Figure 4–18 show that out-of-plane bending moments resulting from connection eccentricities played an important role in the behavior of the anchorage bars. Figure 4–18(a) shows that yielding of the upper anchorage bars at the end columns occurred primarily as a result of bending, at axial force values well below the yield capacity of 81.3 kip (362 kN), calculated based on a nominal area of 1.27 in² (819 mm²) for a #10 bar and a yield strength of $f_y = 64$ ksi (441 MPa) listed in Table 3–1. The calculated bending moments are larger at the end columns than at the center column, probably as a result of unbalanced forces in the column plates, which permitted more extensive out-of-plane bending and eventually led to detachment of the column plates (see Figure 4–3 and Figure 4–7). Figure 4–16(a) shows that the upper anchorage bar at the left end column (Section LE) reached a peak axial force at a center column displacement of $\Delta = 3.5$ in (89 mm), close to the displacement at which detachment of the upper column plate on the left end column was noted in Figure 4–2(d). Figure 4–16(a) also shows that the upper anchorage bar at the right end column (Section RE) reached a peak axial force at a much larger center column displacement of $\Delta = 11.9$ in (302 mm), close to the displacement at which detachment of the upper column plate on the right end column was noted in Figure 4–2(h). The strain measurements thus corroborate the failure modes identified previously from the video images.

Anchorage bar fracture occurred on the left side of the center column, near Section LC, and Figure 4–14(a) shows that strain gauges S45 and S46 at Section LC both exhibited drops in strain at $\Delta = 5.7$ in (145 mm), close to the displacement at which anchorage bar fracture was noted in Figure 4–2(d). An earlier drop in strain measurement S45, at $\Delta = 2.5$ in (133 mm), prevented calculation of the axial force and bending moment at Section LC at the point of fracture using the procedure described above. However, Figure 4–16(b) shows that the lower anchorage bar on the opposite side of the center column (at Section RC) reached a peak axial force of 97.7 kip (435 kN) with a bending moment of almost zero when fracture occurred. Note that strain gauges on the anchorage bars were attached 3.5 in (89 mm) from the end of the connecting angles (see Figure 3–9). Because of steep gradients in bending moment near the welded ends of the anchorage bars, bending moments at the end of the weld, where fracture occurred, could be significantly greater than those calculated at the location of the gauges. The interaction of bending moment and axial force in the welded anchorage bars is further discussed in Section 5.4.1 in the context of computational modeling.

Figure 4–19 and Figure 4–20 present measured axial strains in the link plates (see Figure 3–11 for gauge locations), where Figure 4–19 shows strains in the link plates at the end columns and Figure 4–20 shows strains in the link plates at the center column. Strain rosettes were located at a number of locations on the link plates, and strain transformations were applied to the rosette data to obtain vertical and shear strains in addition to axial strains. However, these transformations are applicable only for elastic behavior, and yielding of the link plates occurred very early in the response, at $\Delta \approx 1$ in (25 mm) or earlier. The shear and vertical strain values in this early stage of the response were not found to provide significant insights into the behavior of the assembly, so only axial strain values are presented in this report.

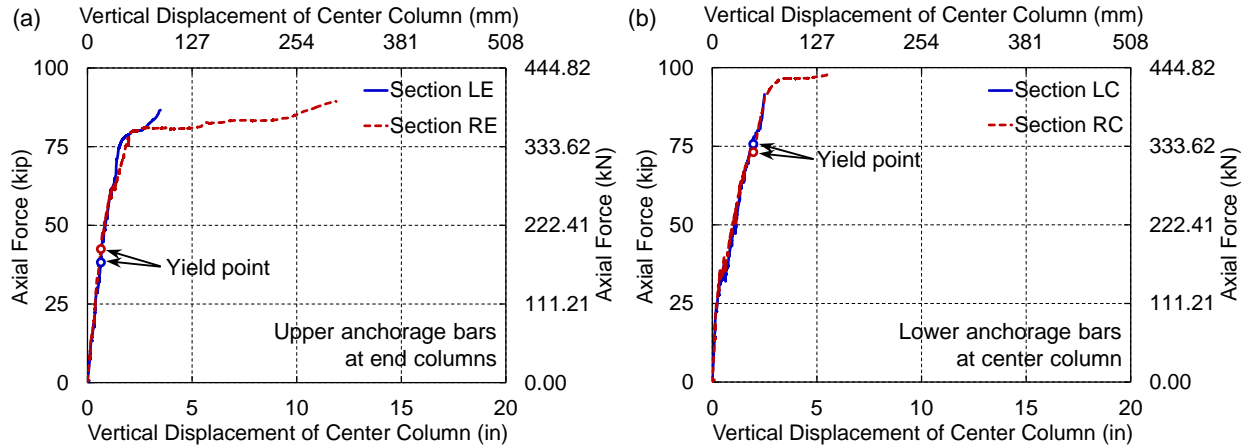


Figure 4-16. Axial force in anchorage bars (OMF specimen).

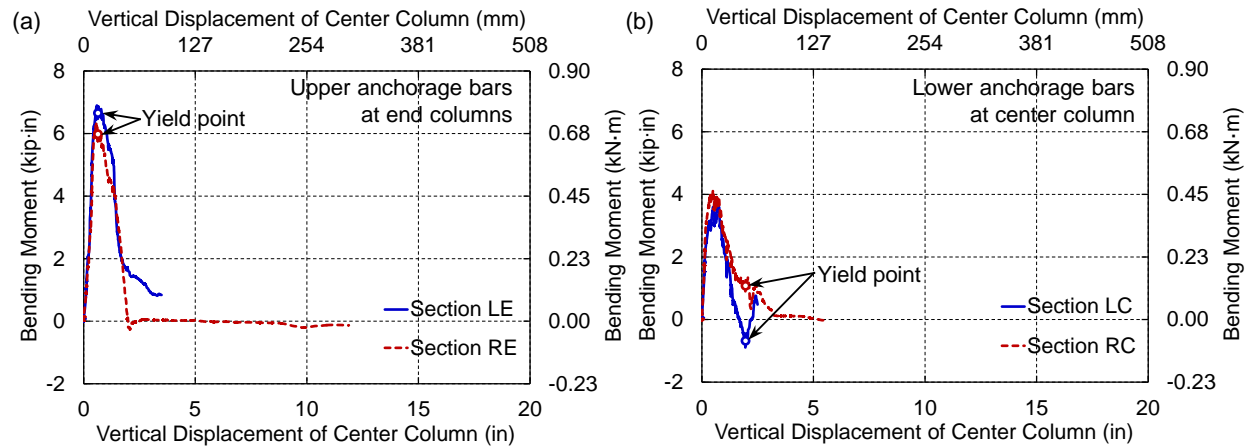


Figure 4-17. Bending moment in anchorage bars (OMF specimen).

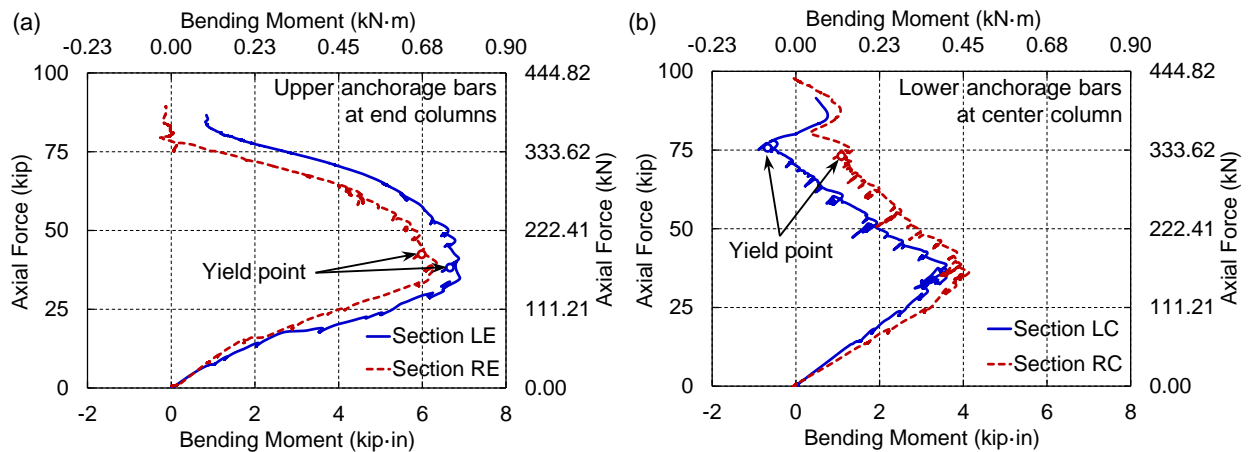


Figure 4-18. Interaction diagrams for axial force and bending moment in anchorage bars (OMF specimen).

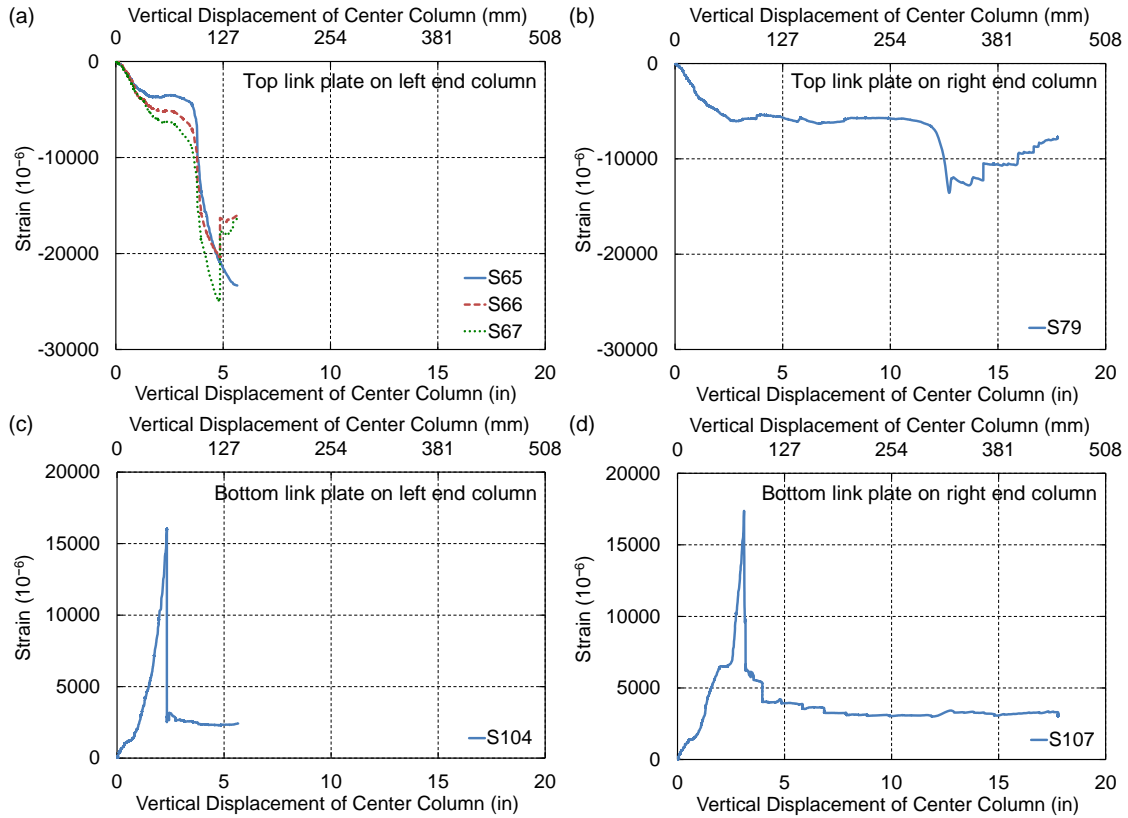


Figure 4–19. Axial strain in link plates at end columns (OMF specimen).

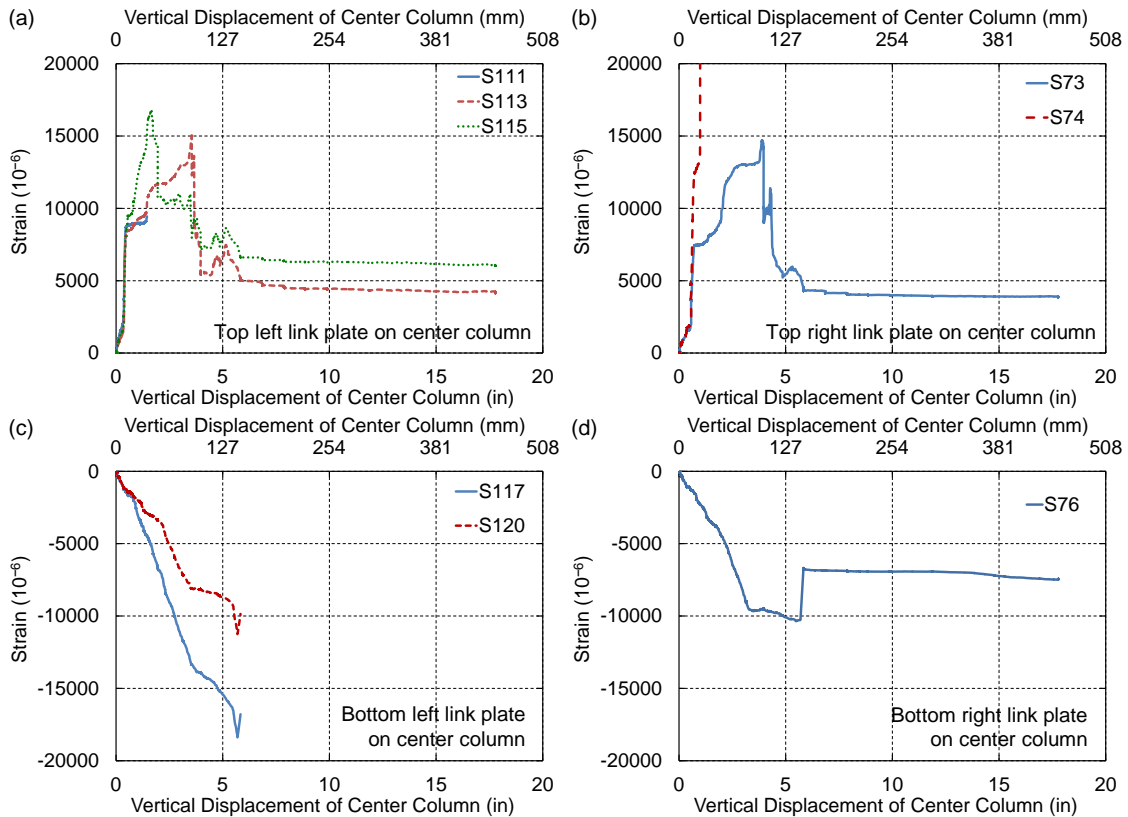


Figure 4–20. Axial strain in link plates at center column (OMF specimen).

The axial strain measurements on the link plates consistently have a sign that is opposite to what would be expected based on their location. For example, compressive strains are observed in the top link plates at the end columns [Figure 4–19(a) and (b)] and in the bottom link plates at the center column [Figure 4–20(c) and (d)], while Figure 4–13 and Figure 4–14 show tensile strains in the anchorage bars at these locations. Similarly, tensile strains are observed in the bottom link plates at the end columns [Figure 4–19(c) and (d)] and in the top link plates at the center column [Figure 4–20(a) and (b)], where compressive strains would be expected. These seemingly inconsistent measurements can be understood with reference to Figure 4–15 by noting that strains were measured on the front surface of the link plates, and that out-of-plane flexure of a link plate can result in surface strains with a sign opposite to that of the average axial strain. Tensile forces in the anchorage bars can thus result in concave bending of the link plate with compressive strains on the surface [compare Figure 4–8(a) and Figure 4–15(a)], while compressive forces in the anchorage bars can result in convex bending of the link plates with tensile strains on the surface [compare Figure 4–8(b) and Figure 4–15(b)].

The measured strains in the link plates provide further corroboration of the failure modes observed previously. Increases in strain at $\Delta = 3.7$ in (94 mm) in Figure 4–19(a) correspond to detachment of the upper column plate from the left end column [Figure 4–2(d)], and increases in strain at $\Delta = 12$ in (305 mm) in Figure 4–19(b) correspond to detachment of the upper column plate from the right end column [Figure 4–2(h)]. Sharp peaks in strain in Figure 4–19(c) and Figure 4–19(d) likely correspond to concrete cracking at the lower column plates on the end columns [Figure 4–2(b) and (c)]. Peaks in strain at $\Delta = 5.7$ in (145 mm) in Figure 4–20(c) and (d) correspond to fracture of the anchorage bars at the ultimate load of the assembly [Figure 4–2(e)].

Figure 4–21 shows the measured strains in the flexural reinforcing bars at midspan of the beams (see Figure 3–10 for gauge locations). Figure 4–22 shows average axial strains in the flexural bars, obtained from the two strain measurements on opposite sides of each bar, along with the overall average strain in the flexural bars at each cross section, obtained by averaging the measured strains in the top and bottom bars. The measured strains at midspan remain very small, with all strains remaining less than 0.02 %, well below the yield point of the bars. Small strains would be expected at midspan, because this is the inflection point in the initial flexural response, with positive bending moment at the center column, approximately equal negative bending moment at the end columns, and zero bending moment near midspan of the beams. Detachment of the upper column plate from the left end column at $\Delta = 3.7$ in (94 mm) [see Figure 4–2(d)] is evident through increased tensile strains in the bottom bars of the left beam and increased compressive strains in the top bars [Figure 4–22(a)]. This corresponds to an increase in positive bending moment, indicating that the inflection point shifted from midspan towards the left end column after detachment of the column plate, which reduced the flexural resistance of the left end connection. Fracture of the lower anchorage bars on the left side of the center column at $\Delta = 5.7$ in (145 mm) is evident through a sharp reduction in bending moment at midspan of the left beam (strains in the top and bottom bars becoming approximately equal) and a sharp increase in negative bending moment at midspan of the right beam (tension in top bars, compression in bottom bars), indicating that the inflection point in the right beam shifted toward the center column after fracture of the anchorage bars.

The overall average strain values in Figure 4–22 show tensile strains in the initial flexural response, as the beams pull the end columns inward (see Figure 4–12), with reductions in tensile strain and development of compressive strains as arching action develops and the beams push the end columns outward. Figure 4–22 shows increasing tensile strains in the final phase of the response, as the vertical load continued to

decrease (beyond point *f* in Figure 4–1). These tensile strains are counterintuitive, since compressive arching action was observed. However, note that the average strains in these flexural bars, located near the back face of the spandrel beams, do not represent the average strain over the entire cross section. Most of the axial force developed in the concrete, where strains are unknown. The measured tensile strains in these bars likely resulted from out-of-plane bending of the spandrel beams, caused by eccentricities in the transfer of forces through the beam-to-column connections.

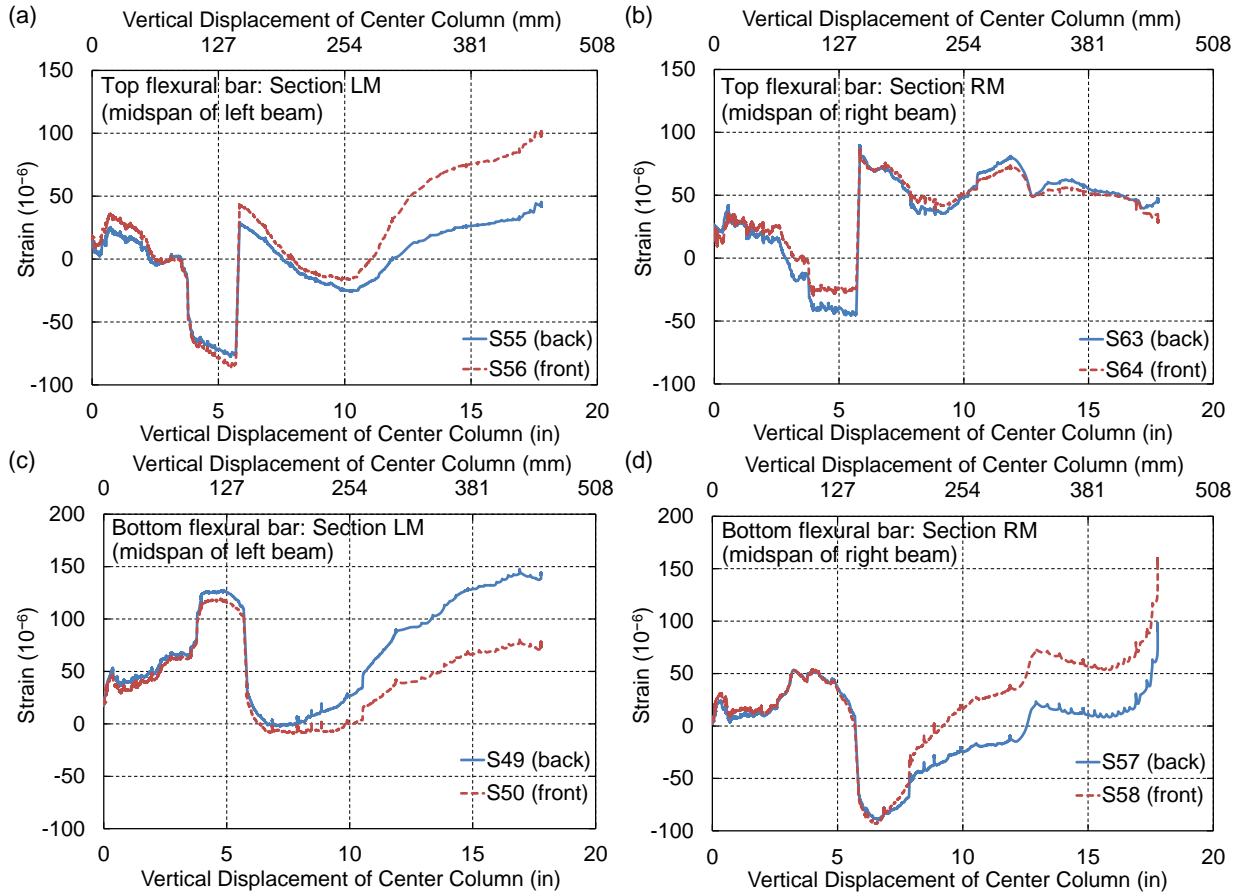


Figure 4–21. Strain in flexural reinforcing bars at midspan of beams (OMF specimen).

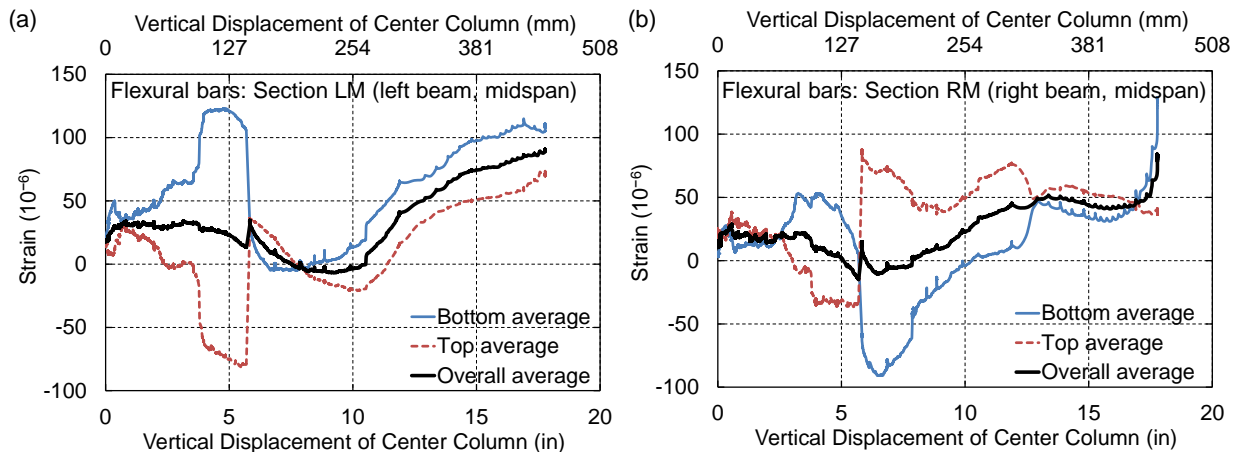


Figure 4–22. Average strain in flexural reinforcing bars at midspan of beams (OMF specimen).

Figure 4–23 shows the measured strains in the front brace beam spanning between the tops of the end columns (see Figure 3–11 for gauge locations). Figure 4–24 shows the corresponding axial force in the W16x67 brace beam, obtained by multiplying the average axial strain in the beam by the elastic modulus of 29 000 ksi (200 GPa) and the cross-sectional area of 19.7 in² (12710 mm²). Compressive forces developed in the brace beam initially, as the end columns moved inward at beam mid-height (Figure 4–12) and as negative moments in the beams tended to rotate the tops of the end columns inward. A drop in the compressive force at $\Delta = 3.7$ in (94 mm) corresponded to detachment of the upper column plate from the left end column [Figure 4–2(d)], and a second drop at $\Delta = 5.7$ in (145 mm) corresponded to anchorage bar fracture. Tensile forces subsequently developed in the brace as the tops of the end columns were pushed outward by arching action.

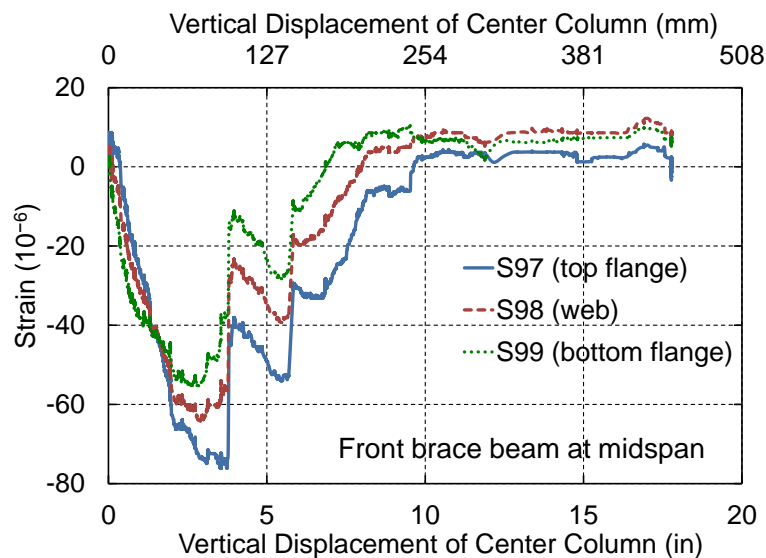


Figure 4–23. Axial strain at midspan of front brace beam (OMF specimen).

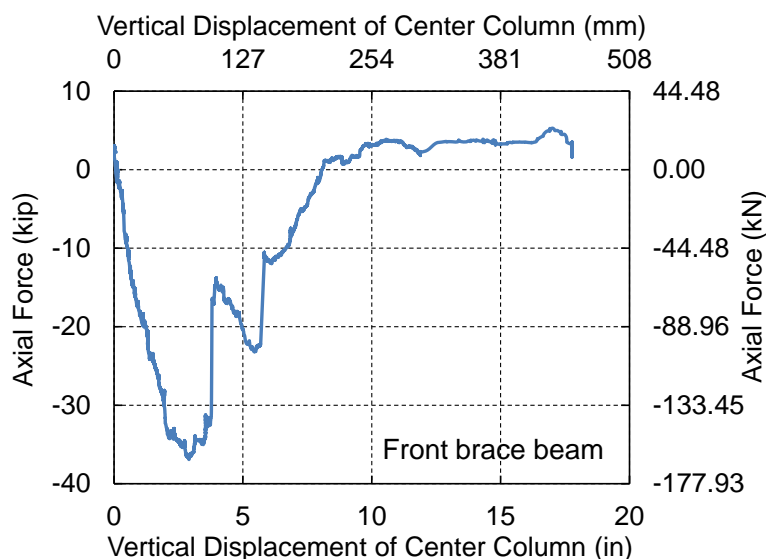


Figure 4–24. Axial force in front brace beam (OMF specimen).

4.2 SMF SPECIMEN

4.2.1 Observed Behavior and Failure Modes

Figure 4–25 shows a plot of the applied vertical load versus the vertical displacement of the center column for the SMF specimen. The vertical displacement of the center column, Δ , was obtained as an average of the displacements measured on each side of the center column (D85 and D86 in Figure 3–12). Displacement measurements are further discussed subsequently in Section 4.2.2. The labeled points in Figure 4–25 correspond to images in Figure 4–26 that show the progression of damage with increasing Δ . The images in Figure 4–26 were obtained from the three video cameras that recorded the test. The value of Δ corresponding to each row of images was estimated by tracking and scaling of vertical displacements in the images, and the uncertainty in these displacement estimates is approximately 0.2 in (5.1 mm).

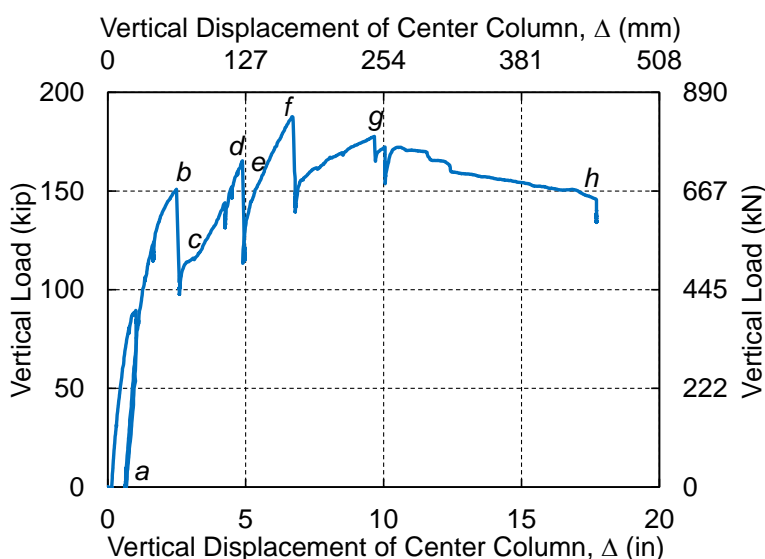


Figure 4–25. Applied vertical load vs. vertical displacement of center column for SMF specimen (labeled points correspond to images in Figure 4–26).

The specimen was initially loaded to 89 kip (391 kN) and then unloaded, to confirm that the instrumentation, data acquisition, and loading systems were working properly. During the initial phase of loading, some limited damage occurred, which included concrete cracking on the right beam near the link plates (see Figure 4–26(a)). After unloading, the center column had a residual vertical displacement of $\Delta = 0.65$ in (17 mm), corresponding to point *a* in Figure 4–25. From this point, the specimen was loaded under monotonically increasing displacement for the remainder of the test.

After reaching an initial peak load at point *b* in Figure 4–25, at a vertical displacement of $\Delta = 2.49$ in (63.3 mm), a significant drop in the vertical load occurred, from 151 kip to 98 kip (672 kN to 435 kN). This drop in load was associated with fracture of a No. 11 anchorage bar welded to the bottom connecting angle on the left side of the center column (see connection detail in Figure 2–4). Fracture of the anchorage bar was evidenced by a widened gap between the left beam and the center column, as indicated in Figure 4–26(b). Strain data from the link plates, discussed later in Section 4.2.3, indicate that the bottom anchorage bar fractured first and that the upper two anchorage bars fractured subsequently. The anchorage bars fractured at the end of the flare-bevel-groove weld on the connecting angle, as is evident

in Figure 4–27, which shows the connecting angle and welded anchorage bars recovered from the specimen after the test.

After the drop in load at point *b* in Figure 4–25, the load increased beyond the initial peak load, reaching a peak of 165 kip (735 kN) at point *d* before dropping sharply again at a displacement of $\Delta = 4.88$ in (124 mm). Between points *c* and *d*, the specimen developed additional capacity through arching action, with the bottom corner of each beam bearing against the end columns and the top corner of each beam bearing against the center column. Such bearing was evidenced by a reduced gap between the beams and columns, as indicated for the end columns in Figure 4–26(c) and for the center column in Figure 4–26(c). The drop in load at point *d* was associated with fracture of the two remaining No. 11 anchorage bars welded to the bottom connecting angle on the left side of the center column. Fracture of these anchorage bars was evidenced by further increases in the gap between the left beam and the center column, as well as extensive spalling of concrete near the anchorage bars, as indicated in Figure 4–26(d).

After the drop in load at point *d* in Figure 4–25, the load increased again up to point *f*, reaching an ultimate peak of 188 kip (836 kN) at a displacement of $\Delta = 6.69$ in (170 mm). Between points *e* and *f*, the specimen continued to develop additional capacity through arching action, with the bottom corners of the beams pressing outward against the end columns. The sharp drop in load at point *f* was associated with bond failure of the upper anchorage bars at the right end column, resulting from the formation of splitting cracks and spalling of the concrete covering the upper anchorage bars near the right end column. Initial surface cracking at this location is indicated in Figure 4–26(d), and the progression of splitting failure and spalling is more evident in Figure 4–26(e). Finally, at point *f*, extensive spalling had occurred, and a substantial gap that had opened between the right beam and the right end column provided evidence of bond failure, as indicated in Figure 4–26(f). Close-up photographs in Figure 4–28 illustrate the progression of spitting failure and concrete spalling that resulted in bond failure at this location.

It is noted that the bond failure of the anchorage bars (Figure 4–28) may have been influenced by the inverted installation of the SMF spandrel beams (see Section 3.1). If the longer anchorage bars had been at the top of the beams, as designed, bond failure may have been somewhat delayed, or anchorage bar fracture may have occurred instead. However, such differences would not be expected to significantly change the overall response of the specimen. Computational modeling (discussed in Section 5.1) showed that the inverted beams had only a small influence on the computed response of the SMF specimen.

As indicated in Figure 4–26(f), shear deformation of the right end column also commenced with the drop in load at point *f*, accompanied by diagonal cracking and spalling of concrete below the beam level. Shear deformation of the right end column continued throughout the remainder of the test, and Figure 4–29 shows the final damage to the right end column viewed from several angles.

After the drop in load at point *f*, the load continued to increase, but with a reduced stiffness, reaching 95 % of the ultimate load at point *g*. A slight drop in load at point *g* was associated with diagonal cracking of the left end column below the beam level. Shear deformation of the left end column commenced at point *g*, as indicated in Figure 4–26(g), and continued throughout the remainder of the test. Figure 4–30 shows the final state of damage of the left end column viewed from several angles. By the end of the test, both end columns had displaced noticeably outward below the beam level, as a result of arching action, while the tops of both end columns, which were linked by brace beams (see Figure 3–4), had displaced noticeably to the right. The left end column thus displaced leftward near its base but rightward at its top, as can be seen in Figure 4–26(h), resulting in extensive tensile cracking on its left

side, which is evident in Figure 4–30. From point *g* in Figure 4–25, the load gradually decreased, falling to 78 % of the ultimate load at point *h*. Finally, as the load continued to decrease and large chunks of concrete spalled from the specimen, the test was terminated at a center column displacement of $\Delta = 17.8$ in (452 mm).

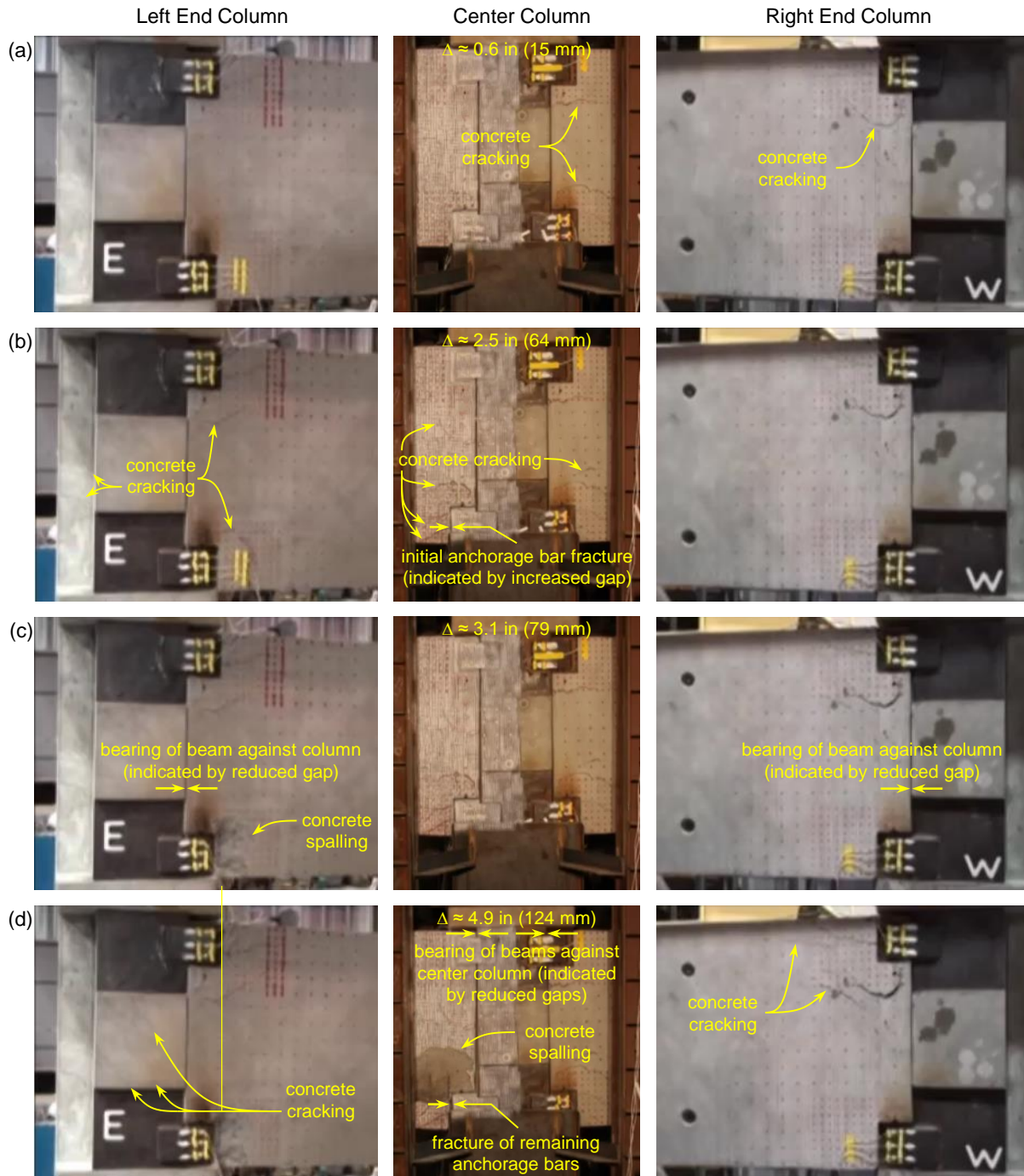


Figure 4–26. Progression of damage for SMF specimen (images correspond to labeled points in Figure 4–25).

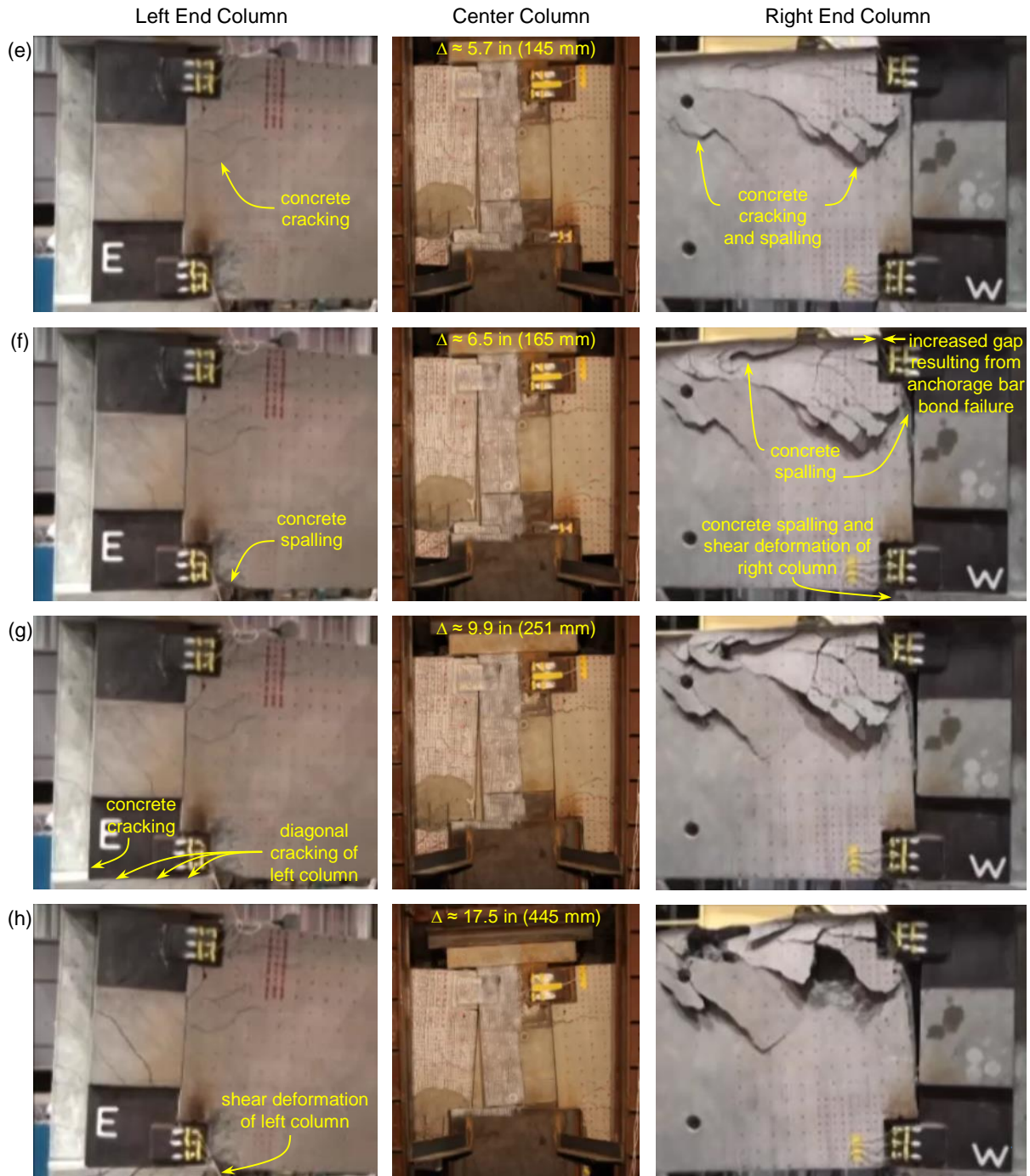


Figure 4–26 (continued). Progression of damage for SMF specimen (images correspond to labeled points in Figure 4–25).



Figure 4–27. Fractured anchorage bars from lower left connection to center column (SMF specimen).



Figure 4–28. Progression of splitting failure and concrete spalling at upper anchorage bars at right end column (SMF specimen).



Figure 4–29. Final damage to right end column viewed from several angles (SMF specimen).



Figure 4–30. Final damage to left end column viewed from several angles (SMF specimen).

4.2.2 Displacement and Rotation Measurements

Figure 4–31 shows the vertical load plotted against the vertical displacements at (a) the center column, (b) $\frac{3}{4}$ span of the beams, (c) midspan of the beams, and (d) $\frac{1}{4}$ span of the beams. Figure 4–32 shows the corresponding displacement profile of the beams at selected values of the center column displacement Δ , where Δ is the average of the two displacement measurements on each side of the center column (D85 and D86). Figure 4–32 was obtained by plotting displacements from Figure 4–31 at the transducer locations shown in Figure 3–12. Figure 4–31 and Figure 4–32 show good agreement between the measurements of symmetrically placed displacement transducers up to the initial peak load at $\Delta = 2.49$ in (63.3 mm), indicating that symmetry was largely maintained to this point. Some asymmetry of the displacement profile is evident after the initial peak load, with larger displacements on the left side of the center column than on the right side. This asymmetry is a result of the anchorage bar fractures on the lower left side of the center column, which permitted in-plane rotations of the center column, as is evident in Figure 4–26. Figure 4–32 shows that at each level of loading, the deflected profile of each beam was approximately linear, indicating that most of the deformations were localized at the beam-to-column connections, with the beams primarily rotating as rigid bodies.

Figure 4–33 shows the measured rotation at both ends of the right beam (R93 and R94, see Figure 3–12) plotted against the vertical displacement of the center column. Rotation measurements from the left beam (R91 and R92) are not presented because these inclinometers appeared to have malfunctioned. Plotted with the measured rotations is the beam chord rotation, calculated as $\theta = \tan^{-1}(\Delta/L)$, where $L = 300$ in (7620 mm) is the centerline-to-centerline beam span. The measured rotation of the right beam near the center column (R93) remained quite close to the calculated chord rotation, being less than the chord rotation by about 0.35° (0.0061 rad) for most of the test. A sudden increase in rotation measurement R94 occurred at $\Delta = 6.8$ in (172 mm), which was likely associated with spalling of concrete at the upper anchorage bars near the right end column, where the inclinometer was mounted [see Figure 4–26(f)]. Later in the test, rotation measurement R94 decreased and converged fairly closely to the calculated beam chord rotation.

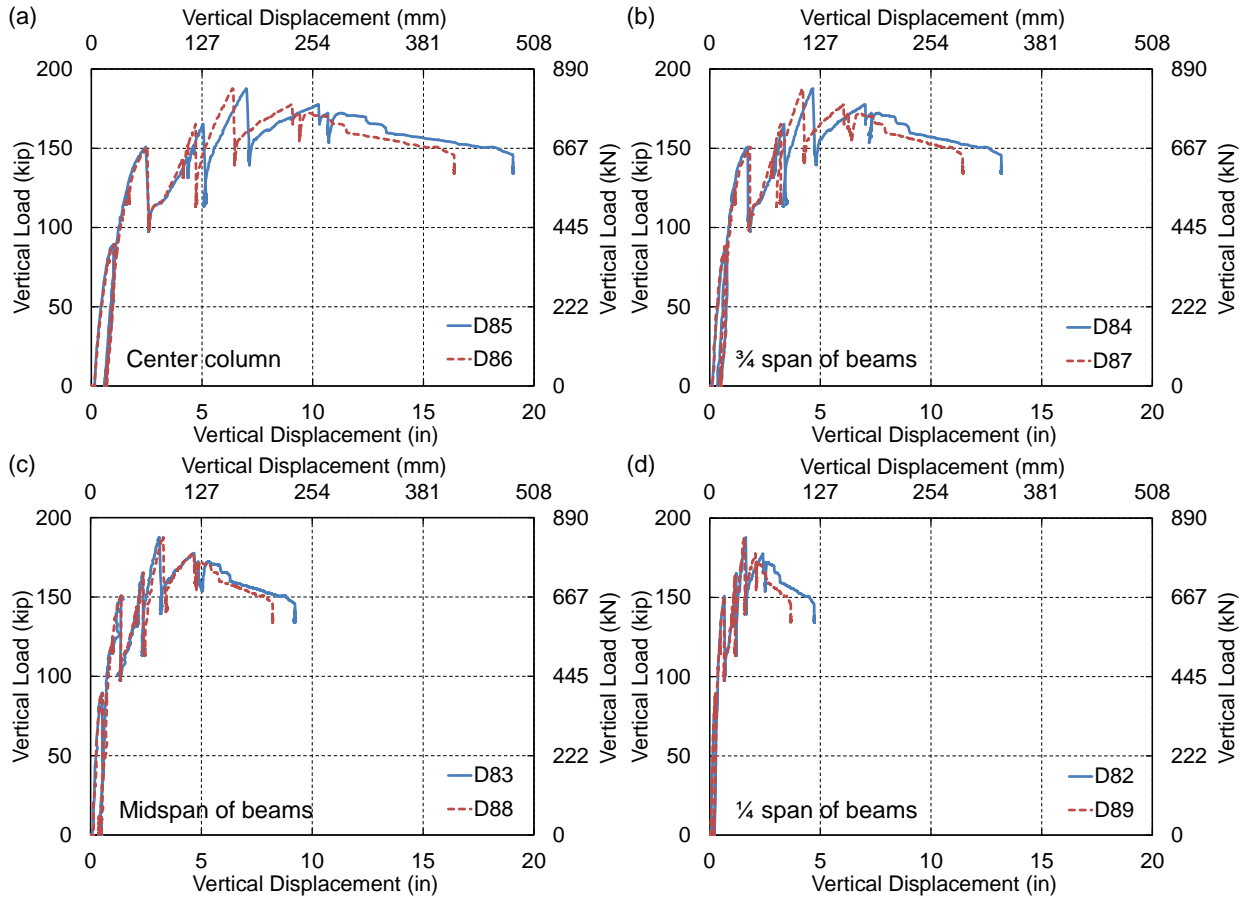


Figure 4-31. Applied vertical load vs. vertical displacements at (a) center column, (b) 3/4 span of beams, (c) midspan of beams, and (d) 1/4 span of beams (SMF specimen).

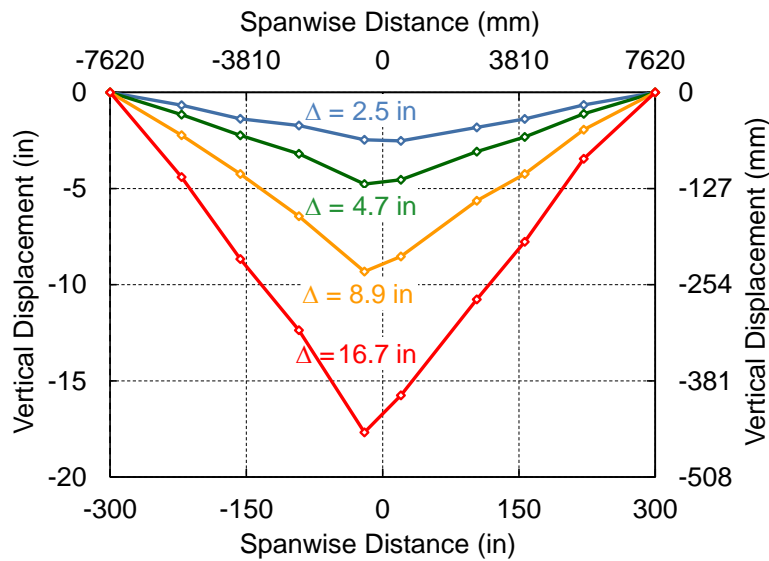


Figure 4-32. Vertical displacement profile of beams corresponding to indicated vertical loads (SMF specimen; displacements magnified).

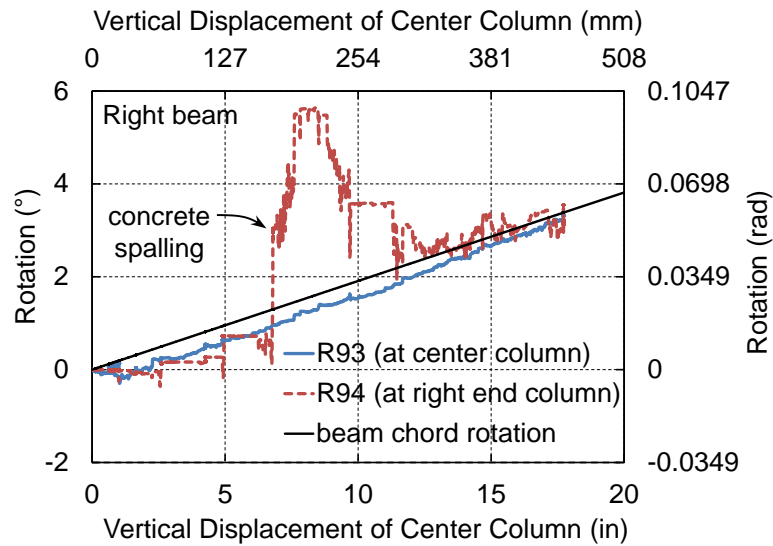


Figure 4–33. Beam end rotations (SMF specimen).

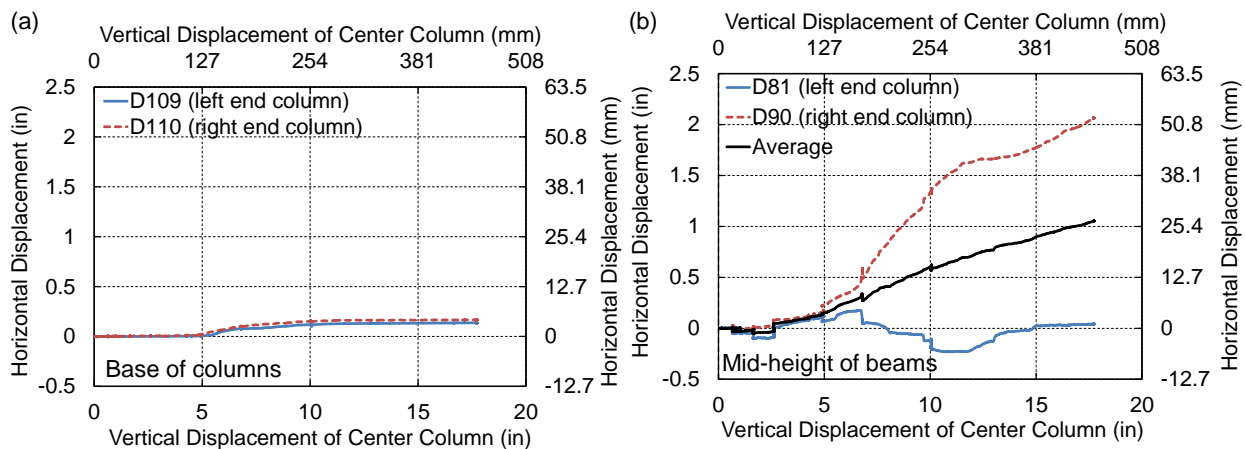


Figure 4–34. Horizontal displacement of end columns (SMF specimen).

Figure 4–34 shows the horizontal displacement of the end columns at (a) the column bases and (b) beam mid-height, with positive values signifying outward displacement, plotted against the vertical displacement of the center column. The footings at the bases of the end columns were clamped to the strong floor using post-tensioning bars to prevent horizontal displacement (see Figure 3–4). Figure 4–34(a) shows that displacements at the column bases remained quite small, with an average outward displacement of 0.15 in (3.8 mm) at the end of the test. Plotted along with the measured displacements at beam mid-height in Figure 4–34(b) is the average of the two measurements, which cancels out rigid body motions. Initially, both end columns displaced slightly inward at beam mid-height, reaching an average inward displacement of 0.042 in (1.1 mm) prior to the onset of arching action. After fracture of the anchorage bars (point *b* in Figure 4–25), at a center column displacement of $\Delta = 2.6$ in (66 mm), both end columns began to move outward as a result of arching action in the beams. At $\Delta = 6.7$ in (170 mm), after bond failure of the upper anchorage bars at the right end column, and after shear deformation of the right end column commenced (point *f* in Figure 4–25), the motion of the left column changed direction, and both columns moved to the right at beam mid-height. The left column reached a peak inward (rightward)

displacement of 0.23 in (5.8 mm) at $\Delta \approx 11.7$ in (297 mm) before changing direction again and beginning to move outward as a result of cracking and shear deformation of the left column. Although the displacement of the left column changed directions due to rigid-body motions, the average displacement at beam mid-height shows a monotonically increasing outward displacement after the onset of arching action, with an average outward displacement of 1.05 in (26.7 mm) at the end of the test.

4.2.3 Strain Measurements

Figure 4–35 and Figure 4–36 present measured axial strains in the link plates of the SMF specimen (see Figure 3–15 for gauge locations). For the OMF specimen, strain measurements on the link plates, presented previously, had the opposite sign that would be expected based on their location, as a result of out-of-plane bending of the link plates (see Figure 4–15). However, out-of-plane bending of the link plates was less extensive for the SMF specimen than for the OMF specimen (compare Figure 4–28 and Figure 4–8, for example). Consequently, the strain measurements on the link plates of the SMF specimen generally had the expected sign, with tensile strains in the top link plates at the end columns [Figure 4–35(a) and (b)] and in the bottom link plates at the center column [Figure 4–36(c) and (d)], and compressive strains in the bottom link plates at the end columns [Figure 4–35(a) and (b)] and in the top link plates at the center column [Figure 4–36(a) and (b)].

Figure 4–37 shows typical deformation and strain profiles for the anchorage bars and link plates of the SMF specimen, which exhibit strains of the same sign in the anchorage bar and on the front surface of the link plate (contrast with Figure 4–15 for the OMF specimen). The exception to this pattern is for the lowest strain gauges on the bottom link plates on the center column [S72 in Figure 4–36(c) and S77 in Figure 4–36(c)], where compressive strains developed on the surface of the link plates, as illustrated in Figure 4–15(a), indicating more extensive out-of-plane bending near the bottom edge of the bottom link plates. Interestingly, this is the location where the initial anchorage bar fracture occurred. In the top link plates, out-of-plane bending was greater near the top edge than the bottom edge, as evidenced by the lower magnitudes of strain for the upper gauges in Figure 4–35(a) and (b) and in Figure 4–36(a) and (b). A fairly consistent pattern is thus observed, in which the extreme edges of the link plates (top edges of top link plates and bottom edges of bottom link plates) exhibit more extensive out-of-plane bending, perhaps induced by larger tensile forces in the uppermost and lowermost anchorage bars.

The measured strains in the link plates provide further corroboration of the failure modes discussed previously. Figure 4–36(c) shows a sudden change in sign for strain gauge S72 at $\Delta = 2.6$ in (66 mm), which corresponds to fracture of the lowest anchorage bar on the left side of the center column [Figure 4–26(b)]. Simultaneous increases in tensile strain for the upper two strain gauges on the same link plate [S70 and S71 in Figure 4–36(c)] indicate that the two remaining anchorage bars at that location remained intact and developed additional load after fracture of the lowest bar. Subsequent reductions in strain for strain gauges S70 and S71 at $\Delta = 4.9$ in (124 mm) correspond to fracture of the two remaining anchorage bars [Figure 4–26(d)]. Figure 4–35(b) shows sharp increases in strain for gauges S78–S80 on the upper link plate on the right end column at $\Delta = 6.7$ in (170 mm), followed by gradual reductions in strain, corresponding to bond failure of the upper anchorage bars at this location [Figure 4–26(f)].

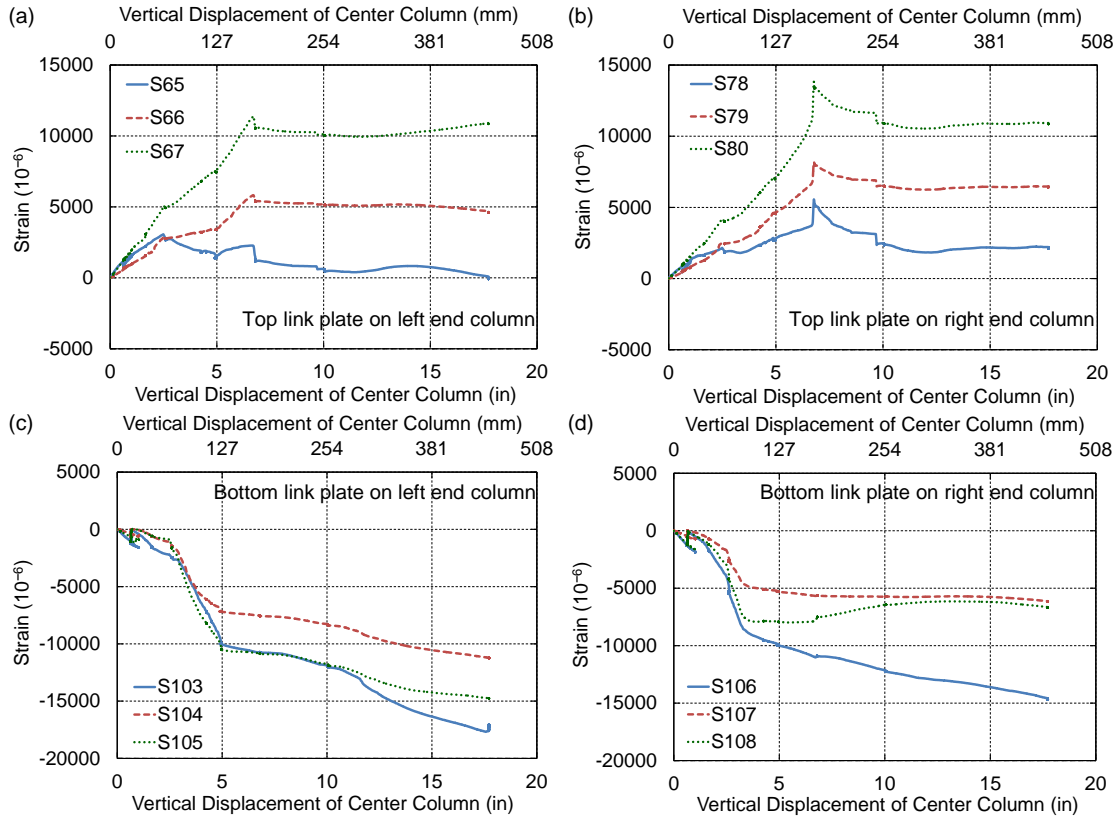


Figure 4-35. Axial strain in link plates at end columns (SMF specimen).

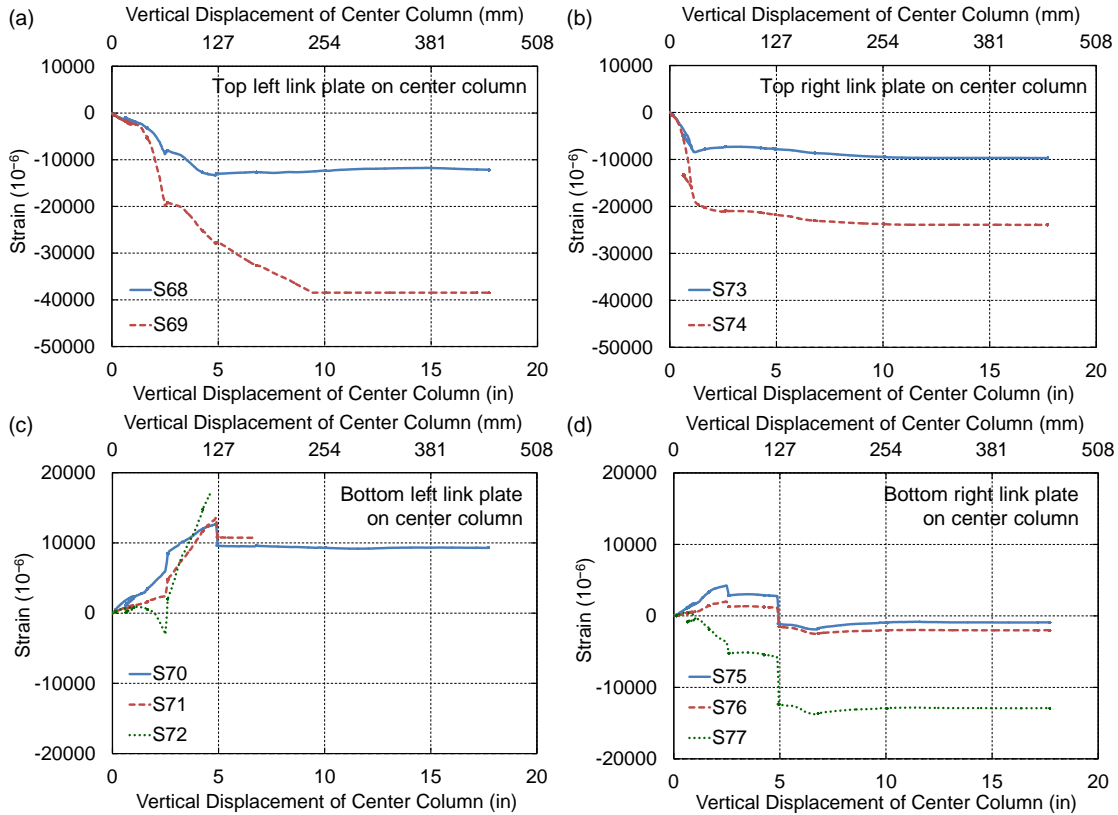


Figure 4-36. Axial strain in link plates at center column (SMF specimen).

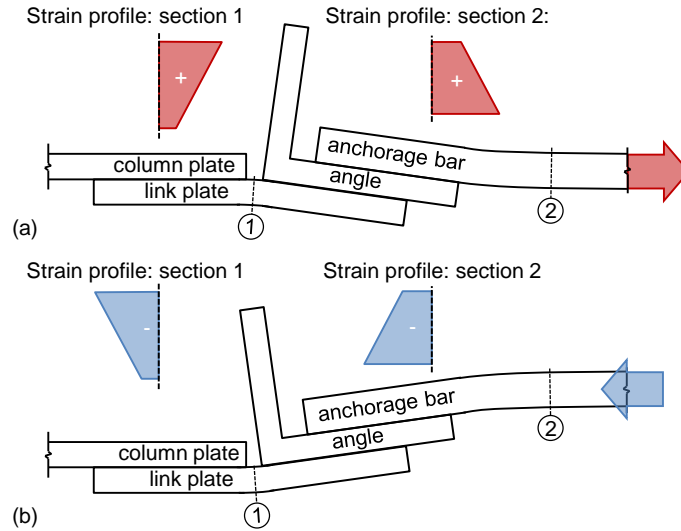


Figure 4–37. Deformation and strain profiles in anchorage bar and link plate of SMF specimen: (a) tension in anchorage bar; (b) compression in anchorage bar.

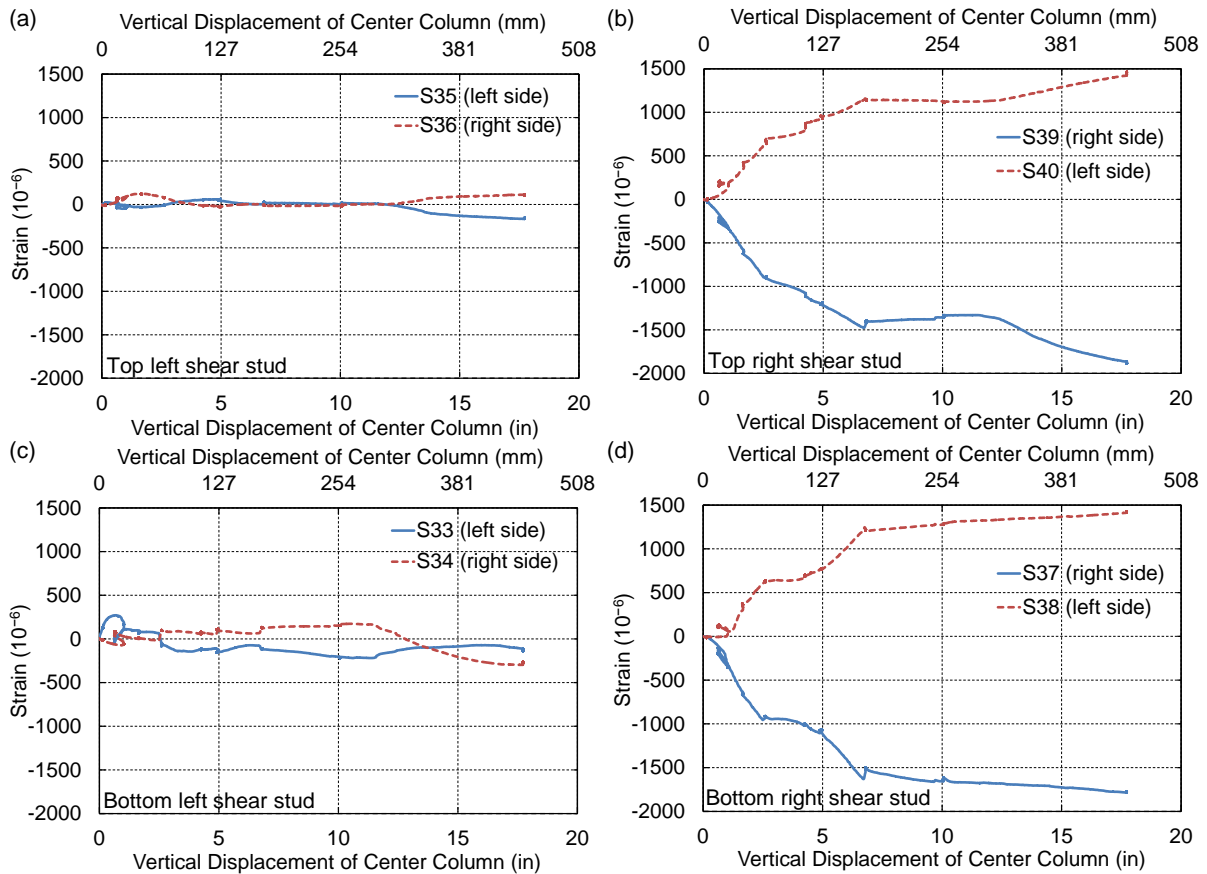


Figure 4–38. Strain in shear studs on upper column plate on left end column (SMF specimen).

Figure 4–38 shows measured strains in shear studs on the upper column plate on the left end column (see Figure 3–14 for gauge locations). Bending of the shear studs is indicated by nearly equal and opposite strains measured on opposite sides of each shear stud. As would be expected, larger strains were observed in the studs on the right side of the plate [Figure 4–38(b) and (d)], where loads were transferred to the

column plate by the link plate, than in the studs on the left side [Figure 4–38(a) and (c)], which are near the free edge of the plate. The measured strains in Figure 4–38 remain less than 0.2 %, which is the approximate yield point of the shear studs. Although detachment of column plates was observed for the OMF specimen (Figure 4–3 and Figure 4–7), no shear stud failures were observed for the SMF specimen.

Figure 4–39 shows the measured strains in the flexural reinforcing bars at midspan of the beams (see Figure 3–13 for gauge locations). Figure 4–40 shows average axial strains in the flexural bars, obtained from the two strain measurements on opposite sides of each bar, along with the overall average strain in the flexural bars at each cross section, obtained by averaging the measured strains in the top and bottom bars. The measured strains at midspan are very small, with all strains remaining less than 0.06 %, well below the yield point of the bars. Small strains would be expected at midspan, because this is the inflection point in the initial flexural response, with positive bending moment at the center column, approximately equal negative bending moment at the end columns, and zero bending moment near midspan of the beams. Fracture of the bottom anchorage bar on the left side of the center column at $\Delta = 2.5$ in (64 mm) [Figure 4–26(b)] is evident through increased tensile strains in the top bars of the both beams and increased compressive strains in the bottom bars (Figure 4–40). This corresponds to an increase in negative bending moment, indicating that the inflection points in both beams shifted from midspan towards the center column after fracture of the anchorage bar, which reduced the flexural resistance at the center column. Fracture of the two remaining anchorage bars on the left side of the center column at $\Delta = 4.9$ in (124 mm) [Figure 4–26(d)] is evident through further increases in negative bending moment at midspan of both beams, with these increases being more pronounced in the right beam, where the connection to the center column remained intact. Bond failure of the upper anchorage bars at the right end column at $\Delta = 6.7$ in (170 mm) [Figure 4–26(f)] was evident through sharp reductions in the measured strains, with these reductions being more pronounced in the right beam, where the bond failure occurred.

The plot of overall average strain at midspan of the right beam [Figure 4–40(b)] shows tensile strains in the initial flexural response, as the beams pull the end columns inward (see Figure 4–34), with reductions in tensile strain and development of compressive strains as arching action develops and the beams push the end columns outward. Compressive strains associated with arching action are not evident in Figure 4–40(a), and both Figure 4–40(a) and (b) show tensile strains developing in the final phase of the response. These tensile strains are counterintuitive, since compressive arching action was observed. However, note that the average strains in these flexural bars, located near the back face of the spandrel beams, do not represent the average strain over the entire cross section. Most of the axial force developed in the concrete, where strains are unknown. The measured tensile strains in these bars likely resulted from out-of-plane bending of the spandrel beams, caused by eccentricities in the transfer of forces through the beam-to-column connections.

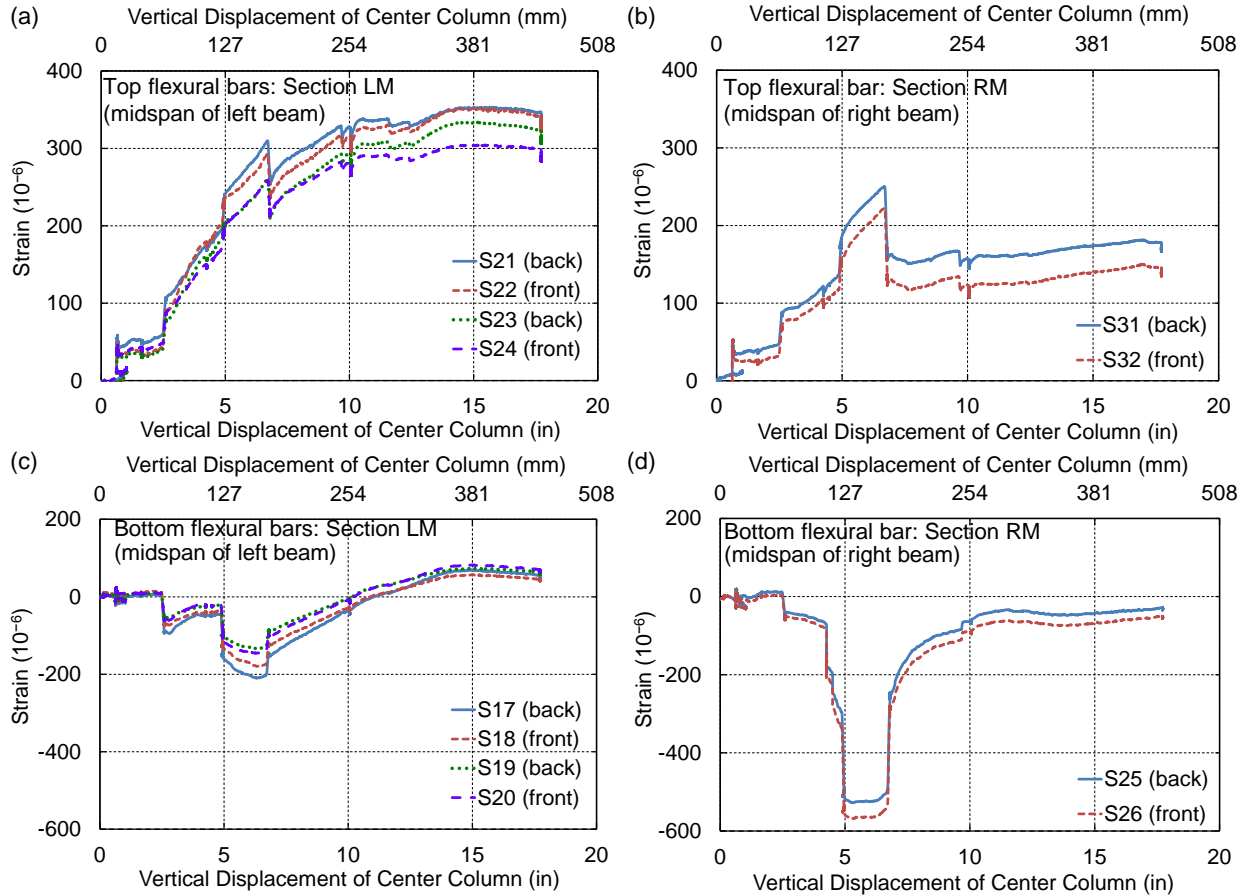


Figure 4-39. Strain in flexural reinforcing bars at midspan of beams (SMF specimen).

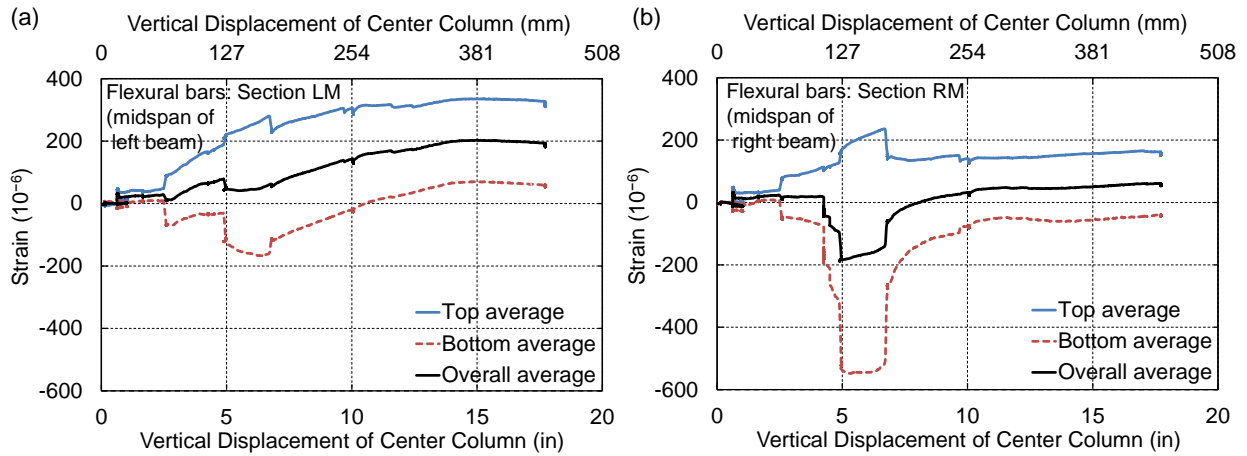


Figure 4-40. Average strain in flexural reinforcing bars at midspan of beams (SMF specimen).

Figure 4-41 shows the measured strains in the W16x67 brace beams spanning between the tops of the end columns (see Figure 3-15 for gauge locations). Figure 4-42 shows the corresponding axial forces in the brace beams, obtained by multiplying the average axial strain in each beam by the elastic modulus of 29 000 ksi (200 GPa) and the cross-sectional area of 19.7 in² (12710 mm²). The total brace force, obtained by summing the axial forces in the two brace beams, is also plotted in Figure 4-42. Compressive forces developed in the brace beams initially, as the end columns moved slightly inward at beam mid-height

(Figure 4–34) and as negative moments in the beams tended to rotate the tops of the end columns inward. Sudden reductions in the compressive force at $\Delta = 2.5$ in (64 mm) and at $\Delta = 4.9$ in (124 mm) corresponded to fracture of the lower anchorage bars on the left side of the center column [Figure 4–26(b) and (d)]. A steep reversal in the sign of the brace beam forces, from compressive to tensile, occurred at $\Delta = 6.7$ in (171 mm), which corresponded to bond failure of the upper anchorage bars at the right end column and the onset of shear deformations of the right end column [Figure 4–26(f)]. The top of the right end column was subsequently forced outward (rightward) by arching action, pulling the top of the left end column rightward as well, and thus developing tensile forces in the brace beams. Differences in strain through the depth of the brace beams were indicative of flexure, which was induced by in-plane rotations at the tops of the end columns.

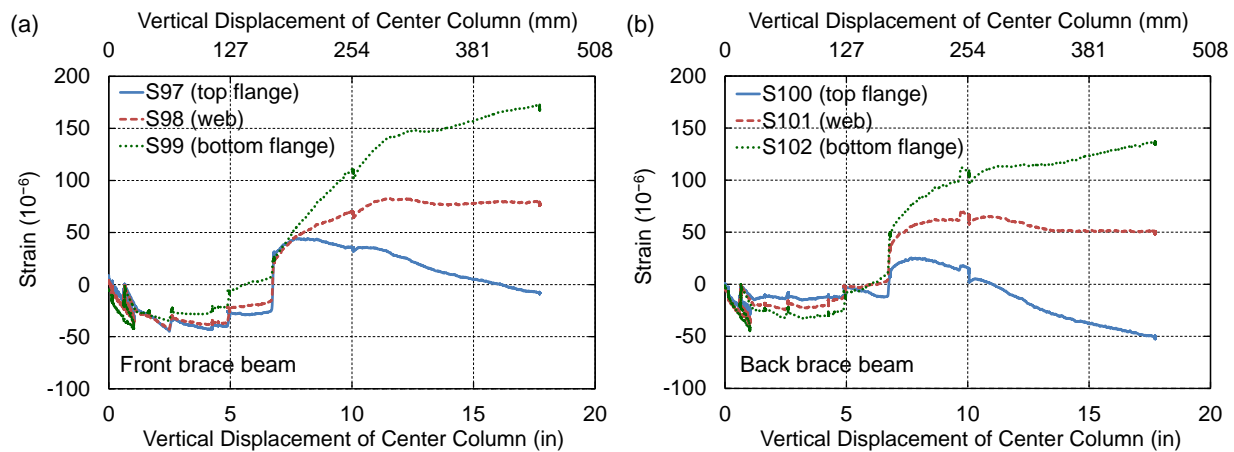


Figure 4–41. Strain in brace beams at midspan (SMF specimen).

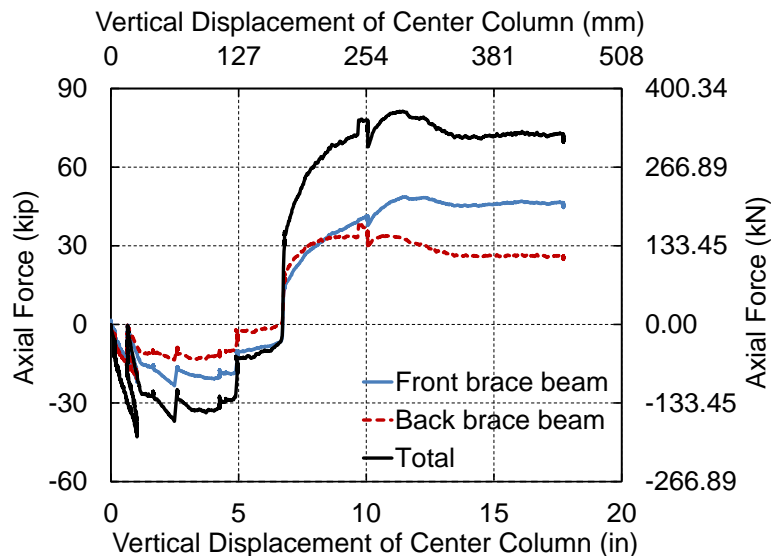


Figure 4–42. Axial force in brace beams (SMF specimen).

Differences between the axial forces in the two brace beams resulted from torsion in the end columns. Because the precast spandrel beams were aligned with the front faces of the columns, rather than their centerlines (see top view in Figure 3–4), forces in the link plates produced torsion in the end columns. This torsion was resisted by contact with the cross beams used to brace the end column tops at their inside

and outside faces, resulting in differential forces in the front and back brace beams. Initially, tensile forces in the upper link plates on the end columns tended to pull the front faces of the end columns inward, and this torsional rotation was resisted by greater compression in the front brace beam. Subsequently, compressive forces associated with arching action tended to push the front faces of the end columns outward, and this torsional rotation was resisted by greater tension in the front brace beam.

4.3 SUMMARY AND DISCUSSION

This chapter presented experimental results for the OMF and SMF specimens, which were subjected to vertical loading of the unsupported center column to simulate a column removal scenario. Experimental measurements were presented, which included the applied vertical load, vertical displacements of the center column and beams, horizontal displacements of the end columns, rotations at the beam ends, and strains in reinforcing bars, anchorage bars, link plates, and other steel components. Photographs and video images were also presented to illustrate the behavior, damage progression, and failure modes of the specimens.

The responses of the two specimens consisted of three primary stages, which are illustrated in Figure 4–43. In the first stage, loads were resisted through flexural action. As illustrated in Figure 4–43(a), tensile forces in the bottom link plates at the center column were balanced by compressive forces in the top link plates, and tensile forces in the top link plates at the end columns were balanced by compressive forces in the bottom link plates. Eccentricities in the transfer of forces through the link plate connections, as illustrated in Figure 4–44(a), resulted in out-of-plane bending of the link plates and anchorage bars, as illustrated in Figure 4–44(a). This out-of-plane bending was evident from strain gauge measurements and from photographs of the deformed plates.

In the second stage, loads were resisted through a combination of flexural action and arching action. This stage began when deflections and rotations of the beams caused the initial gaps between the beams and columns to close, as illustrated in Figure 4–43(b). The top ends of each beam began to bear against the center column, while the bottom ends of each beam began to bear against the end columns, enabling the development of arching action. Arching action became evident at a center column displacement of about 3.9 in (99 mm) for the OMF specimen and about 3.1 in (79 mm) for the SMF specimen. Increased vertical loads were developed in this stage, along with increased compressive forces in the beams, as the beams began to push the end columns outward.

In the third stage, the specimens continued to carry loads through arching action, but at a reduced capacity because of multiple failures that reduced the flexural resistance of the beam-to-column connections. Specifically, these failures degraded the capacity for transfer of tensile forces through the link plate connections, both at the upper link plates on the end columns and at the lower link plates on the center column, as illustrated in Figure 4–43(c). After the flexural resistance was compromised by these failures in the transfer of tensile forces, diagonal cracks and shear deformations developed in the lower portions of the end columns, as continued arching action forced the end columns outward.

For the OMF specimen, the first failure in tensile force transfer was at the upper link plate assembly on the left end column (see Figure 4–3), where the column plate detached from the column at a center column displacement of about 3.7 in (94 mm) (see Figure 4–2(d)). The specimen developed additional load through arching action until a second failure in tensile force continuity occurred, which was

anchorage bar fracture at the lower link plate assembly on the left side of the center column (see Figure 4-4). This failure occurred at $\Delta = 5.7$ in (144 mm) (see Figure 4-2(e)) and was associated with the peak vertical load.

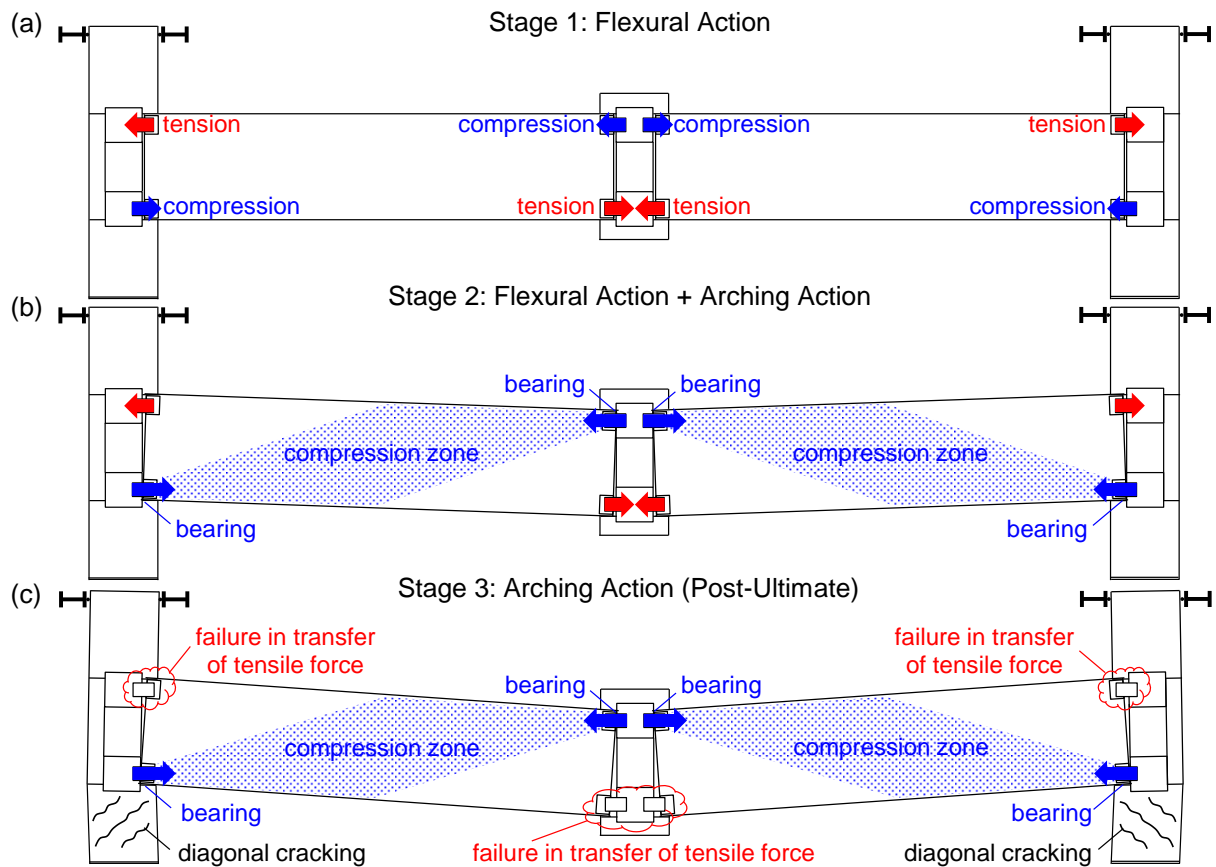


Figure 4-43. Three stages in the response of the precast concrete specimens.

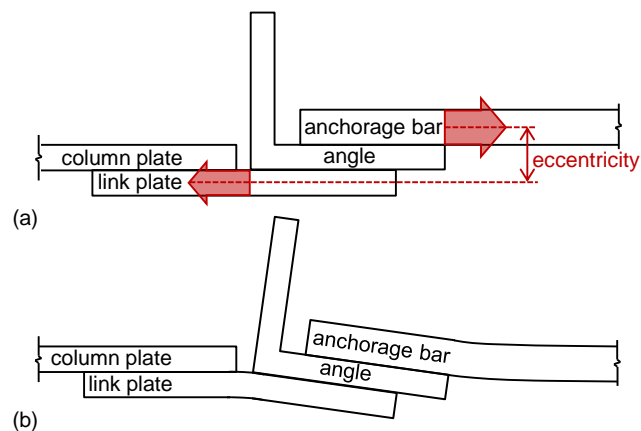


Figure 4-44. Top view of link plate connection showing (a) eccentricity in force transfer and (b) resulting out-of-plane bending.

For the SMF specimen, the first failure in tensile force transfer was at the lower link plate assembly on the left side of the center column, where the anchorage bars fractured (see Figure 4–27), first the lowest bar at $\Delta = 2.6$ in (66 mm) (see Figure 4–26(b)) and then the upper two bars at $\Delta = 4.9$ in (124 mm) (see Figure 4–26(d)). The SMF specimen also developed additional load through arching action until a second failure in tensile force transfer occurred, which was bond failure of the anchorage bars at the upper link plate assembly on the right end column, as a result of splitting cracks and spalling of the beam concrete at that location (see Figure 4–28). This failure occurred at $\Delta = 6.7$ in (170 mm) (see Figure 4–26(f)) and was associated with the peak vertical load.

The peak vertical load for the OMF specimen was 166 kip (738 kN), while the peak load for the SMF specimen was 188 kip (836 kN). Corresponding beam chord rotations at the ultimate load were calculated as $\theta_u = \tan^{-1}(\Delta_u/L)$, where Δ_u is the center column displacement at the ultimate load and $L = 25$ ft (7.6 m) is the centerline-to-centerline span length. Values of $\theta_u = 0.019$ rad and $\theta_u = 0.022$ rad were obtained for the OMF and SMF specimens, respectively. Thus, the more stringent seismic design for the SMF specimen resulted in an increase of only 13 % in the ultimate capacity under the column removal scenario, with an increase of 18 % in the corresponding beam chord rotation. While the initial anchorage bar fracture for the OMF specimen occurred at $\theta_u = 0.019$ rad, the initial anchorage bar fracture for the SMF specimen occurred at a much smaller beam chord rotation of only 0.0087 rad. Computational results presented subsequently in Section 5.6 show that for the prototype span length of $L = 30$ ft (9.1 m), the ultimate capacity of the SMF specimen was actually slightly less than that of the OMF specimen. The robustness of the OMF and SMF specimens is further discussed and compared in Chapter 6.

In full-scale testing and computational modeling of reinforced concrete moment frames under a column removal scenario, Lew et al. (2011) observed that an arching action stage was followed by a catenary action stage, in which tensile forces developed in the beams, providing additional load-carrying capacity. Tensile forces developed in the beams when the deflection of the center column was approximately equal to the depth of the beams. However, the precast concrete spandrel beams considered in this study were much deeper than the reinforced concrete beams considered by Lew et al. (2011), and failures of the precast concrete specimens occurred when the deflections of the center column remained much less than the beam depth. Consequently, catenary action did not develop for the precast concrete specimens considered in this study.

The diagonal cracking, spalling, and shear deformation of the end columns observed in these tests indicate that lateral forces due to arching action could potentially result in shear failure of columns. If arching action is to be exploited in resisting vertical loads under column removal scenarios, care must be taken to ensure that the columns adjacent to the missing column can resist the lateral loads induced by arching action. In evaluating the potential for column shear failure, gravity loads from the upper stories should be considered in combination with shear forces due to arching action. The potential for shear failure is of particular concern for columns that have spandrel beams framing into the connections from only one side, like the end columns considered in these tests. For an intermediate column in a moment frame, the spandrel beam framing into the connection from the adjacent bay would provide resistance to rotation and horizontal displacement of the column, thus reducing the flexural and shear demands on the column. Corner columns, therefore, need particular attention in evaluating the potential for shear failure due to arching action.

This page intentionally left blank.

Chapter 5

COMPUTATIONAL MODELING AND ANALYSIS

This chapter presents a computational study of the response of the OMF and SMF specimens under the column removal scenario considered experimentally. The main objectives of the computational study were to (1) develop finite element models that could adequately capture the experimentally observed behaviors and failure modes of the specimens, (2) provide additional insights into behaviors and failure modes that could not be directly observed from the experimental data, and (3) evaluate the response of specimens having the full prototype span length, which could not be accommodated within the testing facility (see Section 3.1). Another important aspect of the computational study is that multiple analyses were run for each specimen, with variations in geometric and material parameters. These analyses enabled identification of key factors that influenced the responses of the specimens and provided insights into the sensitivity of the responses to uncertainties in these factors.

To provide context for the subsequent discussion of computational modeling, Section 5.1 discusses pre-test modeling of the test specimens and illustrates the influence of key factors on the computed responses. Section 5.2 provides an overview of the finite element models that were developed for the two specimens, and Section 5.3 describes the material models used to represent the various components of the specimens. Modeling of the welded anchorage bar connections, discussed in Section 5.4, required particular care in order to capture the interaction of axial forces with bending moments resulting from connection eccentricities, as well as reductions in ductility near the welds. Section 5.5 presents analysis results from the computational models of both specimens, including comparisons with the experimental results to demonstrate that the models were able to capture the primary response characteristics and failure modes. As noted previously in Section 3.1, the span length of the test specimens was reduced in order to fit within the test facility, and Section 5.6 presents a computational investigation of the influence of span length on the responses of the specimens. Finally, Section 5.7 summarizes and discusses the results of the computational study.

5.1 PRE-TEST MODELING AND MODEL SENSITIVITIES

Initial pre-test models of each specimen were developed to aid in planning of the tests and layout of the instrumentation. These initial models overestimated the resistance of the test specimens relative to the experimental data and did not capture some of the failure modes that were observed experimentally. The main discrepancies between the pre-test models and the experimental results, along with the key factors that were identified as responsible for these differences, can be summarized as follows:

1. Fracture of the welded anchorage bars (see Figure 4–4 and Figure 4–27) occurred significantly earlier in the tests than predicted by the pre-test models. This earlier fracture was due to (a) localized bending moments near the welds and (b) reductions in the ductility of the anchorage bars in the heat-affected zones near the welds. As discussed in Section 5.4, the first factor affected both test specimens, while the second factor was significant only for the SMF specimen. Neither of these factors was adequately captured in the pre-test modeling. After the test, component testing of a welded anchorage bar was performed, and a more refined post-test

modeling approach for the welded anchorage bars was developed to capture these effects (see Section 5.4).

2. Detachment of the column plates and embedded shear studs from the end columns in the OMF specimen was not captured by the pre-test model. This detachment resulted from a complex state of loading of the shear studs, in which shear forces were coupled with tensile forces due to out-of-plane bending of the link plates. The effects of this out-of-plane bending were accounted for in the post-test models by reducing the effective shear capacity of the shear studs as described in Section 5.3.5. Such reductions were significant for the OMF specimen but not for the SMF specimen because of the lesser out-of-plane bending of the link plates (see Section 5.3.5). While other aspects of the modeling were based on constitutive relationships for the materials, this shear stud failure criterion was calibrated to capture the experimentally observed failures.
3. Development of vertical loads through arching action was less than predicted by the pre-test model for the OMF specimen. The smaller loads observed experimentally were due to larger initial gaps between the beams and columns than were assumed in the pre-test model: the larger gaps delayed the development of arching action and reduced its extent. The gap width was not specified in the design of the prototype buildings (Kim et al. 2009a,b), and a gap width of 0.50 in (13 mm) was assumed in the pre-test modeling. The post-test models used initial gap widths from the actual test specimens, which were 0.75 in (19 mm) for the OMF specimen and 0.35 in (9 mm) for the SMF specimen. Use of the actual gap widths allowed the post-test models to better capture the experimentally observed arching action.

Results are compared from three models of each specimen, as listed in Table 5–1, in order to illustrate the sensitivity of the computed responses to variations in the key factors listed above. These results highlight some of the challenges and complexities in modeling of precast concrete moment frames and provide helpful perspective on the final post-test modeling approach, which is described in the following sections.

Computed results from the models in Table 5–1 are presented in Figure 5–1 and Figure 5–2 for the OMF and SMF specimens, respectively. Models OMF-A and SMF-A were the final post-test models of the two specimens, which are compared with experimental measurements in Section 5.5, while the other models in Table 5–1 considered variations in the key factors listed above. The three models of each specimen were identical apart from variations in the factors listed in Table 5–1.

Table 5–1. Finite element models used to illustrate the influence of key factors on the computed responses.

Model	Initial Gap	Shear Stud Strength	Anchorage Bar Model
OMF-A*	0.75 in (19 mm)	reduced	ductile
OMF-B	0.50 in (13 mm)	reduced	ductile
OMF-C	0.75 in (19 mm)	nominal	ductile
SMF-A*	0.35 in (9 mm)	nominal	reduced ductility
SMF-B	0.35 in (9 mm)	nominal	ductile
SMF-C	0.50 in (13 mm)	nominal	reduced ductility

* OMF-A and SMF-A were the final post-test models used throughout the remainder of this report.

Figure 5–1(a) illustrates the influence of the initial gap between the beams and columns (item 3 above) on the vertical load-displacement response of the OMF specimen. The initial gap width determines the amount of rotation that the connections can accommodate before the gaps close. Once the gaps close, arching action develops in the beams, as discussed previously in Chapter 4, resulting in significant increases in vertical load accompanied by outward forces on the end columns. The results in Figure 5–1(a) show that increasing the initial gap from 0.50 in (13 mm) in model OMF-B (as assumed in the pre-test modeling) to 0.75 in (19 mm) in model OMF-A (as estimated directly from the test specimen) reduced the computed ultimate capacity of the specimen by 35 %.

Figure 5–1(b) shows the influence of reduced shear stud capacity (item 2 above) on the computed response of the OMF specimen. Model OMF-C included no reduction in the shear stud capacity (as in the pre-test modeling), while model OMF-A used a reduced shear capacity as discussed in Section 5.3.5. The drop in load at $\Delta = 3.5$ in (90 mm) for model OMF-A was associated with shear stud failure, and the ultimate capacity of model OMF-A is 24 % less than that of model OMF-C. Both factors illustrated in Figure 5–1 contributed to overestimation of the resistance of the OMF specimen by the pre-test model.

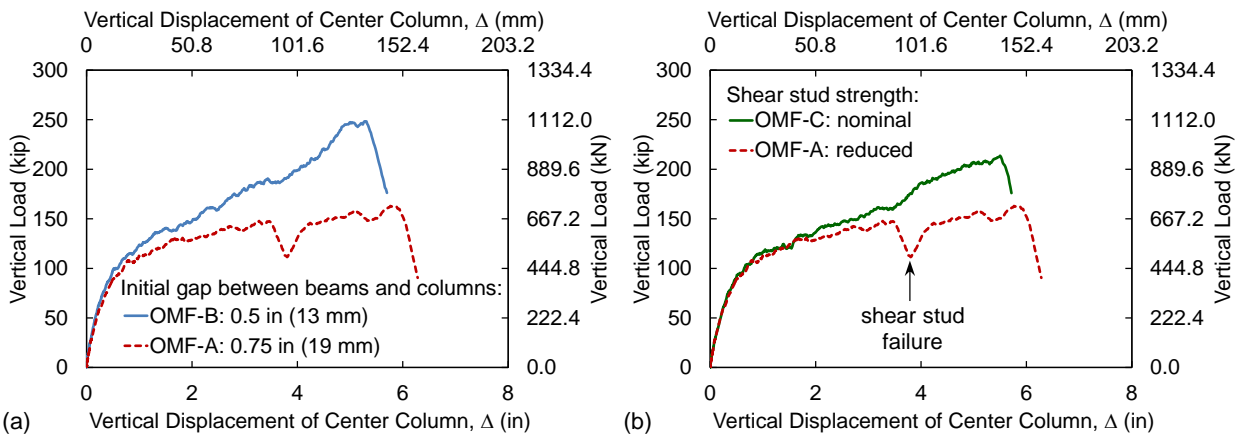


Figure 5–1. Influence of key factors on computed response of OMF specimen.

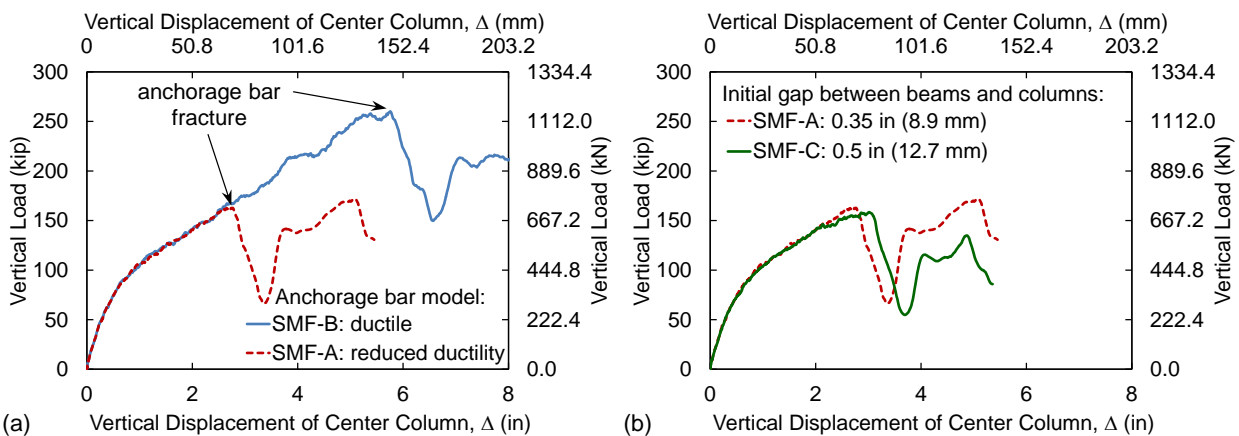


Figure 5–2. Influence of key factors on computed response of SMF specimen.

The response of the SMF specimen was strongly influenced by the assumed ductility of the anchorage bars near the weld (item 1b above), as illustrated in Figure 5–2(a). Model SMF-B considered no reduction

in the ductility of the anchorage bars (as in the pre-test modeling), while Model SMF-A accounted for reductions in ductility using the approach described in Section 5.4.2. While fracture of the first anchorage bar occurred at $\Delta = 6.0$ in (152 mm) in model SMF-B, Figure 5–2(a) shows that anchorage bar fracture occurred at half of this displacement in Model SMF-A, with a corresponding reduction of the ultimate capacity by 37 %.

Figure 5–2(b) shows the influence of the initial gap width on the computed response of the SMF specimen. Model SMF-C assumed a gap of 0.5 in (13 mm) (as in the pre-test modeling), while model SMF-A used the average actual gap width of 0.35 in (8.9 mm) from the test specimen. Figure 5–2(b) shows that the smaller initial gap width in model SMF-A resulted in slightly earlier fracture of the anchorage bars relative to model SMF-C. Model SMF-A also sustained larger vertical loads after anchorage bar fracture than model SMF-C through more extensive arching action resulting from the smaller initial gap. However, the influence of the initial gap width was not as great for the SMF specimen as for the OMF specimen, and the reduced ductility of the anchorage bars, as illustrated in Figure 5–2(a), was the primary reason that the pre-test model overestimated the resistance of the SMF specimen.

In addition to the three models of the SMF specimen listed in Table 5–1, a fourth model SMF-D was developed to investigate the sensitivity of the specimen to installation errors. As noted previously in Section 3.1, the beams of the SMF specimen were inadvertently installed in an inverted orientation, so that the longer anchorage bars were at the bottoms of the beams rather than at the tops, and a slight misalignment of the torsion rod sleeves also prevented installation of the torsion rods. For consistency with the test, models SMF-A, SMF-B, and SMF-C considered inverted beams with no torsion bars. Model SMF-D included torsion bars and non-inverted beams and was otherwise equivalent to model SMF-A. Comparison of the computed results showed small differences, with a slight delay in the fracture of the lower anchorage bars at the center column for model SMF-D relative to model SMF-A and an increase of the peak vertical load by 3.5 %. These results indicate that the installation errors did not significantly influence the response of the SMF specimen.

5.2 FINITE ELEMENT MODELS

Detailed finite element models, as illustrated in Figure 5–3, were developed to study the behavior and failure modes of the two test specimens. The finite element analyses were conducted using explicit time integration in LS-DYNA (Hallquist 2007), a general-purpose finite element software package. The analyses accounted for both geometric and material nonlinearities, including modeling the fracture of steel components using element erosion. In the analyses, the center column was pushed downward under displacement control until failure occurred. Displacements were increased at a sufficiently slow rate to ensure a quasi-static response, simulating the test conditions.

The models used 8-node solid elements to represent the concrete and the steel plates and angles (shown on the left-hand side in Figure 5–3), and 2-node beam elements to represent the reinforcing bars, torsion bars, and shear studs (shown on the right-hand side in Figure 5–3). The model of the OMF specimen consisted of approximately 346 000 elements, while the model of the SMF specimen consisted of about 171 000 elements. The characteristic length of the solid elements ranged from 0.25 in to 2.15 in (6.4 mm to 54.6 mm), and the level of refinement of the solid-element mesh is illustrated in Figure 5–4, which shows the mesh used to represent the moment connections at the center column for the SMF specimen. Typical beam elements ranged in length from 2.0 in to 5.3 in (51 mm to 135 mm), with smaller elements

in locally refined regions near the anchorage bar welds, as illustrated in Figure 5–5 and discussed subsequently in Section 5.4.1. An automatic contact interface was activated to prevent interpenetration and enable force transfer between the concrete beams and columns and the steel plates and angles.

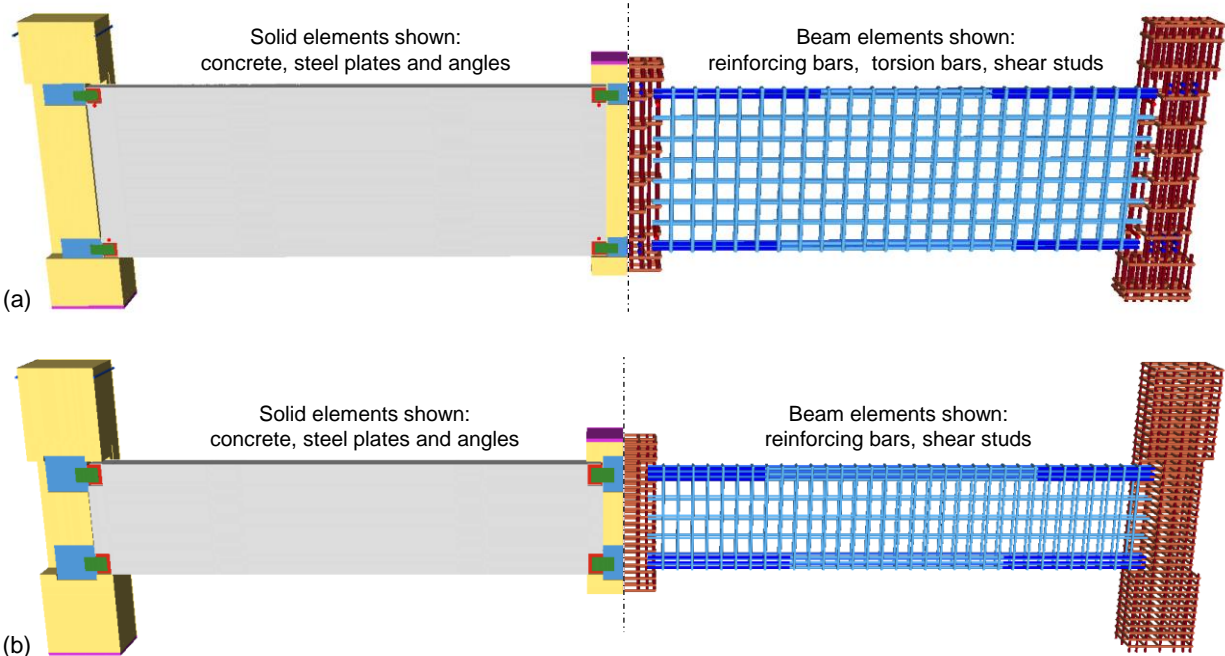


Figure 5–3. Finite element models: (a) OMF specimen; (b) SMF specimen.

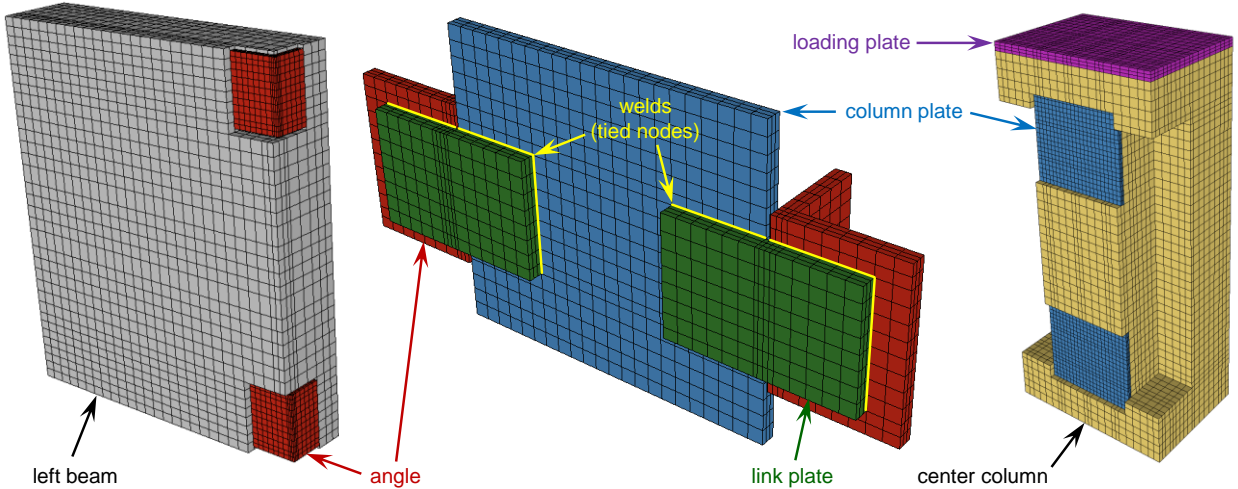


Figure 5–4. Solid-element mesh in connection region (SMF specimen).

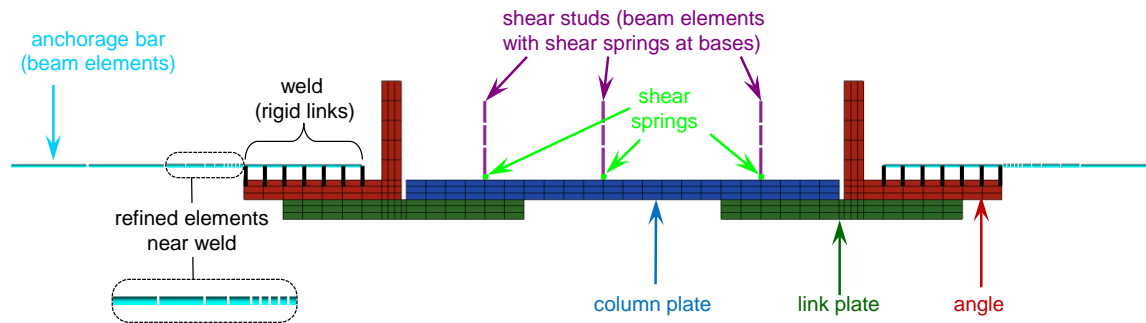


Figure 5–5. Modeling details at moment connection (top view).

Shear studs connecting the column plates to the column concrete were modeled using beam elements that shared nodes with the surrounding concrete elements. The nonlinear load-slip behavior of the shear studs was represented through discrete shear springs that connected the beam elements to the column plates, as illustrated in Figure 5–5 and further discussed in Section 5.3.5. Welds on the link plates were modeled using constraints that tied the nodes around the edges of the link plates to corresponding nodes on the angles and column plates, as indicated in Figure 5–4. Welds between the anchorage bars and the connecting angles were modeled using rigid links (`CONSTRAINED_NODAL_RIGID_BODY` in LS-DYNA), to capture the offset between the anchorage bar centerline and the surface of the connecting angle, as illustrated in Figure 5–5. These offsets contributed to the eccentricity in the transfer of forces between the anchorage bars and the link plates, producing significant out-of-plane bending moments in the link plates and in the anchorage bars near the welds, as discussed subsequently in Section 5.4.1. Nodal constraints (`CONSTRAINED_LAGRANGE_IN_SOLID` in LS-DYNA) were used to tie the anchorage bars, as well as the longitudinal and transverse reinforcing bars, to the surrounding concrete elements, and bond-slip effects were neglected. Welding of the column longitudinal bars to steel plates at the column bases was modeled by tying the longitudinal bars to nodes of the solid elements representing the steel base plates.

To represent the fixed base conditions for the end columns in the experimental configuration (see Figure 3–4), all translations were restrained for nodes on the bottom surfaces of the steel base plates. Restraint of the end column tops by bracing beams (see Figure 3–4) was represented through contact with rigid elements at the inside and outside faces of the end columns. Lateral bracing of the center column and at midspan of the beams was modeled using nodal constraints to prevent out-of-plane displacements.

5.3 MATERIAL MODELING

5.3.1 Concrete

A continuous surface cap plasticity model (material 159 in LS-DYNA) was used as the material model for concrete, with reduced integration solid elements. This material model was originally developed for roadside safety simulations for the Federal Highway Administration (FHWA 2007). Key features of the model include isotropic constitutive equations, a yield surface formulated in terms of three stress invariants with translation for pre-peak hardening, a hardening cap that expands and contracts, and damage-based softening with modulus reduction in both compression and tension. The model captures confinement effects, which are an important feature of concrete behavior, and uses a constant fracture energy approach to regulate mesh size sensitivity in the modeling of softening behavior. The material

model provides initialization routines whereby model parameters are fit to data for normal strength concrete with compressive strengths between 2900 psi and 8400 psi (20 MPa and 58 MPa) and aggregate sizes between 0.3 in and 1.3 in (8 mm and 32 mm). Required input parameters are the unconfined compressive strength and the maximum aggregate size. Because reduced-integration solid elements were used to model the concrete, hourglass control was required to suppress spurious zero-energy modes of deformation. An assumed strain co-rotational stiffness form of hourglass control was selected with an hourglass control coefficient of 0.03.

Figure 5–6 demonstrates the capabilities of the concrete material model to capture confinement effects in compression and brittle fracture in tension, based on single-element simulations using a cubic 8-node solid element. Figure 5–6(a) illustrates confinement effects by comparing the compressive behavior under uniaxial loading with that under triaxial loading with a constant confinement pressure of 600 psi (4 MPa). While the stress approaches zero in the softening phase for uniaxial compression, Figure 5–6(a) shows that moderate confinement pressure causes the material to maintain a residual compressive strength after softening. Figure 5–6(b) illustrates the brittle softening behavior of the material model in uniaxial tension. According to the default assumption in the material model, the fracture energy in uniaxial compression is taken as 100 times that in uniaxial tension.

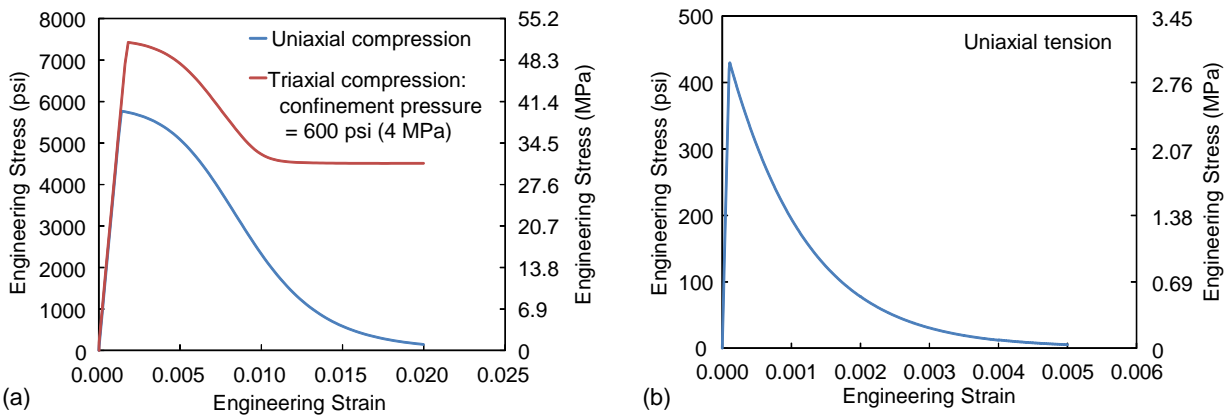


Figure 5–6. Stress-strain response of concrete material model: (a) compression; (b) tension.

5.3.2 Steel Plates and Angles

A piecewise linear plasticity model (material 24 in LS-DYNA) was used as the material model for the ASTM A36 steel plates and angles, which were modeled using fully integrated solid elements. In this model, the plastic material response is defined through a true stress vs. plastic strain curve, which can be obtained from an engineering stress-strain curve using the following relationships (e.g., Dieter 1976):

$$\sigma = s(e + 1) \quad (5.1)$$

$$\varepsilon = \ln(e + 1) \quad (5.2)$$

where σ is the true stress, s is the engineering stress, ε is the true strain, and e is the engineering strain. Letting E denote the elastic modulus, the plastic strain is then obtained as:

$$\varepsilon_p = \varepsilon - \frac{\sigma}{E} \quad (5.3)$$

A representative stress-strain curve was used for the steel plates and angles, based on tensile testing of ASTM A36 steel coupons reported by Sadek et al. (2010). This curve, shown up to the ultimate tensile strength in Figure 5–7(a), assumed a yield strength of $F_y = 42$ ksi (290 MPa), an ultimate tensile strength of $F_u = 65$ ksi (448 MPa), and an engineering strain of $e_u = 0.22$ at the ultimate tensile strength.

Eqs. (5.1) – (5.3) apply only up to the onset of necking at the ultimate tensile strength. To model the softening and fracture that could occur beyond this point, the true stress vs. plastic strain curve was extended linearly, and a critical plastic strain was defined at which element erosion would be activated, removing elements from the analysis to simulate fracture. Because modeling of softening and fracture is mesh-size dependent, this approach required calibration of the erosion strain and the post-ultimate tangent modulus for the specific element size used at critical regions in the models, in order to achieve values of engineering strain that were consistent with coupon tensile testing. However, this post-ultimate modeling approach had a negligible influence on the computed results for the test specimens, since fracture did not occur in the plates or angles.

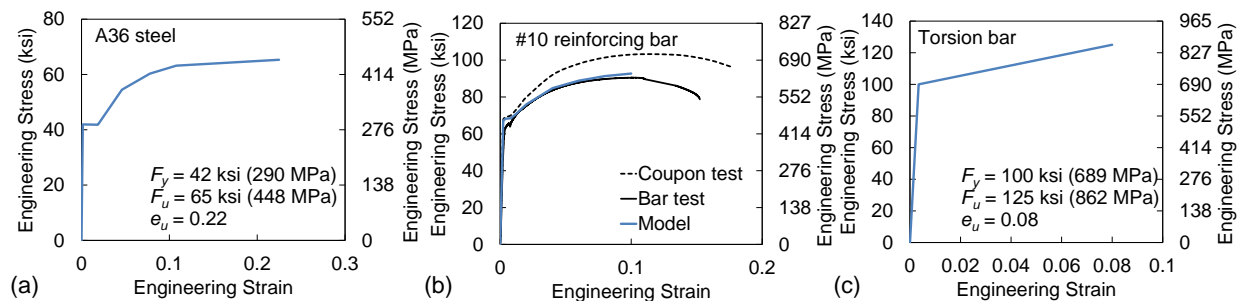


Figure 5–7. Stress-strain curves used to model steel components.

5.3.3 Reinforcing Bars

A piecewise-linear plasticity model (material 124 in LS-DYNA) was used as the material model for the reinforcing bars, which were modeled using Hughes-Liu beam elements with cross-section integration. This material model defines the material response through true stress vs. plastic strain curves, similar to the model used for the steel plates and angles. A distinct material model was defined for each size of reinforcing bar used in the test specimens, with stress-strain curves for each bar size based on data from tensile testing reported in Table 3–1. As noted in Table 3–1, two types of tensile tests were performed for the No. 10 and No. 11 bars: (a) direct tensile testing of reinforcing bars and (b) tensile testing of smaller-diameter coupons machined from the reinforcing bars. For the smaller bar sizes, only coupon testing was performed, which is known to give consistently higher tensile strength values than bar testing, as illustrated in Figure 5–7(b) for a No. 10 reinforcing bar. The lower tensile strength from bar testing is the appropriate value to use in modeling of reinforcing bars, and so the stress-strain curves used to model the No. 10 and No. 11 bars were based on tensile test results from bar testing, as illustrated in Figure 5–7(b). Because only coupon test data were available for the smaller bar sizes, these bars were modeled using approximate stress-strain curves that accounted for the reduced tensile strength that would be expected from bar testing, based on the reduction factor obtained for the No. 10 and No. 11 bars. This approximate reduction in the tensile strength did not significantly affect the overall behavior, because the strains in the reinforcing bars remained fairly small except at critical locations in the No. 10 and No. 11 anchorage bars near the welds. Modeling of these critical regions is discussed in Section 5.4.

5.3.4 Torsion Bars

The torsion bars, which were ASTM A193 Grade B7 bolts, were modeled using the same piecewise linear plasticity material model and beam element formulation that were used for the reinforcing bars. The torsion bars were modeled using the minimum specified tensile strength of $F_u = 125$ ksi (862 MPa), with a yield strength of 100 ksi (689 MPa), and an assumed engineering strain of $e_u = 0.08$ at the ultimate tensile strength. A simple bilinear form of stress-strain curve was assumed, as shown in Figure 5–7(c). To model the pre-tension introduced in the torsion bars during the assembly process, a coefficient of thermal expansion was defined in the material model, and the torsion bar elements were artificially cooled to develop tensile stresses through restraint of thermal contraction. Several trial analyses were performed to determine the reduction in temperature required to achieve the desired service tension of 18 kip (81 kN), as listed in the PCI Design Guide (PCI 2014, page 6–105).

5.3.5 Shear Studs

Discrete shear springs, as illustrated previously in Figure 5–5 (implemented in LS-DYNA using material 119), were used to represent the nonlinear shear behavior of the shear studs that connected the column plates to the column concrete. Figure 5–8 shows the normalized shear force vs. slip model used for the shear springs. The initial portion of the model curve is based on the empirical load-slip relationship proposed by Ollgaard et al. (1971), and this empirical curve is also plotted in Figure 5–8. While the empirical curve is plotted up to a slip of 0.5 in (13 mm), it is noted that this curve is only intended to represent the initial load-slip behavior up to the peak load at a slip of 0.2 in (5 mm). After reaching the peak load, the shear force is gradually reduced to 80 % of its peak value at a displacement of 0.40 in (10 mm) and is then steeply reduced to a constant residual strength equal to 20 % of its peak value. This residual strength represents the frictional resistance of crushed concrete that remains even after failure of a shear stud.

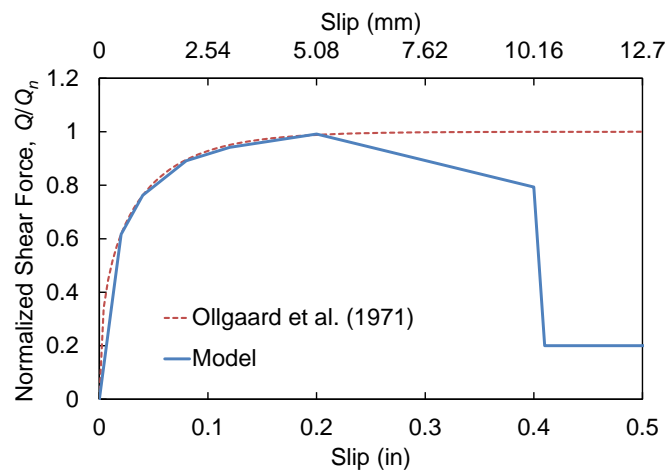


Figure 5–8. Normalized shear force vs. slip relationship used for shear studs.

For the 1.0 in (25 mm) diameter shear studs used in the OMF and SMF connections (see Figure 2–3 and Figure 2–4), a nominal shear strength of $Q_n = 38$ kip (170 kN) was calculated based on the AISC Specification (AISC 2010, Section I8.2a), assuming a tensile strength of $F_u = 65$ ksi (450 MPa) for the shear studs, which is the minimum specified tensile strength for AWS D1.1 Type B studs (AWS 2010).

This nominal shear strength was used in the model of the SMF specimen, and no shear stud failure occurred, consistent with the experimental results. However, using this nominal shear strength for the OMF specimen failed to capture the experimentally observed detachment of the upper column plates from the end columns and significantly overestimated the vertical load sustained by the OMF specimen (see results for model OMF-C in Figure 5–1).

As shown in Figure 4–3 and Figure 4–7, detachment of the column plates in the OMF specimen involved not only shear slip, but also significant out-of-plane displacement, which resulted from out-of-plane bending of the link plates. The shear studs were thus subjected a complex state of loading that involved not only shear forces, but also axial tension, and this tension reduced the effective shear capacity of the shear studs. This effect was more significant for the OMF specimen than for the SMF specimen because of the more extensive out-of-plane bending of the link plates that occurred, as noted previously in Section 4.2.3. Developing a failure model for the shear studs that explicitly accounts for the complex interaction of stresses observed here would require further research and is beyond the scope of this study. The key observation is that these effects reduced the effective shear capacity of the shear studs, and accounting for this reduction was necessary to capture the experimentally observed failures. In model OMF-A (the final post-test model), an effective shear strength of 12 kip (53 kN) was used for the shear studs, which represents only 31 % of the nominal shear strength. This value was calibrated to the experimental data in order to capture the column plate detachment observed at a center column displacement of $\Delta = 3.7$ in (89 mm).

An alternative estimate for the effective strength of the shear studs in the OMF specimen can be obtained by noting that the upper anchorage bar at the left end column developed a peak axial force of 86.6 kip (385 kN) just prior to detachment of the column plate (see Figure 4–16). Assuming that both anchorage bars at that location carried approximately the same axial force, the total peak shear force transferred to the column by the shear studs was about 173 kip (770 kN). Dividing this force among the nine shear studs gives an average shear strength of 19 kip (86 kN) per stud. While this experimentally based estimate is somewhat higher than that obtained by calibration of the computational model, it is still only 50 % of the nominal shear strength, thus confirming that out-of-plane bending significantly reduced the effective strength of the shear studs in the OMF specimen.

5.4 WELDED ANCHORAGE BAR MODELING

Item 1 in Section 5.1 introduced two key factors that influenced the fractures of the welded anchorage bars observed in the experiments: (a) localized bending moments near the welds and (b) reductions in the ductility of the anchorage bars in the heat-affected zone near the welds. The first of these factors resulted in interaction of bending moment and axial tension that played a key role in the fracture of the anchorage bars for both the OMF and SMF specimens, and Section 5.4.1 describes the procedure that was used to properly capture these effects. The second factor was significant only for the SMF specimen, and Section 5.4.2 describes the procedure that was used to account for the weld-induced reductions in ductility through calibration against component testing of a welded anchorage bar from the SMF specimen.

Weld-induced reductions in ductility of the anchorage bars may have been more significant for the SMF specimen than for the OMF specimen because of the greater heat input associated with the larger weld size (compare Figure 2–4 and Figure 2–3). Variability in the welding process may also have contributed to the differences, because even for the SMF specimen, reductions in ductility seem to have been more significant for some bars than for others. In the SMF specimen test (see Section 4.2), the lowest anchorage bar at the center column connection fractured first at $\Delta = 2.5$ in (64 mm), while the upper two

anchorage bars fractured later at $\Delta = 4.9$ in (124 mm). This contrasts with the computational results (see Figure 5–2(a)), in which all three anchorage bars, which were assumed to have the same ductility, fractured nearly simultaneously. These fractures occurred earlier in model SMF-A (with reduced ductility) than in model SMF-B (with no reduction in ductility) but were nearly simultaneous in both models. The earlier fracture of the lowest anchorage bar in the SMF specimen suggests that reductions in ductility caused by welding may have been more significant for this bar than for the upper two bars. This indicates the potential for significant variability in the extent to which ductility is reduced by the process of hand-welding a deformed bar to a plate or angle. Section 6.7.3 of the PCI Design Handbook (PCI 2014) discusses preheat and other requirements for welding of reinforcing bars to avoid potential crystallization and the associated brittle behavior.

5.4.1 Interaction of Bending Moment and Axial Force

The welded anchorage bars were subjected to a combination of bending and axial loading due to eccentricities in the transfer of forces between the link plates and the anchorage bars (see Figure 4–44). The resulting interaction of bending moment and axial tension (see Figure 4–18) caused the anchorage bars to fracture at a lower axial force than if the bars had been subjected to pure tension. Because detailed modeling of the welded anchorage bars using solid elements would be too computationally demanding for analysis of an entire test specimen, a reduced-order modeling approach was used, illustrated previously in Figure 5–5, in which the welded anchorage bars were modeled using beam elements. However, detailed solid-element models of welded anchorage bars under eccentric loading were also developed, as illustrated in Figure 5–9, to verify the adequacy of the reduced-order modeling approach and to enable calibration of the failure criterion used to model bar fracture. Figure 5–9 shows detailed and reduced-order models of a welded #10 anchorage bar, as used in the OMF moment connections. Corresponding detailed and reduced-order models were also developed of a welded #11 anchorage bar, as used in the SMF moment connections.

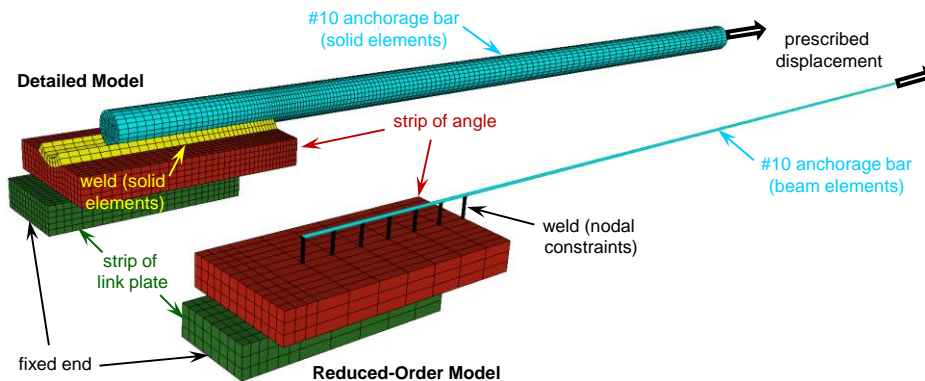


Figure 5–9. Finite element models of a welded anchorage bar under eccentric loading: (a) detailed model; (b) reduced model.

The welded anchorage bar models used for calibration included a single anchorage bar along with strips of angle and link plate having widths obtained by dividing the actual widths (see Figure 3–1 and Figure 3–2) by the number of anchorage bars in the connection. Concrete was excluded from the models, because the focus of these analyses was on the transfer of forces through the steel components at the welded connections. In the detailed models, the anchorage bars, welds, angles, and link plates were modeled using solid elements. The reduced-order models were consistent with the modeling approach

used for the moment connections in the OMF and SMF specimens (see Figure 5–5), in which the anchorage bars were modeled using beam elements, the welds were modeled using nodal constraints, and the angles and link plates were modeled using a coarser mesh of solid elements than was used in the detailed models. In both the detailed and reduced-order models, the welds between the angle and the link plate were modeled by having elements of the two components share common nodes at their interface. Only the leg of the angle that was parallel to the link plate was included in the models, because the perpendicular leg was not loaded in the configuration being analyzed. The portion of the link plate that was welded to the column plate was not included in the model. Instead, the link plate was truncated at the edge of the column plate, and this truncated end was modeled as fixed (see Figure 5–9). A segment of anchorage bar extending 30 in (762 mm) beyond the end of the angle was modeled, and displacement-controlled axial loading was applied to the end of this bar segment. Eccentricity in the loading resulted from the offset (in the direction normal to the link plate) between the load applied to the anchorage bar and the reaction at the fixed end of the link plate.

As subsequent computational results show (see Figure 5–12), the bending moment was largest at the end of the weld and decayed steeply with distance along the bar. To capture this localized bending of the anchorage bars in the reduced-order models, a refined mesh was required near the weld (see Figure 5–5). After considering various mesh sizes in this refined zone, a beam element length of 0.2 in (5 mm) was selected, which was found to be sufficient to capture the maximum bending moment at the end of the weld, as well as the decay in bending moment along the length of the bar. The nonlinear distribution of axial stress over the cross-sectional area of the bar was captured using 64 integration points per element. Fracture was modeled using element erosion at a specified value of plastic strain. However, plastic strains were found to localize in the single element closest to the weld, where the bending moment and corresponding stresses were largest. Because of this localization, modeling of fracture in the reduced-order models was found to be mesh-size dependent, and calibration of the erosion strain for the selected element size was necessary. As described in the following, the failure criterion used in the detailed models was first calibrated against tensile test data, and then the failure criterion used in the reduced-order models was calibrated against the detailed models.

The detailed models used a piecewise linear plasticity model for the anchorage bars (material 24 in LS-DYNA), with fully integrated solid elements. True stress vs. plastic strain curves for use in the material model were calculated from tensile test data for #10 and #11 bars using Eqs. (5.1) – (5.3), and these true stress vs. plastic strain curves were extended linearly beyond the onset of necking to model softening prior to fracture. The detailed models used the same material model for the welds as for the anchorage bars. Fracture of the anchorage bars in the detailed models was modeled using element erosion, and the erosion strain in the detailed models was calibrated against experimental data from tensile tests. This calibration was performed by modeling tensile tests of #10 and #11 bars (illustrated in Figure 5–10 for a #10 bar) and adjusting the erosion strain so that the engineering strain at fracture (point *d* in Figure 5–10) matched the value obtained experimentally. For consistency with the experimental results (see Table 3–1), a gauge length of 8 in (203 mm) was used in calculating engineering strain values from the computational models. Because modeling of erosion and fracture is mesh-size dependent, the bars in the tensile test models used the same solid-element mesh as in the welded bar models (Figure 5–9).

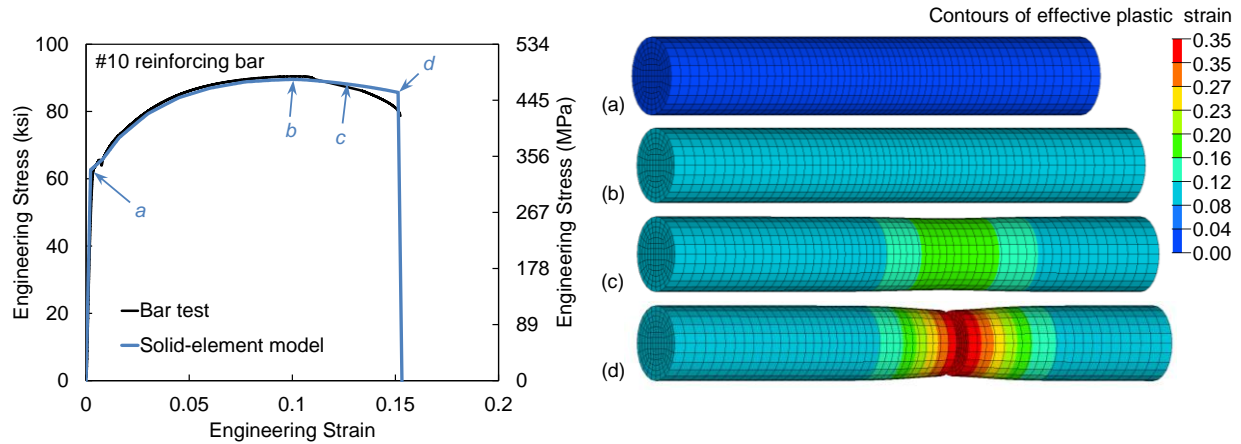


Figure 5–10. Calibrated detailed model analysis of reinforcing bar tensile test.

After calibrating the modeling of bar fracture under uniaxial tensile loading, the detailed models were used to analyze the response of the welded anchorage bars under eccentric tensile loading. Figure 5–11 shows computed results from the detailed model of the welded #10 bar shown in Figure 5–9. The interaction diagram of axial tension vs. bending moment is plotted, and for the points labeled on the interaction diagram, the corresponding deformed geometry of the finite element mesh is shown with contours of effective plastic strain. The computed deformations are comparable to the schematic illustration presented previously in Figure 4–15(a). Plastic strains were concentrated in the link plate near the fixed end and in the anchorage bar near the end of the weld. The final point on the interaction diagram (point *d*) corresponds to the initiation of fracture at the peak axial load. The deformed shape after complete fracture is also shown in Figure 5–11(e).

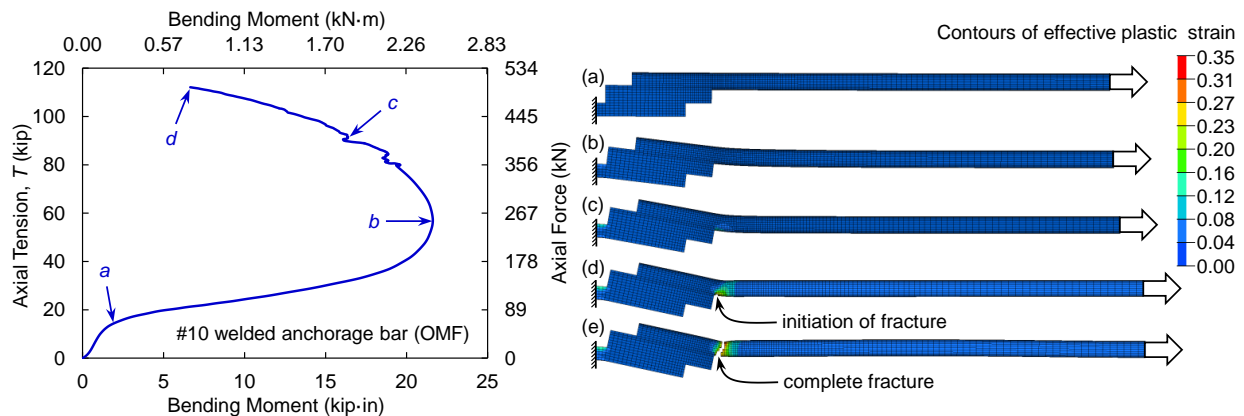


Figure 5–11. Detailed model analysis of welded anchorage bar under eccentric loading.

The values of bending moment plotted in Figure 5–11 were calculated for the cross section at the end of the weld, where the bending moment was largest. Figure 5–12 shows the variation of bending moment with distance along the bar for two different levels of axial tension, corresponding to points *b* and *c* in Figure 5–11. At the lower level of axial tension (point *b*), the bending moment decays to 50 % of its peak value at a distance of 3.3 in (84 mm) from the end of the weld. At the higher level of axial tension (point *c*), the bending moment decays even more steeply, dropping to 50 % of its peak value at a distance of only 0.8 in (20 mm) from the end of the weld. This steep decay in bending moment with distance explains why the reduced modeling approach required such short beam elements for the anchorage bar near the

weld (see Figure 5–5). The pre-test model used much larger beam elements in this region and thus failed to adequately capture the local bending effects.

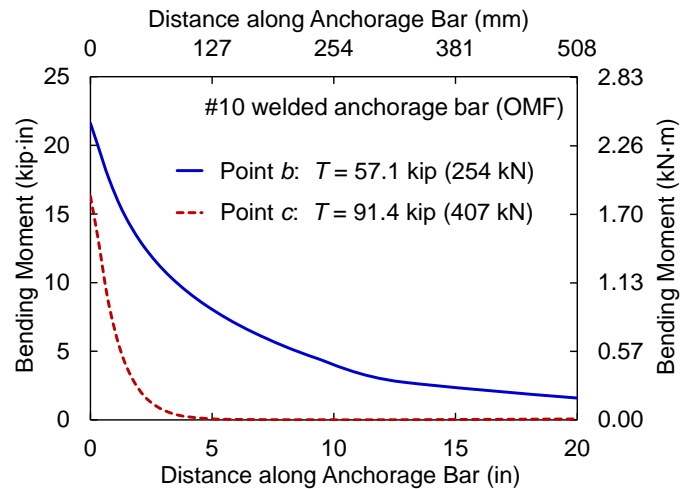


Figure 5–12. Bending moment in welded anchorage bar vs. distance along bar.

Figure 5–13 shows a comparison of moment-axial interaction diagrams obtained using the detailed and reduced models of the welded anchorage bars under eccentric loading. Figure 5–13(a) presents results for the #10 anchorage bar models shown in Figure 5–9, while Figure 5–13(b) presents corresponding results for the #11 anchorage bar models. For each bar size, the erosion strain used in the reduced model was calibrated so that the detailed and reduced models had approximately the same ratio of bending moment to axial force at the fracture point. Graphically, this required the fracture points for the detailed and reduced models to lie approximately along the same ray directed from the origin of the moment-axial interaction diagram, as indicated with the dashed arrow annotation in Figure 5–13. This calibration approach was adopted in an effort to best match the degree of moment-axial interaction at the point of fracture, rather than seeking to match either the bending moment or the axial force at the expense of the other. The results show fairly good agreement between the interaction diagrams obtained using the detailed and reduced modeling approaches. The peak bending moment and the peak axial force both agree within 6 % for the #10 bar and within 9 % for the #11 bar. This good agreement confirms that the reduced modeling approach is able to capture the interaction of bending moment and axial tension leading to fracture of the anchorage bars.

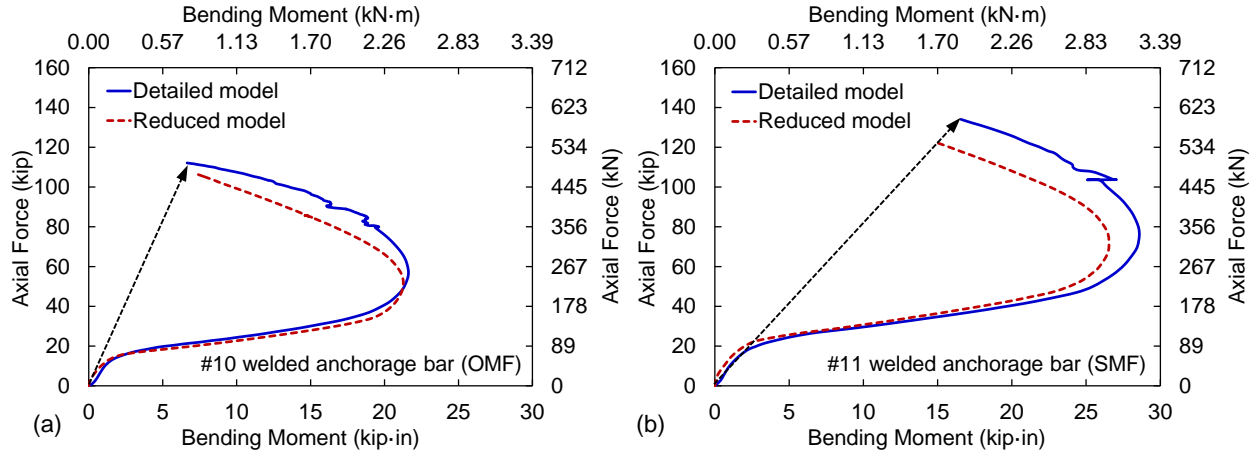


Figure 5–13. Interaction of axial force and bending moment for welded anchorage bars under eccentric loading: (a) #10 bar, (b) #11 bar.

5.4.2 Reduction of Ductility in Heat-Affected Zone

When the calibrated, reduced model of the welded #10 anchorage bar [Figure 5–13(a)] was implemented in analysis of the OMF specimen, the model closely captured the center column displacement at which anchorage bar fracture occurred. In contrast, when the calibrated, reduced model of the welded #11 anchorage bar [Figure 5–13(b)] was implemented in analysis of the SMF specimen (model SMF-B in Section 5.1), anchorage bar fracture in the model occurred significantly later than observed experimentally. To investigate the cause of the earlier anchorage bar fracture observed experimentally, component testing of a welded anchorage bar from the SMF specimen was performed, as illustrated in Figure 5–14.

The welded anchorage bar connection used in the component test was recovered from a location in the tested SMF specimen that was subjected to predominantly compressive loads during the test. The three-bar connection (see Figure 2–4) was sawed through the angle and link plate to isolate a single anchorage bar for testing, along with a strip of angle with a width of 4.5 in (114 mm) welded to the #11 bar. The angle and link plate were welded together along the sawed edge, and the link plate was also sawed flush with the heel of the angle. A nut was welded to the perpendicular leg of the angle to receive a 2 in (51 mm) diameter threaded rod, through which tensile loading was applied in the testing machine [Figure 5–14(b)]. The nut was aligned along the axis of the anchorage bar to provide concentric axial loading. Steel bars with dimensions of 8 in \times 1 in \times 0.5 in (203 mm \times 25 in \times 13 mm) were welded diagonally between the two legs of the angle to stiffen the angle and prevent out-of-plane deformations. Elongations of the anchorage bar were measured using a displacement transducer spanning a gauge length of 30 in (762 mm) and attached to the toe of the angle, at the end of the weld. The estimated uncertainty in the measured load and displacement data was ± 1 %. The welded anchorage bar was tested under displacement-controlled tensile loading until fracture occurred.

The results of the welded bar component test are shown in Figure 5–15. Figure 5–15(a) shows the stress-strain curve obtained from the welded bar component test, along with that obtained from tensile testing of a #11 bar for comparison. The yield stress is almost equivalent in both cases, and the welded bar showed only slightly lower stress in the post-yield work-hardening phase. However, the welded bar had significantly reduced ductility, with the ultimate stress being reached at an engineering strain of 9.3 % and

fracture occurring immediately thereafter, without appreciable necking. In contrast, the ultimate stress was reached at an engineering strain of 11.1 % in the bar tensile test and was followed by significant necking and softening prior to fracture. Figure 5–15(b) shows the fractured anchorage bar after the component test, in which it is evident that the fracture occurred at the end of the weld. The reduced ductility of the welded anchorage bar is believed to have been caused by changes in material properties in the heat-affected zone near the weld (e.g., microstructural changes such as the formation of brittle martensite).

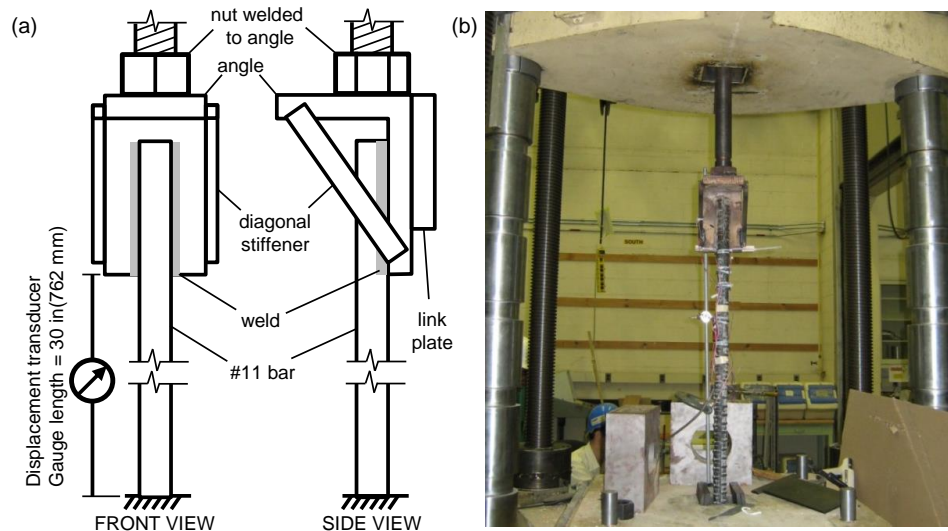


Figure 5–14. Component test setup for welded anchorage bar.

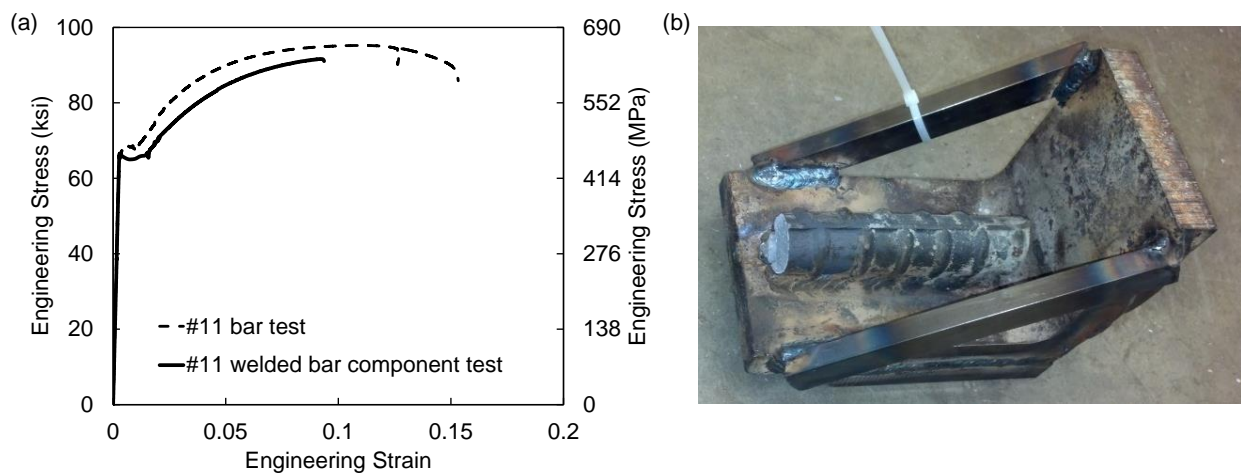


Figure 5–15. Results of welded anchorage bar component test: (a) stress-strain curve; (b) fractured anchorage bar.

Based on the results of the welded bar component test, the reduced model of the welded #11 anchorage bar [Figure 5–13(b)] was recalibrated to account for the reduced ductility that was observed. This recalibration followed the same procedure outlined in Section 5.4.1, but with one modification: rather than calibrating the anchorage bar material model against a bar tensile test, as illustrated previously in

Figure 5–10, the material model was instead calibrated against the welded bar component test, as illustrated in Figure 5–16.

Figure 5–16(a) shows the detailed model used to calibrate the anchorage bar material model against the welded bar component test. The concentric loading conditions in the welded bar component test were simulated by constraining axial displacements for all nodes on a plane located 0.45 in (12 mm) from the end of the angle, which corresponds to the end of the welds that affixed the diagonal stiffeners the angle. This approach was found suitable to achieve concentric loading of the welded anchorage bar without the need to model the full details of the diagonal stiffeners and the concentrically located loading nut used in the component test (Figure 5–14). The true stress vs. plastic strain curve used in the anchorage bar material model was obtained from the welded bar component test data using Eqs. (5.1) – (5.3), with a linear extension beyond the ultimate tensile strength. To represent the reduced ductility in the heat-affected zone near the weld, as indicated in Figure 5–16(a), element erosion was activated only for anchorage bar elements adjacent to the weld and within one row of elements beyond the end of the angle. The erosion strain was adjusted to match the experimental engineering strain at fracture, as shown in Figure 5–16(b).

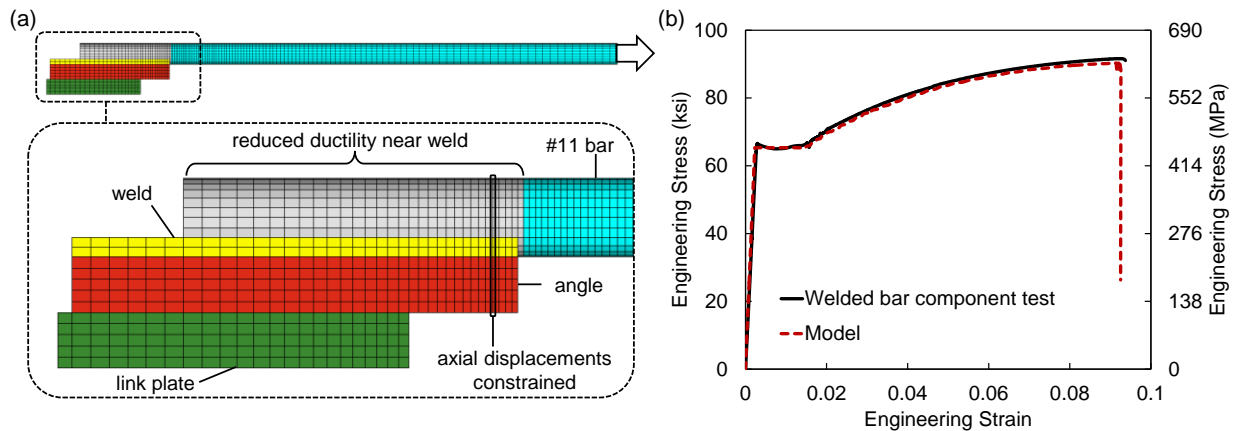


Figure 5–16. Calibrated detailed model of welded anchorage bar component test.

After calibrating the anchorage bar material model against the welded bar component test, the welded bar was analyzed again under the eccentric loading and support conditions illustrated in Figure 5–9. The resulting moment-axial interaction diagram is shown in Figure 5–17, along with corresponding results from the reduced model. As was done previously in Figure 5–13, the erosion strain used in the reduced model was calibrated so that the detailed and reduced models had approximately the same ratio of bending moment to axial force at the fracture point. Comparing Figure 5–17 with Figure 5–13(b) reveals that the reduction in ductility due to welding led to a 35 % reduction in the peak tensile force that could be sustained under eccentric loading. Because the tensile capacity from the welded bar component test (under concentric loading) was only 4 % less than that of the bar without welding [see Figure 5–15(a)], this shows that moment-axial interaction under eccentric loading can amplify the effects of reduced ductility. This helps to explain why the ultimate capacity of model SMF-A, which had anchorage bars with reduced ductility, was so much less than that of model SMF-B, which had ductile anchorage bars [see Figure 5–2(a)].

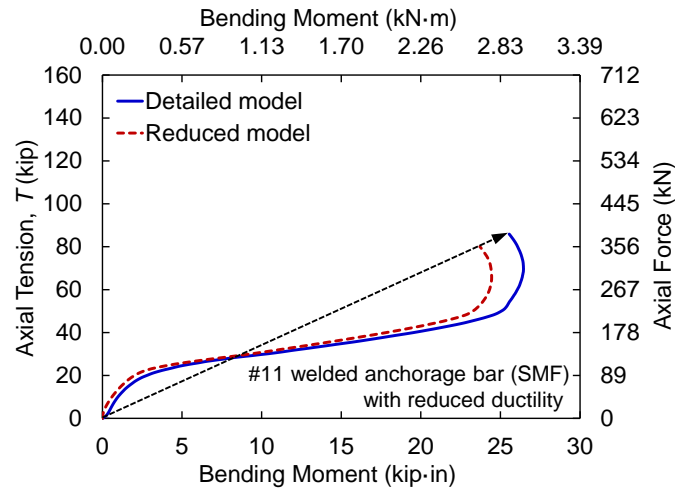


Figure 5–17. Interaction of axial force and bending moment for welded #11 anchorage bar with reduced ductility under eccentric loading.

5.5 ANALYSIS OF TEST SPECIMENS

This section presents analysis results from the final post-test models of the OMF and SMF test specimens (models OMF-A and SMF-A in Table 5–1), including comparisons of the computed results with the experimental measurements. As discussed in Section 5.1, and further elaborated in Sections 5.3.5 and 5.4, the final post-test models incorporated refinements in modeling of the shear studs and the welded anchorage bars, in order to better capture the experimentally observed behaviors and failure modes.

In the analysis of each test specimen, self-weight loading was first applied gradually and then held constant for the rest of the analysis by imposing a body-force acceleration vs. time curve. After the specimen reached an equilibrium configuration under its own self-weight, the unsupported center column was pushed downward by prescribing a gradually increasing velocity vs. time curve to the steel loading plate at the top of the center column. Loads were transmitted to the center column through contact with the steel loading plate, consistent with the experimental configuration. The analysis results for each of the specimens are presented in the following subsections.

5.5.1 OMF Specimen

Figure 5–18(a) shows a comparison between the measured and computed curves of the applied vertical load vs. the vertical displacement of the center column. A slight drop in both the measured and computed vertical load is evident in Figure 5–18(a) at a center column displacement of $\Delta = 3.7$ in (89 mm), corresponding to shear stud failure at the top column plates on the end columns. As a result of this failure, a more severe drop occurred in both the measured and computed horizontal reaction from the front brace beam at the tops of the end columns, as shown in Figure 5–18(b).

Inward horizontal forces on the column tops are considered positive in Figure 5–18(b), corresponding to tension in the brace beam spanning between the tops of the end columns. The experimental curve in Figure 5–18(b) corresponds to the measured axial force in the front brace beam (Figure 4–24). While the brace beams themselves were not included in the computational model, their influence was represented through contact with rigid elements at the inside and outside faces of the end column tops. For

consistency with the experimental measurements, the curve from the computational model in Figure 5–18(b) represents the portion of the horizontal reaction that would have been transferred to the front W16x67 brace beam by the W14x82 cross beams (see Figure 3–4). The computed horizontal reactions at the tops of the two end columns were averaged, with inward forces positive. (The horizontal reactions at the two end column tops were essentially equivalent initially, but differences became evident after shear stud failure occurred and the response was no longer symmetric.) An outward horizontal reaction developed in the initial application of self-weight in the computational model, and for consistency with the experimental measurements, this initial reaction was deducted from the horizontal force values presented in Figure 5–18(b). The peak computed horizontal reaction from the front brace beam, prior to shear stud failure, was 29 % less than the peak force from the experimental data.

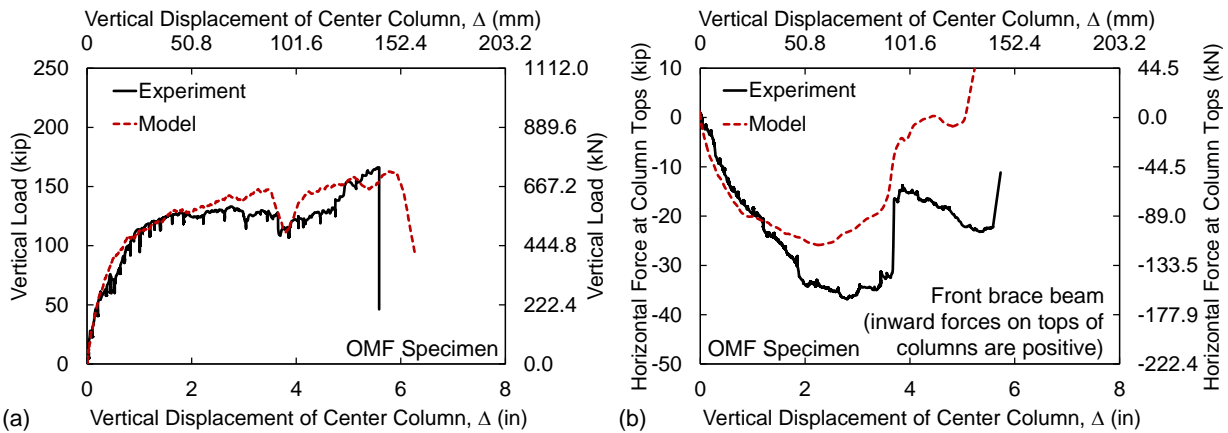


Figure 5–18. Comparison of experimental and computed results for (a) vertical load and (b) horizontal reaction from front brace beam at end column tops (OMF specimen).

Shear stud failure was evident in the computational model by increased displacements of the top column plates relative to the end columns, as indicated in Figure 5–19(a). Figure 5–19(a) shows a section view of the OMF model at the level of the top anchorage bars on the top link plates, at a center column displacement of $\Delta = 6.0$ in (151 mm), near the peak vertical load. Figure 5–19(b) shows a similar section view at the level of the bottom anchorage bars on the bottom link plates, in which shear stud failure is also evident through relative displacements of the column plates. As discussed in Section 5.3.5, shear stud failure in the OMF specimen was influenced by out-of-plane bending of the link plates, and significant out-of-plane bending of the link plates is evident in Figure 5–19, particularly at the center column, where balanced forces from the beams on each side prevented shear stud failures. The computed out-of-plane deformations of the link plates and anchorage bars shown in Figure 5–19 are consistent with the strain gauge measurements presented in Section 4.1.3 and illustrated schematically in Figure 4–15.

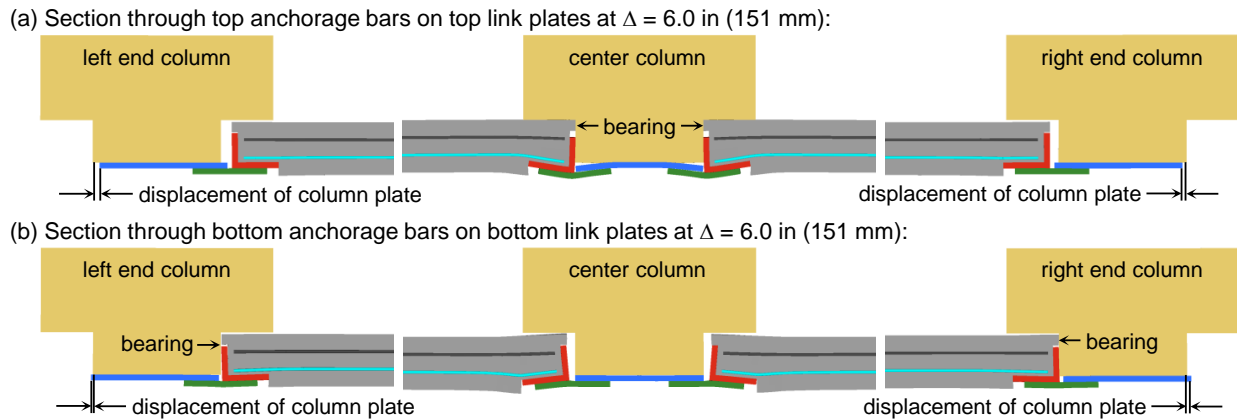


Figure 5–19. Section views of OMF model near the peak vertical load.

After shear stud failure, the OMF specimen developed additional capacity through arching action, with the top ends of the beams bearing against the center column, as indicated in Figure 5–19(a), and the bottom ends of the beams bearing against the end columns, as indicated in Figure 5–19(b). The deflected shape of the OMF specimen near the peak vertical load is shown in Figure 5–20, indicating a predominantly linear deflected profile of the beams between the connections, consistent with the experimental measurements (Figure 4–10). Contours of the concrete damage index near the peak vertical load are presented in Figure 5–21, which shows that concrete damage was concentrated in the regions surrounding the beam-to-column connections and in the lower portions of the end columns. Shortly after the onset of arching action, which was evidenced by bearing of the beams against the columns, inclined damage contours developed in the lower portions of the end columns. These inclined damage contours indicate the formation of diagonal shear cracks, consistent with the experimental observations (see Figure 4–5 and Figure 4–6).

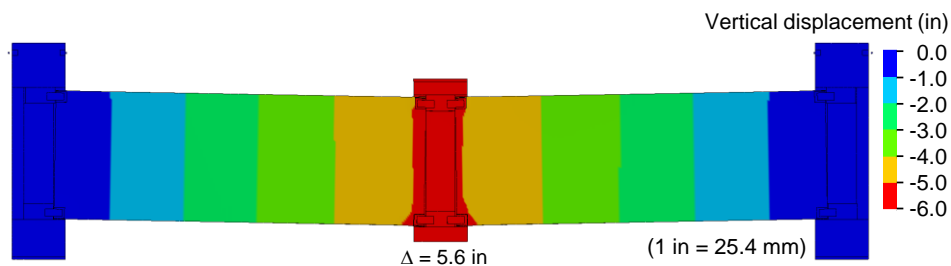


Figure 5–20. Deflected shape of OMF specimen prior to anchorage bar fracture.

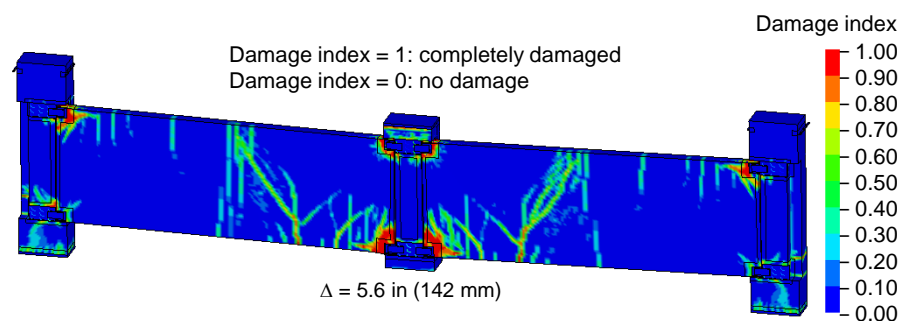


Figure 5–21. Concrete damage for OMF specimen prior to anchorage bar fracture.

Figure 5–22 shows the concrete damage near the top of the center column, a location where extensive spalling occurred, comparing (a) a photograph taken after the peak vertical load with (b) damage contours from the computational model at $\Delta = 6.1$ in (156 mm), also after the peak vertical load. While the concrete damage model is unable to capture discrete cracking and spalling, which are evident in Figure 5–22(a), the concentration of damage around the link-plate connections in the computational model is generally consistent with the damage in the OMF specimen. Out-of-plane bending of the link plates is also evident in Figure 5–22, and the deformed shape of the link plates in the computational model agrees quite well with the deformed shape shown in the photograph.

The computed vertical load reached a peak value of 163 kip (725 kN), within 2 % of the experimental peak load, at a center column displacement of $\Delta = 5.8$ in (147 mm). After reaching this peak value, the vertical load dropped sharply as a result of anchorage bar fracture, illustrated in Figure 5–23. Fracture of the anchorage bars resulted from a combination of bending moment and axial tension, and significant out-of-plane bending of the link plates and anchorage bars is evident in Figure 5–23, as was previously noted in Figure 5–19.

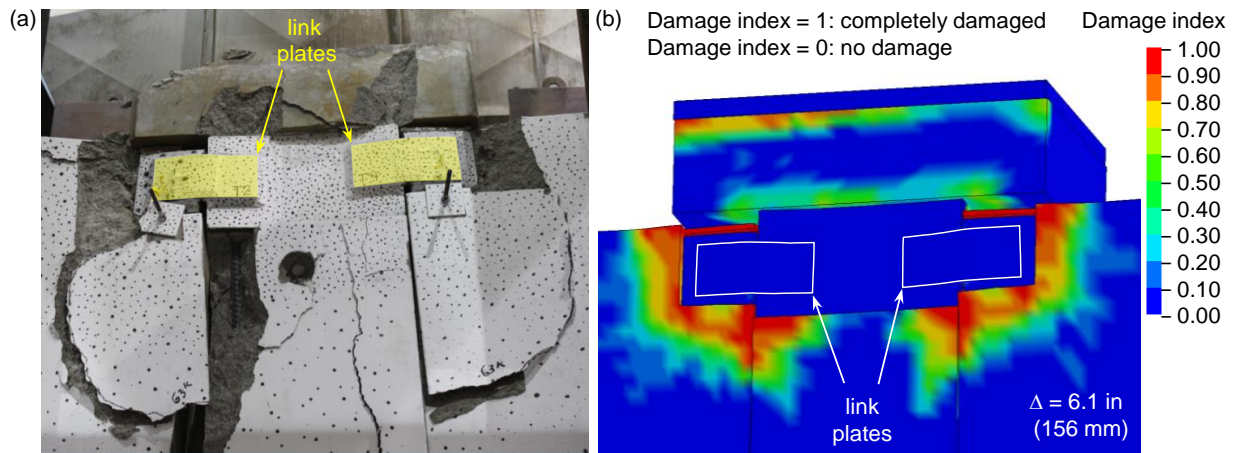


Figure 5–22. Concrete damage near top of center column for OMF specimen after anchorage bar fracture: (a) photograph; (b) contours of computed damage index.

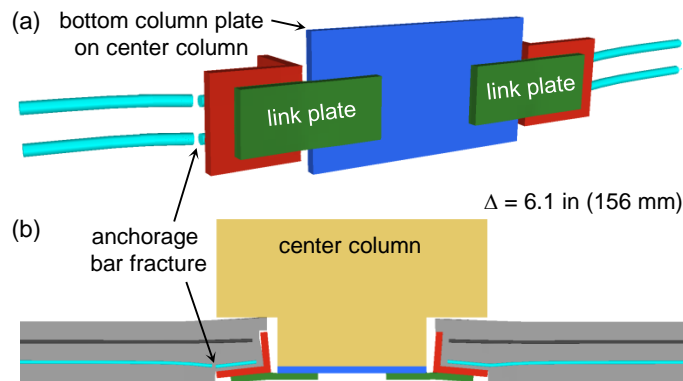


Figure 5–23. Anchorage bar fracture in OMF model: (a) perspective view; (b) section through bottom anchorage bars on bottom link plates.

Figure 5–24 shows the interaction of the computed bending moment and axial force in the lowest anchorage bar on the left side of the center column, in the critical element adjacent to the weld, where the initial fracture occurred. Limiting interaction boundaries corresponding to the yield strength and the ultimate strength of a #10 bar are also shown in Figure 5–24 for reference, calculated based on Chapter H of the 2010 AISC Specification (AISC 2010), where $M_y = S \cdot f_y$ is the yield moment, $T_y = A \cdot f_y$ is the yield capacity in tension, $M_u = Z \cdot f_u$ is the ultimate moment, $T_u = A \cdot f_u$ is the ultimate capacity in tension, S is the elastic section modulus, Z is the plastic section modulus, and f_y and f_u are the yield and ultimate strength values of the #10 bar obtained from tensile tests (see Table 3–1). Unloading and reloading of the anchorage bar, which occurred before fracture and is evident in Figure 5–24, was caused by the failure of shear studs. The final fracture point was slightly beyond the limiting interaction boundary corresponding to the ultimate strength. The tensile force at fracture was 84% of the ultimate tensile capacity, indicating a moderate reduction in tensile strength as a result of moment-axial interaction. The tensile force in the anchorage bar at fracture was within 1 % of the peak axial force calculated from strain gauge measurements (Figure 4–18, Section RC), showing excellent agreement between the experimental and computed fracture points. The computed values of bending moment in Figure 5–24 were larger than the experimental values in Figure 4–18 because of the steep decay in bending moment with distance along the anchorage bar (see Figure 5–12), since the bending moment was computed for a cross section located at the end of the weld, whereas the strain gauges were located 3.5 in (89 mm) from the end of the weld (see Figure 3–9).

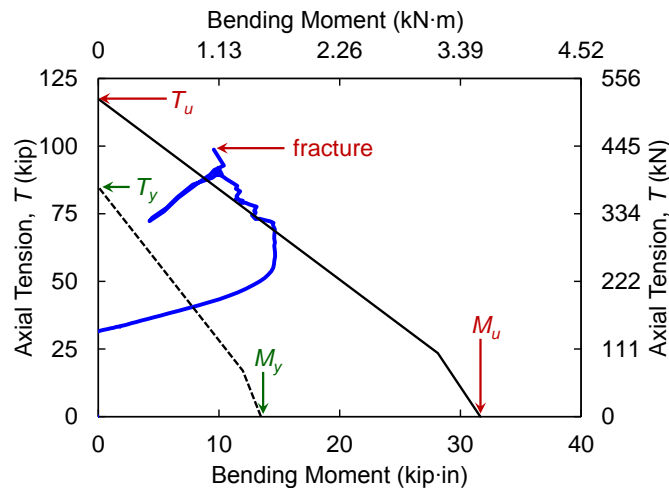


Figure 5–24. Bending moment and axial force interaction for anchorage bar of OMF model.

5.5.2 SMF Specimen

Figure 5–25 shows a comparison between the measured and computed curves of (a) the applied vertical load and (b) the horizontal reaction force at the end column tops for the SMF specimen, both plotted against the vertical displacement of the center column. Inward horizontal reaction forces are considered positive in Figure 5–25(b), corresponding to tension in the brace beams spanning between the tops of the end columns. The experimental curve in Figure 5–25(b) was obtained as the sum of the axial forces measured in the front and back brace beams (see Figure 4–42). The curve computed from the model in Figure 5–25(b) was obtained as the average of the horizontal reaction forces at the tops of the two end columns, with inward forces positive. An outward horizontal reaction developed in the initial application of self-weight in the computational model, and for consistency with the experimental measurements, this initial reaction was deducted from the horizontal force values presented in Figure 5–25(b).

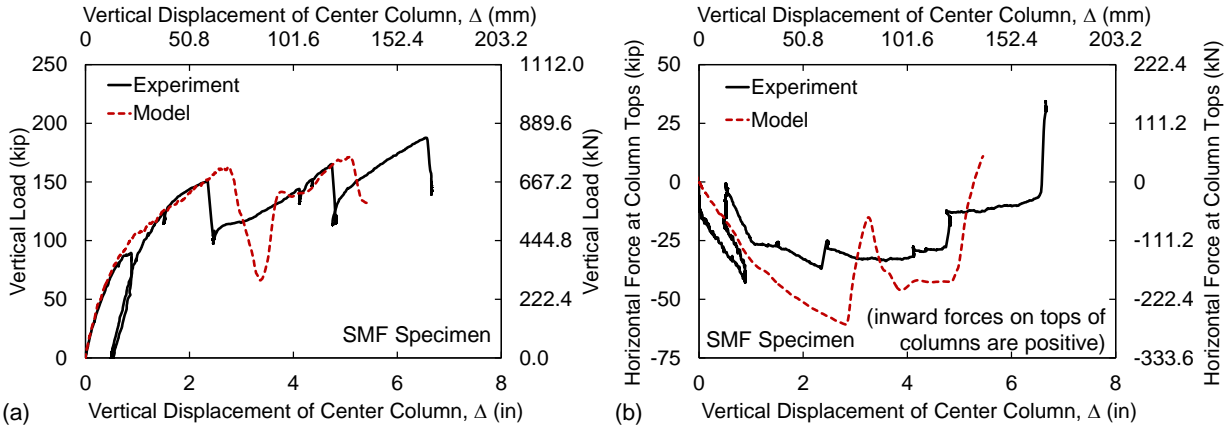


Figure 5–25. Comparison of experimental and computed results for (a) vertical load and (b) horizontal reaction from brace beams at end column tops (SMF specimen).

Figure 5–25(a) shows that the vertical load from the computational model reached an initial peak value of 163 kip (725 kN) at a vertical displacement of 2.8 in (70 mm), before dropping sharply as a result of anchorage bar fracture, shown in Figure 5–26. A corresponding drop in load is also evident in the computed horizontal reaction at the column tops in Figure 5–25(b). The measured and computed horizontal forces in Figure 5–25(b) agree fairly well initially, both showing outward horizontal reactions corresponding to compressive brace forces. However, when the specimen was unloaded and reloaded after the initial phase of loading (see Section 4.2.1), the measured horizontal force never again reached the peak horizontal force of 43 kip (191 kN) attained in the initial loading. The unloading and reloading cycle appears to have introduced some change in the horizontal restraint that was not captured by the computational model (which was not unloaded and reloaded), and consequently, the peak computed horizontal force exceeded the measured value by 42 %.

The three anchorage bars fractured nearly simultaneously in the model. This contrasts with the experiment, in which the lowest anchorage bar fractured first at $\Delta = 2.5$ in (64 mm) and the upper two anchorage bars fractured later at $\Delta = 4.9$ in (124 mm). As discussed previously in Section 5.4, these differences in the experimentally observed fracture points may be due to variations in the ductility of the anchorage bars in the heat-affected zones near the welds, whereas the model assumed the same ductility for all anchorage bars. Fracture of the anchorage bars resulted from a combination of bending moment and axial tension, and out-of-plane bending of the link plates and anchorage bars is evident in Figure 5–26, although not as pronounced as it was for the OMF specimen in Figure 5–23.

Figure 5–27 shows the interaction of the computed bending moment and axial force in the lowest anchorage bar on the left side of the center column, in the critical element adjacent to the weld, where fracture occurred. Limiting interaction boundaries corresponding to the yield strength and the ultimate strength of a #11 bar are also shown in Figure 5–27 for reference, as were shown previously in Figure 5–24 for a #10 bar. As a result of the larger bar size, computed values of bending moment in the anchorage bars are larger for the SMF specimen in Figure 5–27 than for the OMF specimen in Figure 5–24. The final fracture point was slightly beyond the limiting interaction boundary corresponding to the ultimate strength. The tensile force at fracture was 66 % of the ultimate tensile capacity, indicating a significant reduction in capacity that resulted from the combined effects of (a) moment-axial interaction and (b) reductions in ductility of the bar in the heat-affected zone near the weld.

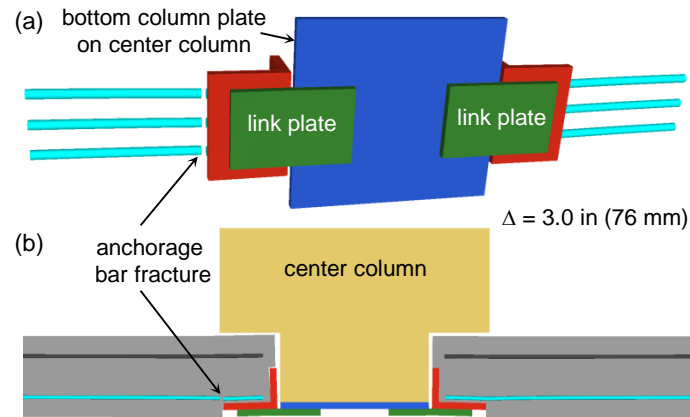


Figure 5–26. Anchorage bar fracture in SMF model: (a) perspective view; (b) section through bottom anchorage bars on bottom link plates.

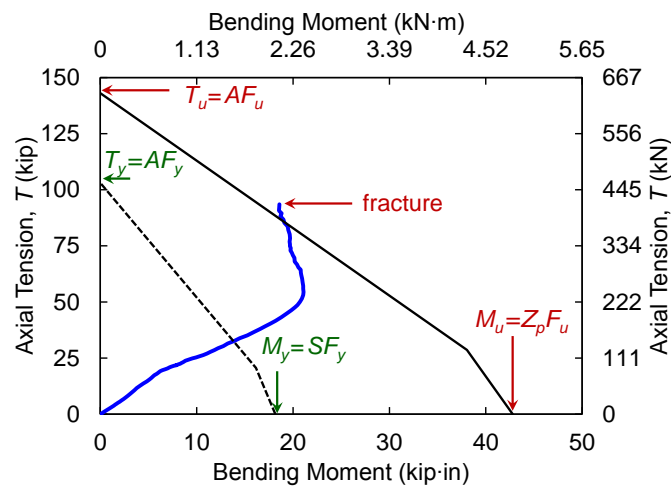


Figure 5–27. Bending moment and axial force interaction for anchorage bars of SMF specimen.

Figure 5–28 shows the deflected shape of the SMF specimen just prior to anchorage bar fracture, which indicates a predominantly linear deflected profile of the beams between the connections, consistent with the experimental measurements (Figure 4–32). Contours of the concrete damage index prior to anchorage bar fracture are shown in Figure 5–29. Extensive concrete damage is evident at the tops of the beams near the end columns and at the bottom of the beams near the center column, consistent with the locations where cracking and spalling were observed in the test (see Figure 4–26).

After fracture of the anchorage bars, the SMF specimen developed additional load carrying capacity through arching action, with the top ends of the beams bearing against the center column, as indicated in Figure 5–30(a), and the bottom ends of the beams bearing against the end columns, as indicated in Figure 5–30(b). Outward forces, from bearing of the beams against the end columns, resulted in inclined damage contours in the lower portions of the end columns, as shown in Figure 5–31(a), indicating the formation of diagonal shear cracks consistent with the experimental observations in Figure 5–31(a).

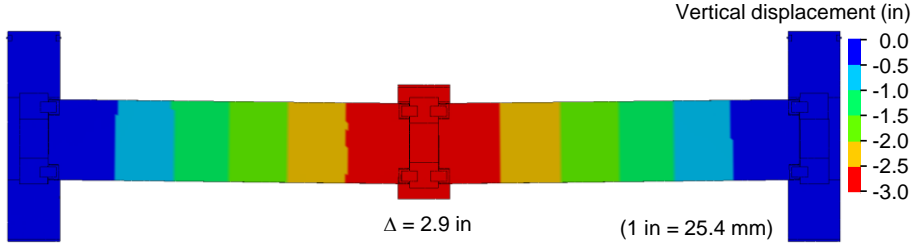


Figure 5-28. Deflected shape of SMF specimen prior to anchorage bar fracture.

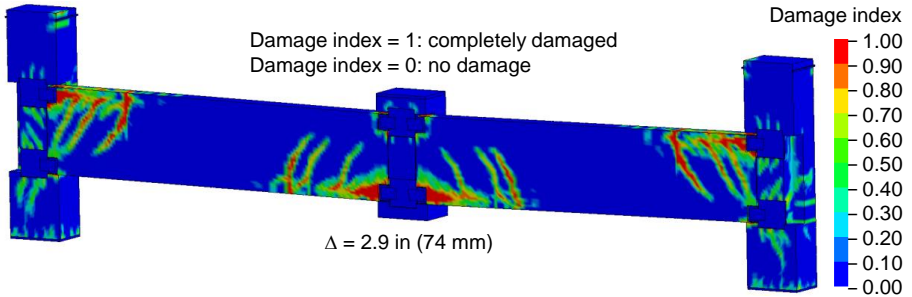


Figure 5-29. Concrete damage for SMF specimen prior to anchorage bar fracture.

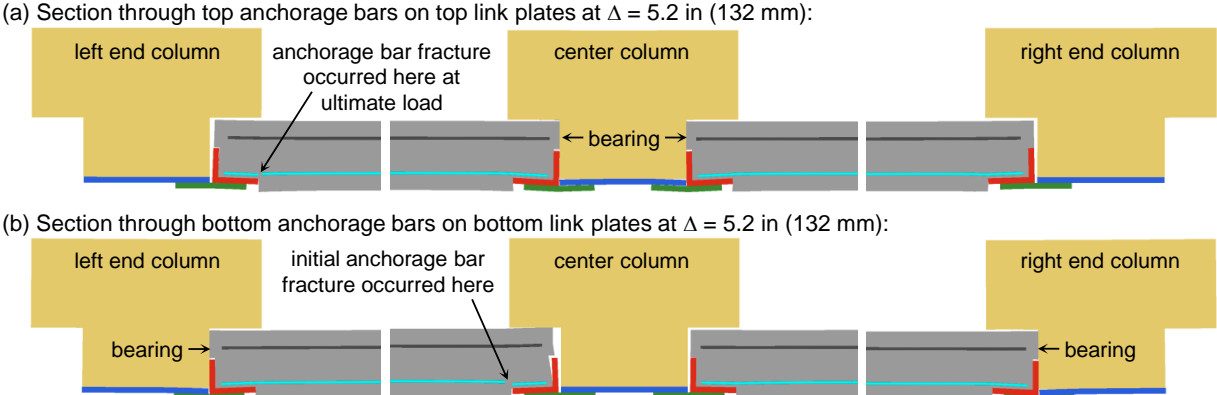


Figure 5-30. Section views of SMF model at the peak vertical load.

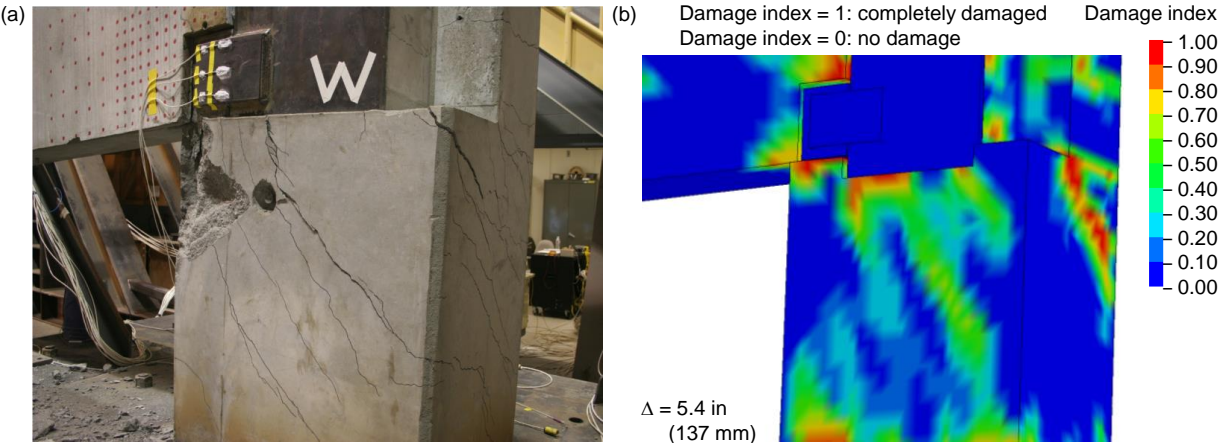


Figure 5-31. Concrete damage on right end column of SMF specimen: (a) photograph; (b) contours of computed damage index.

Figure 5–25(a) shows that the computed vertical load eventually reached an ultimate peak value of 172 kip (765 kN), about 8 % less than the experimental peak, at a center column displacement of $\Delta_u = 5.1$ in (130 mm). The vertical load dropped sharply after reaching the peak value, and a corresponding drop in the horizontal reaction force at the column tops is also evident in Figure 5–25(b). Consistent with the experimental measurements, the horizontal reaction force changed direction from outward to inward after the peak vertical load [see Figure 5–25(b)], as arching action began to force the tops of the end columns outward.

In the computational model, the failure mode associated with the peak vertical load was fracture of the upper anchorage bars at the left end column, as indicated in Figure 5–30(a). In the experiment, the failure mode associated with the peak vertical load was bond failure of the upper anchorage bars at the right end column, which resulted from the formation of splitting cracks and spalling of the concrete cover [see Figure 4–26(f)]. The modeling approach used in this study is unable to capture this failure mode. While bond slip and bond failure could be modeled using a 1-dimensional contact interface between the reinforcing bar and the surrounding concrete (e.g., Lew et al. 2011), such an approach does not capture the influence of discrete crack formation on bond strength, which played an important role in this case. However, while the computational model indicated bar fracture rather than bond failure at the peak vertical load, the model correctly indicated that the failure mode involved the upper anchorage bars at an end column. The computed center column displacement at the peak load was about 22 % less than the experimental value. The earlier failure of the upper anchorage bars in the model suggests that these bars may have been more ductile than was assumed. While all anchorage bars in the model were assumed to have the same ductility, the potential for significant variability in weld-induced reductions in ductility was noted in Section 5.4.

5.6 INFLUENCE OF SPAN LENGTH

As noted in Section 3.1, the span length of the test specimens was reduced to 25 ft (7.6 m) from the prototype span length of 30 ft (9.1 m), in order to fit within the test facility. Somewhat smaller capacities would be expected if the full span length had been used in the test specimens. To investigate the influence of span length, finite element models of each specimen were developed in which the span length was increased to 30 ft (9.1 m), consistent with the prototype building design (see Section 2.1). Apart from the difference in span length, the models were identical to the final post-test models of each specimen (models OMF-A and SMF-A in Table 5–1).

Figure 5–32 shows a comparison of the vertical load-displacement curves computed from the two finite element models of each specimen. Because the self-weight differed for the different span lengths, the vertical load values in Figure 5–32 include the self-weight sustained by the specimens in addition to the load applied to the center column. Only self-weight that was tributary to the center column was added, which included the center column and half of each spandrel beam. For the 25 ft (7.6 m) span length, this self-weight amounted to 29.3 kip (130 kN) for the OMF specimen and 24.9 kip (111 kN) for the SMF specimen, and the vertical load values in Figure 5–32 are thus greater than the corresponding values in Figure 5–18 and Figure 5–25 by these respective amounts. For the 30 ft (9.1 m) span length, the self-weight amounted to 33.8 kip (150 kN) for the OMF specimen and 28.8 kip (128 kN) for the SMF specimen. The displacement values in Figure 5–32 include displacements due to self-weight in addition to the computed displacements due to loading of the center column.

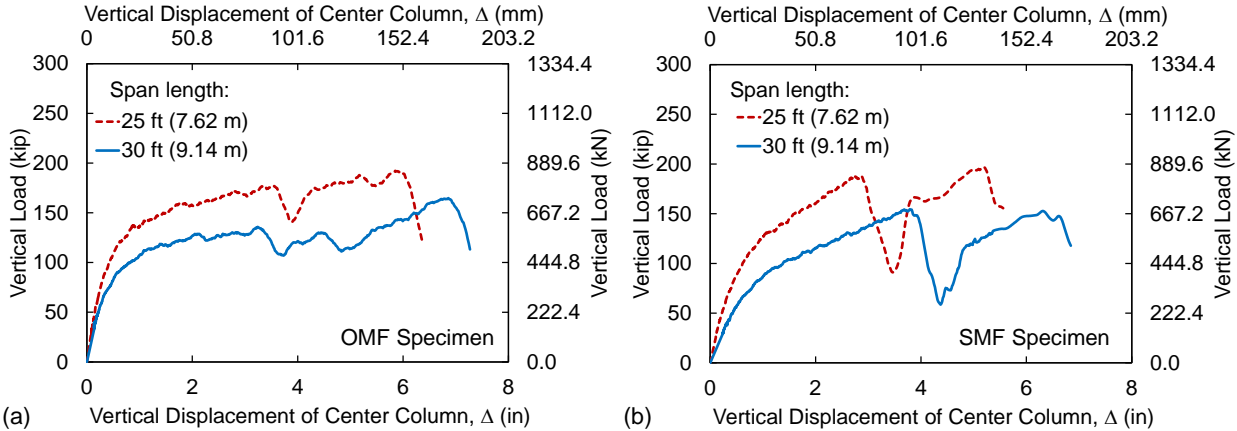


Figure 5–32. Influence of span length on computed vertical load-displacement response: (a) OMF specimen and (b) SMF specimen.

The behaviors and failure modes observed in the computational models with the 30 ft (9.1 m) span length were essentially the same as those described in Section 5.5 for the 25 ft (7.6 m) span length. However, Figure 5–32 shows that the longer-span specimens had lower ultimate capacities that were achieved at larger vertical displacements of the center column. The ratio between the ultimate capacities for the longer and shorter spans was 0.857 for the OMF specimen and 0.786 for the SMF specimen. For the SMF specimen, the influence of arching action was less significant for the longer span length, so that the ultimate peak load at $\Delta_u = 6.3$ in (160 mm) was essentially equivalent to the initial peak load at $\Delta = 3.8$ in (96 mm). The center column displacement at the ultimate load, Δ_u , was larger for the longer span length than for the shorter span length, with a ratio of 1.17 for the OMF specimen and 1.22 for the SMF specimen. However, the beam chord rotation at the ultimate load, θ_u (calculated as described in Section 4.3), was nearly equivalent for both span lengths. The ratio between the values of θ_u obtained for the longer and shorter span lengths was 0.98 for the OMF specimen and 1.01 for the SMF specimen.

5.7 SUMMARY AND DISCUSSION

This chapter presented computational modeling and analysis of the precast OMF and SMF specimens subjected to monotonic loads at the top of the unsupported center column to simulate a column removal scenario. Pre-test models significantly overestimated the capacities of the test specimens, largely because of the sensitivity of the responses to factors that were not well known prior to the tests. Key factors that were found to influence the computed responses included (a) the initial gap width between the spandrel beams and columns, (b) the reduction in ductility of the welded anchorage bars in the heat-affected zone near the welds, and (c) the reduction in effective shear strength of the shear studs due to out-of-plane bending of the link plates. To illustrate the influence of these key factors, computed responses were compared from three models of each specimen, in which individual factors were varied to isolate their effects. By more carefully accounting for each of these factors in the final post-test models, reasonably good agreement with the experimental measurements was achieved. The computed ultimate capacities of the test specimens were 163 kip (725 kN) for the OMF specimen and 172 kip (765 kN) for the SMF specimen, which were less than the experimental values by 2 % and 8 %, respectively. The computational results also provided additional insights into the load-carrying mechanisms and failure modes of the precast concrete moment frames.

For both the OMF and SMF specimens, the failure modes included fracture of anchorage bars at the lower link plate connections to the center column. Detailed finite-element modeling of the welded anchorage bar connections revealed that these failures were influenced by local bending moments near the welds that resulted from eccentricities in the transfer of forces between the link plates and the anchorage bars. For the SMF specimen, component testing of a welded anchorage bar showed that these failures were also influenced by reductions in ductility in the heat-affected zone near the weld. A reduced-order modeling approach for the welded anchorage bar connections that captured these effects was developed, and the failure criterion for bar fracture was calibrated against detailed models. As a consequence of these effects, the computational models of the moment-frame assemblies showed that anchorage bar fracture occurred at 84 % of the ultimate tensile capacity of the anchorage bar for the OMF specimen and at 66 % of the ultimate tensile capacity for the SMF specimen.

Another failure mode observed for the OMF specimen was shear stud failure at the upper link plate connections to the end columns. These failures were influenced by out-of-plane bending of the link plates, which significantly reduced the effective shear capacity of the shear studs relative to their nominal capacity, as confirmed by forces calculated from anchorage bar strain measurements. Developing a failure model for the shear studs that explicitly accounted for the complex interaction of stresses observed in the OMF specimen would have required further research and was not attempted in this study. Rather, the effects of out-of-plane bending were accounted for reducing the effective shear strength of each shear stud to about 30 % of its nominal value. In contrast with other aspects of the modeling, which were based on fundamental constitutive relationships for the various materials, the failure criterion for the shear studs was calibrated to capture the experimentally observed shear stud failures in the OMF specimen.

The computational models were able to capture the arching action that was observed for both specimens, in which increased vertical loads were developed through bearing forces between the beams and columns. Arching action developed when the connection rotations became large enough to close the initial gaps between the spandrel beams and the columns. As a result of arching action, the vertical loads sustained by the moment-frame assemblies were found to be strongly influenced by the initial gap width, particularly for the OMF specimen, which had much deeper spandrel beams. After the development of arching action, significant compressive forces were developed through bearing of the spandrel beams against the end columns, which resulted in damage to the end columns. Inclined damage contours in the lower portions of the end columns became evident in the computational models after the development of arching action, indicating the formation of diagonal shear cracks consistent with the experimental observations. Catenary action did not develop, because failures depleted the capacity of the specimens when the displacement of the center column remained much less than the depth of the spandrel beams.

The test specimens considered in this study had a reduced span length of 25 ft (7.6 m), in order to fit within the testing facility. Using models of the two specimens with the full prototype span length of 30 ft (9.1 m), ultimate capacities of 165 kip (733 kN) and 155 kip (688 kN) were computed for the OMF and SMF specimens, respectively. These capacities include self-weight and represent a reduction relative to the shorter-span capacities by 14 % for the OMF specimen and by 21 % for the SMF specimen. Therefore, although the SMF specimen was designed under more stringent seismic requirements, the computational models predicted that for the full prototype span length, the ultimate capacity of the SMF specimen would actually be somewhat less than that of the OMF specimen. The reduced capacity of the SMF specimen relative to the OMF specimen resulted from earlier fracture of the anchorage bars and from less extensive arching action because of the reduced beam depth.

Chapter 6

EVALUATION OF STRUCTURAL ROBUSTNESS

This chapter presents an evaluation of the structural robustness of the precast moment-frame assemblies through a comparison of their ultimate capacities with the applicable gravity loads from the prototype buildings. An energy-based procedure was used to account for the dynamic effects of sudden column loss. Because the test specimens used a reduced span length, computational results from Section 5.6 for specimens with the full prototype span length of 30 ft (9.1 m) were used in the evaluation of structural robustness. This accounted for the reduction in capacities associated with the longer span length and enabled a direct comparison with the gravity loads from the prototype buildings.

6.1 GRAVITY LOADS

The following load combination is considered in evaluating applicable gravity loads:

$$1.2D + 0.5L \quad (6.1)$$

where D is dead load and L is live load. Eq. (6.1) corresponds to the load combination specified in ASCE 7-10 (ASCE 2010, Section 2.5.2.2) for evaluating the residual capacity of structural systems following the notional removal of load-bearing elements. Although the span length of the test specimens was reduced to 25 ft (7.6 m) to fit within the test facility, the full span length of 30 ft (9.1 m) is considered in evaluating applicable gravity loads on the moment frame assemblies.

A live load of 50 psf (2.40 kN/m²) is considered, corresponding to office occupancy, with a live load reduction factor of 0.75 based on Eq. (4.7-1) in ASCE 7-10, resulting in a reduced live load 37.5 psf (1.80 kN/m²). Multiplying by the tributary area of (30 ft)(15 ft) = 450 ft² [(9.1 m)(4.6 m) = 42 m²] for an edge column (see Figure 2–1) yields an unfactored live load of 16.9 kip (75.1 kN) acting on the column to be removed.

The dead load acting on the column to be removed includes self-weight plus a superimposed dead load of 10 psf (0.48 kN/m²). The unfactored dead load corresponding to the tributary area of the column to be removed was estimated from the design documents (Kim, Dasgupta, and Ghosh 2009a,b) as 83 kip (369 kN) for the OMF building and 81 kip (360 kN) for the SMF building. Evaluating the load combination in Eq. (6.1) with the dead and live loads defined above yields total gravity loads of 108 kip (481 kN) and 106 kip (470 kN) acting on the column to be removed for the OMF assembly and the SMF assembly, respectively.

6.2 ENERGY-BASED ANALYSIS

Given a load-displacement relationship obtained from static loading of a structure with an unsupported column, energy-based analysis can be used to account for the dynamic effects associated with sudden column loss, thereby calculating the peak dynamic displacement after sudden column loss under any given level of loading (Powell 2003, Izzuddin et al. 2008, Main 2014). The analysis is based on the fact that the kinetic energy is zero at the peak displacement, assuming a single predominant mode of deformation, so that conservation of energy requires the internal energy in the structure to equal the external work done by gravity loads.

Let $P_s(\Delta)$ denote a load-displacement relationship obtained from nonlinear static pushdown analysis of a structure with an unsupported column, where Δ is the vertical displacement of the unsupported column. The solid curve in Figure 6–1 illustrates such a static load-displacement relationship. Let $P_d(\Delta)$ denote the corresponding relationship between the load and the peak dynamic displacement under sudden column loss, illustrated by the dashed curve in Figure 6–1. At a peak dynamic displacement of Δ , the balance between the work done by the external load, corresponding to the hatched area in Figure 6–1, and the internal energy in the structure, corresponding to the shaded area in Figure 6–1, can be expressed as follows:

$$P_d(\Delta) \cdot \Delta = \int_0^{\Delta} P_s(\tilde{\Delta}) d\tilde{\Delta} \quad (6.2)$$

where $\tilde{\Delta}$ is a dummy variable in the integral representing the vertical column displacement. Rearranging Eq. (6.2) yields the following relationship:

$$P_d(\Delta) = \frac{1}{\Delta} \int_0^{\Delta} P_s(\tilde{\Delta}) d\tilde{\Delta} \quad (6.3)$$

Eq. (6.3) allows the dynamic effects associated with sudden column loss to be evaluated directly from the results of a nonlinear static pushdown analysis.

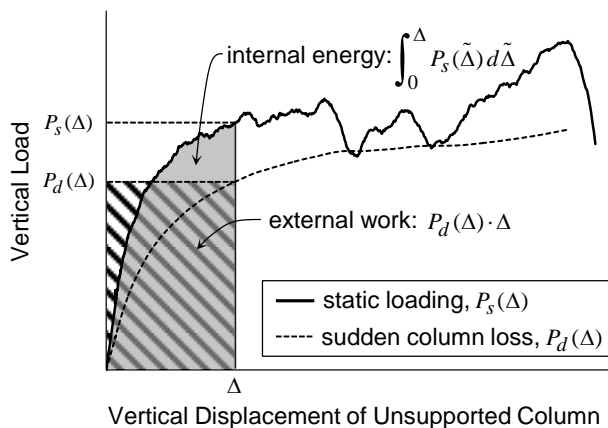


Figure 6–1. Energy-based analysis of sudden column loss.

6.3 RESULTS

Figure 6–2 shows load-displacement curves for the two moment-frame assemblies for both static loading and sudden column loss. The static load-displacement curves in Figure 6–2 were obtained from the computational models and are equivalent to the curves presented previously in Figure 5–32 for the 30 ft (9.14 m) span length. The curves for sudden column loss were evaluated from Eq. (6.3) by numerical integration of the static load-displacement curves.

Plotted with the load-displacement curves in Figure 6–2 are dashed horizontal lines corresponding to the applicable gravity loads from Eq. (6.1). The intersection of the curve for $P_d(\Delta)$ with this horizontal line in each plot gives the peak dynamic displacement under sudden column loss, and peak dynamic displacements of 3.3 in (83 mm) and 3.9 in (100 mm) were obtained for the OMF specimen and the SMF specimen, respectively. The analyses thus predicted that both precast specimens could sustain the applicable gravity loads under sudden column loss without collapse. For both specimens, however, the curves for $P_d(\Delta)$ exceeded the applicable gravity loading only slightly, and the predicted displacements under sudden column loss were highly sensitive to further increases in the gravity loading.

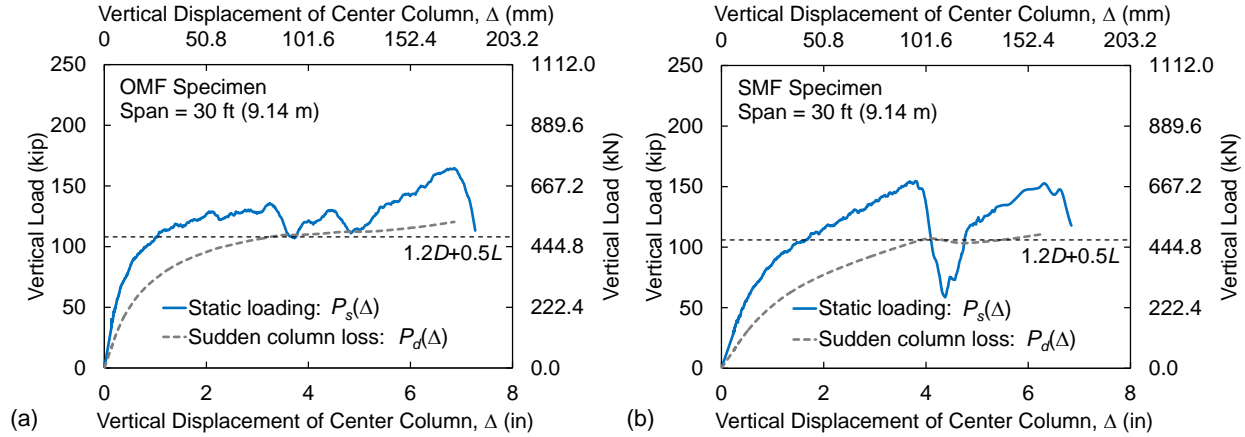


Figure 6–2. Load-displacement relationships for static loading and sudden column loss compared with applicable gravity loading: (a) OMF specimen; (b) SMF specimen.

The ultimate capacities under static loading in Figure 6–2 were 165 kip (733 kN) and 155 kip (688 kN) for the OMF and SMF specimens, respectively, occurring at displacements of $\Delta_u = 6.9$ in (174 mm) and $\Delta_u = 6.3$ in (160 mm). A normalized measure of the ultimate capacity under static loading, denoted $\lambda_{s,u}$, can be obtained by dividing the ultimate static capacity by the gravity loading from Eq. (6.1). Values of $\lambda_{s,u} = 1.53$ and $\lambda_{s,u} = 1.46$ were obtained for the OMF and SMF specimens, respectively, indicating that the specimens could sustain static loads exceeding the applicable gravity loading by about 50 %.

Ultimate capacities under sudden column loss were calculated at the displacement corresponding to the ultimate static load, as proposed by Main (2014), and ultimate capacities of $P_d(\Delta_u) = 120$ kip (535 kN) and $P_d(\Delta_u) = 108$ kip (479 kN) were obtained for the OMF and SMF specimens, respectively. Dividing these values by the applicable gravity loading yields normalized values of the ultimate capacity under sudden column loss, denoted $\lambda_{d,u}$. The quantity $\lambda_{d,u}$ was proposed by Bao et al. (2014) as a *robustness index* for structural systems, where values greater than unity indicate that a structure will not collapse under sudden column loss. Using this approach, robustness indices of $\lambda_{d,u} = 1.11$ and $\lambda_{d,u} = 1.02$ were obtained for the OMF and SMF specimens, respectively. This indicates that the precast specimens could sustain loads 2 % - 11 % greater than the applicable gravity loads under sudden column loss.

Table 6–1 summarizes the normalized ultimate capacities obtained from the computational results in Figure 6–2 for the full prototype span length. Also presented in Table 6–1 are values of the dynamic increase factor (DIF) at the ultimate static load, defined as follows:

$$\Omega(\Delta_u) = \lambda_{s,u} / \lambda_{d,u} \quad (6.3)$$

The results indicate that in a nonlinear static analysis, the loads on the precast concrete frames would need to be increased by about 40 % to account for the dynamic effects associated with sudden column loss.

Table 6–1. Normalized ultimate capacities and dynamic increase factors for OMF and SMF specimens with prototype span lengths.

Specimen	Span Length ft (m)	Normalized Ultimate Capacity		Dynamic Increase Factor, $\Omega(\Delta_u)$
		Static Loading, $\lambda_{s,u}$	Sudden Column Loss ¹ , $\lambda_{d,u}$	
OMF	30 (9.14)	1.53	1.11	1.37
SMF	30 (9.14)	1.46	1.02	1.43

¹ *Robustness index*, obtained using the approximate energy-based analysis of Eq. (6.3)

6.4 DISCUSSION AND LIMITATIONS

The computed results in Table 6–1 indicate that the capacities of the precast moment frames would be adequate to withstand sudden column loss, with reserve capacities of 2 % - 11 % against collapse. These reserve capacities, however, are comparable to the uncertainty in the model predictions. Differences of 2 % - 8 % were observed between the computed and experimental ultimate capacities for the reduced span length of 25 ft (7.6 m), and somewhat larger discrepancies would be expected when extending the models to the full prototype span length of 30 ft (9.1 m). In addition, the computed responses were found to be highly sensitive to factors such as the initial gap width between the beams and columns (which was not specified in the design) and the ductility of the welded anchorage bars. Variations in these factors were found to reduce the computed ultimate capacities by 35 % (see Section 5.1). Differences in these factors were observed between the two specimens that were tested, with larger gap widths for the OMF specimen and greater reductions in anchorage bar ductility for the SMF specimen. Additional variability in the test specimens was introduced by installation errors for the SMF specimen (see Section 3.1), although computational modeling showed that these errors reduced the ultimate capacity by only about 4 %. Because of the strong sensitivities observed, significant variability might be expected if multiple tests of nominally identical specimens were tested, and some combinations of factors could result in specimens that would not sustain the applicable gravity loads under sudden column loss.

The computed results for the full prototype span length (Table 6–1) indicate that the normalized ultimate capacities of the OMF and SMF specimens were approximately equivalent. For the reduced span length of 25 ft (7.6 m), both the experimental and computational results showed slightly higher capacities for the SMF specimen. With increased span length, however, the computational results showed greater reductions in capacity for the SMF specimen than for the OMF specimen. As a result, for the full prototype span length of 30 ft (9.1 m), the normalized ultimate capacity of the SMF specimen was actually slightly less than that of the OMF specimen under both static loading and sudden column loss.

The comparable performance of the OMF and SMF specimens contrasts with previous full-scale testing of steel moment frames (Sadek et al. 2010) and cast-in-place concrete moment frames (Lew et al. 2011), in which the ultimate capacity of SMF specimens under a column removal scenario was approximately twice the ultimate capacity of corresponding intermediate moment frame (IMF) specimens. Because the design and detailing requirements for an OMF are less stringent than for a seismically designed IMF, even more significant improvements in performance might be expected for an SMF specimen relative to an OMF specimen.

For a column removal scenario in an actual building, the response of a precast concrete moment frame would depend on the resistance provided by the surrounding structural system, which would vary depending on the location within the building. This study considered end columns with spandrel beams framing into the connections from only one side. Spandrel beams framing into the columns from both sides would provide additional resistance to rotation and horizontal displacement of the columns, thus reducing the flexural and shear demands on the columns and providing increased support for the development of compressive arching action. Axial forces in the columns due to gravity loads from the upper stories, while increasing the stress levels in the columns, would also provide increased resistance to shear forces resulting from arching action. In a corner column removal scenario, however, negligible arching action would be expected, because of the limited horizontal restraint of the corner column. These issues, and other influences of the surrounding structural system on the robustness of precast concrete moment frames, can be investigated in future studies using computational modeling.

Chapter 7

SUMMARY AND CONCLUSIONS

This report presented an experimental and computational study of two precast concrete moment-frame assemblies, each comprising three columns and two beams. The two moment-frame assemblies represented portions of the structural framing system of two ten-story precast concrete frame buildings. One building was designed for Seismic Design Category B (SDC B) and the other for SDC D. The moment-frame assemblies were taken from the exterior moment-resisting frames of these buildings. The test specimen extracted from the SDC B building was part of an ordinary moment frame (OMF) and the test specimen extracted from the SDC D building was part of a special moment frame (SMF). The specimens were subjected to monotonically increasing vertical displacement of the unsupported center column to observe their behavior under a simulated column removal scenario, including the development of arching action in the beams. The vertical displacement of the center column was increased beyond the ultimate capacity of the assemblies to characterize the failure modes and collapse mechanisms that developed.

The behavior of the moment-frame assemblies was analyzed using detailed finite element models, in which solid elements were used to represent the concrete, steel plates, and steel angles, while beam elements were used to represent the longitudinal and transverse reinforcement in the beams and columns. The analyses conducted using these models were able to capture the primary response characteristics of the test specimens, and the analyses provided insight into the overall behavior and failure modes.

Based on the study reported herein, the following conclusions were reached.

1. For both the OMF and the SMF specimens, the behavior was dominated by flexure in the early stages of the response. With increased vertical displacement of the center column, the initial gaps between the beams and columns closed, and additional resistance was provided through arching action, with the top corners of the beams bearing against the center column and the bottom corners of the beams bearing against the end columns. Computational modeling showed that the vertical resistance developed through arching action was sensitive to the initial gap width between the beams and columns, with smaller gaps resulting in larger forces from arching action.
2. Catenary action did not develop in either the OMF or the SMF specimen, in contrast with previous testing of reinforced concrete moment frames, for which tensile forces developed in the beams when the deflection of the center column was approximately equal to the beam depth. The precast concrete spandrel beams tested in this study had greater depths than the reinforced concrete beams tested previously, and failures of the beam-to-column connections depleted the capacities of the specimens when the deflections of the center column remained much less than the beam depths.
3. Both the OMF and SMF specimens exhibited the following failure modes: (a) cracking and spalling of concrete near the welded link plate connections between the precast concrete beams and columns, (b) fracture of the bottom anchorage bars at the welded connection to the center column, and (c) diagonal cracking, spalling, and outward shear deformation of the end columns below beam level as a result of arching action in the beams.

4. Fracture of the welded anchorage bars occurred at relatively small beam chord rotations of 0.019 rad for the OMF specimen and 0.0087 rad for the SMF specimen. The anchorage bars fractured earlier than would be expected under tensile loading as a result of the following two factors: (a) local bending moments in the anchorage bars resulting from eccentricities in the connections, which interacted with the tensile forces to produce larger tensile stresses, and (b) reductions in the ductility of the anchorage bars as a result of welding the bars to the connecting angles.
5. The diagonal cracking, spalling, and shear deformation of the end columns observed in these tests indicate that lateral forces due to arching action could potentially result in shear failure of columns. If arching action is to be exploited in resisting vertical loads under column removal scenarios, care must then be taken to ensure that the columns adjacent to the missing column can resist the lateral loads induced by arching action.
6. Additional failure modes that were observed included (a) detachment of embedded steel column plates with welded shear studs from the end columns of the OMF specimen under a combination of unbalanced shear forces and out-of-plane bending induced by the link plates and (b) bond failure of the upper anchorage bars at the right end column at the ultimate load of the SMF specimen, resulting from the formation of splitting cracks and spalling of concrete.
7. The ultimate capacity of the OMF specimen was 166 kip (738 kN), while the ultimate capacity of the SMF specimen was 188 kip (836 kN). Corresponding beam chord rotations at the ultimate load were 0.019 rad for the OMF specimen and 0.022 rad for the SMF specimen. Thus, the more stringent seismic design requirements for the SMF specimen resulted in an increase of only 13 % in the ultimate capacity under the column removal scenario, with an increase of 18 % in the corresponding beam chord rotation.
8. The test specimens had a reduced span length of 25 ft (7.6 m), and computational modeling showed that considering the full prototype span length of 30 ft (9.1 m) reduced the ultimate capacity by 14 % for the OMF specimen and by 21 % for the SMF specimen. The ultimate capacities of the prototype-span specimens under static loading exceeded the applicable gravity loading of $1.2D+0.5L$ by factors of 1.53 and 1.46 for the OMF and SMF specimens, respectively. Ultimate capacities of the prototype-span specimens under sudden column loss were evaluated using an approximate energy-based procedure, and the resulting values slightly exceeded the applicable gravity loading, by factors of 1.11 and 1.02 for the OMF and SMF specimens, respectively. However, given the observed sensitivity of the results to factors such as the initial gap width between the beams and columns and the weld-induced reductions in ductility of the anchorage bars, variations in these factors could result in specimens that would not sustain the applicable gravity loads under sudden column loss. The computational results indicated that for the full prototype span length, the ultimate capacity of the SMF specimen was approximately equivalent to that of the OMF specimen, in spite of the more stringent design requirements.

Future research on precast concrete structures will involve development and evaluation of modified connection details to enhance performance (e.g., by eliminating eccentricities and weld-induced embrittlement in the anchorage bar connections). Connections with less sensitivity to factors such as gap width and anchorage bar ductility are desirable, so that more consistent and predictable performance could be achieved. The influence of the surrounding structural system on the response of precast concrete moment frames will also be investigated using computational modeling, including the effects of three-dimensional framing under various column removal scenarios.

REFERENCES

- American Concrete Institute (ACI). (2005), *Building Code Requirements for Structural Concrete (ACI 318-05) and Commentary (ACI 318R-05)*, Farmington Hills, MI, 2005.
- American Institute of Steel Construction (AISC). (2010). “Specification for structural steel buildings.” *ANSI/AISC 360-10*, Chicago, IL.
- American Society of Civil Engineers (ASCE). (2002). *Minimum Design Loads for Buildings and Other Structures, SEI/ASCE 7-02*, Reston, VA.
- American Society of Civil Engineers (ASCE). (2010). *Minimum Design Loads for Buildings and Other Structures, SEI/ASCE 7-10*, Reston, VA.
- American Welding Society (AWS). (2010). “Structural welding code – steel.” *AWS D1.1/D1.1M:2010*, Miami, FL.
- Bao, Y., Main, J.A., Lew, H.S., and Sadek, F. (2014). “Robustness assessment of RC frame buildings under column loss scenarios.” *Proc., 2014 Structures Congress*, ASCE, Reston, VA.
- Delatte, N.J. (2009). *Beyond Failure: Forensic Case Studies for Civil Engineers*, ASCE Press, Reston, VA.
- Dieter, G.E. (1976). *Mechanical Metallurgy*, 2nd ed., McGraw-Hill, New York.
- Elliott, K.S. and Jolly, C.K. (2013). *Multi-Story Precast Concrete Framed Structures*, Blackwell, West Sussex, UK.
- Engström, B. (1990). “Connections between precast components.” *Nordisk Betong, Journal of the Nordic Concrete Federation*, 2(3), 53-56.
- Federal Highway Administration (FHWA). (2007). “Evaluation of LS-DYNA Concrete Material Model 159.” *Publication No. FHWA-HRT-05-063*, McLean, VA.
- Griffiths, H., Pugsley, A.G., and Saunders, O. (1968). *Report of the Inquiry into the Collapse of Flats at Ronan Point, Canning Town*, Her Majesty’s Stationery Office, London.
- Hallquist, J. (2007), *LS-DYNA Keyword User’s Manual*, Livermore Software Technology Corporation, Livermore, CA, Version 971.
- International Code Council (ICC). (2003), *International Building Code*, Falls Church, VA.
- Kang, S.B., and Tan, K.H. (2015). “Behaviour of precast concrete beam–column sub-assemblages subject to column removal.” *Engineering Structures*, 93, 85-96.
- Kim, J., Dasgupta, P., and Ghosh, S.K. (2009a). “Assessment of the ability of seismic structural systems to withstand progressive collapse: design of precast concrete frame building (seismic design category B).” *Report submitted to the National Institute of Standards and Technology*, Gaithersburg, MD.
- Kim, J., Dasgupta, P., and Ghosh, S.K. (2009b). “Assessment of the ability of seismic structural systems to withstand progressive collapse: design of precast concrete frame building (seismic design category D).” *Report submitted to the National Institute of Standards and Technology*, Gaithersburg, MD.
- Lew, H.S., Bao, Y., Sadek, F., Main, J.A., Pujol, S., and Sozen, M.A. (2011). “An experimental and computational study of reinforced concrete assemblies under a column removal scenario.” *NIST Technical Note 1720*, National Institute of Standards and Technology, Gaithersburg, MD.
- Main, J.A. (2014). “Composite floor systems under column loss: collapse resistance and tie force requirements.” *Journal of Structural Engineering*, 10.1061/(ASCE)ST.1943-541X.0000952, A4014003.
- Nimse, R.B., Joshi, D.D., and Patel, P.V. (2014). “Behavior of wet precast beam column connections under progressive collapse scenario: an experimental study.” *Int. J. Adv. Struct. Eng.*, 6, 149-159.
- Nimse, R.B., Joshi, D.D., and Patel, P.V. (2015). “Experimental study on precast beam column connections constructed using RC corbel and steel billet under progressive collapse scenario.” *Proc., 2015 Structures Congress*, ASCE, Reston, VA.

- Ollgaard, J.G., Slutter, R.G., and Fisher, J.W. (1971). "Shear strength of stud connectors in lightweight and normal weight concrete." *Engineering Journal*, AISC, 8(2), 55-64.
- Precast/Prestressed Concrete Institute (PCI). (2004). *PCI Design Handbook, 6th Edition*, Chicago, IL.
- Precast/Prestressed Concrete Institute (PCI). (2014). *PCI Design Handbook, 7th Edition*, Chicago, IL.
- Regan, P.E. (1974). "Catenary tests on composite precast-in situ concrete composite floors." *Report to the Department of Environment*, The Polytechnic of London.
- Sadek, F., Main, J.A., Lew, H.S., Robert, S.D., Chiarito, V.P., and El-Tawil, S. (2010). "An experimental and computational study of steel moment connections under a column removal scenario." *NIST Technical Note 1669*, National Institute of Standards and Technology, Gaithersburg, MD.
- Shultz, D., Burnett, E., and Fintel, M. (1978). "A design approach to general structural integrity – Design and construction of large panel concrete structures." *Supplemental Report A*, Portland Cement Association, Skokie, USA.